Deployable radiator wing for high performance CubeSats

Designing, analysing, prototyping and testing

C.A.B. van Lierop

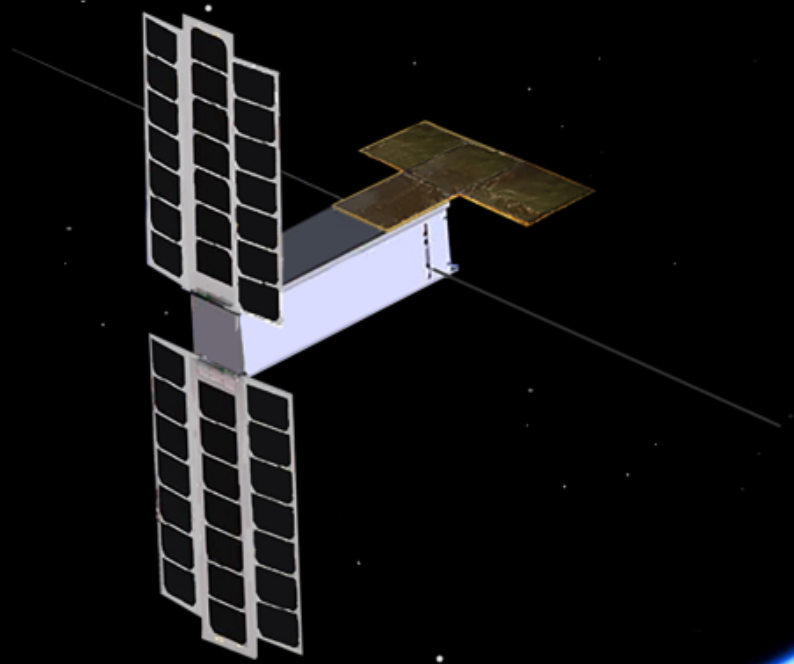

Technische Universiteit Delft

TU Delft

Deployable radiator wing for high performance CubeSats

Designing, analysing, prototyping and testing

by

Casper Adriaan Bastiaan van Lierop

to obtain the degree of Master of Science
in Spaceflight - Aerospace Engineering
at the Delft University of Technology,
to be defended publicly on February 4, 2021 at 9:30.

Student number: 4367707
Project duration: October 6, 2019 – February 4, 2021
Thesis committee:

Dr. A. Cervone	TU Delft, chair
Dr. J. Guo	TU Delft, supervisor
M. Grimminck MEngSc	Airbus Defence and Space Netherlands, supervisor
Dr. M.J. Heiligers	TU Delft, independent examiner

An electronic version of this thesis is available at http://repository.tudelft.nl/.

Cover image: Artist impression of the CubeSat with the deployable radiator wing, composed of existing images from [4, 16] by F.A.V. van Lierop.

TU Delft Delft University of Technology

AIRBUS

Preface

This thesis report concludes my journey of my Bachelor Aerospace Engineering and my Master Space Flight at the Delft University of Technology.

This thesis could not have been performed without the help and resources provided by Airbus Defence and Space Netherlands. I would like to thank my supervisor at Airbus Defence and Space Netherlands, Mark Grimminck for his help and time. He gave me the opportunity to work on this thesis and to build a prototype. Furthermore, I would like to thank the employees of Airbus Defence and Space Netherlands for their help. Most notably N. van der Pas and S. Loarte Castro with their extensive help and to answer my many questions about the software and thermal control. K. Koek had all the expertise and experience to help me produce the prototype.

I also would like to thank my supervisor Dr. J. Guo, Associate Professor of Space Systems Engineering in the Faculty of Aerospace Engineering of the Delft University of Technology (TU Delft). He oversaw my work and graded my work. He provided me with extensive and useful feedback and advice.

Unfortunately, halfway during my thesis, the pandemic of COVID19 struck the Netherlands. I had to work from home. The most unfortunate consequence was that I could not perform the tests at the test facilities at Airbus necessary for this thesis. Suddenly, I had to find new test possibilities and found these at the university. Thanks a lot to Dr. J. Guo for his help finding these alternative test facilities at the university. Also a lot of thanks to my fellow society members from Delft Aerospace Rocket Engineering (DARE) for being allowed to use DARE measurement equipment, useful for the alternative test. Thanks to M.S. Uludag for his help with the vacuum oven on short notice for the alternative test. Last but not least, I thank my family and friends for their support and help. Special thanks to my sister F.A.V. van Lierop for the artist impression of a CubeSat with my design for the deployable radiator wing, on the cover page of this thesis.

I had planned for more tests including a vibration test, a thermal contact resistance test of the materials used and a deployment test. Unfortunately, this was not possible due to the pandemic.

C.A.B. van Lierop
Delft, October 2020

Summary

Spaceflight is becoming more accessible for companies, research institutes and students due to the development of CubeSats. These small satellites contain small and typically few payloads. The trend is that these payloads reduce in size, but not in power, which increases in power density and total power. These high-performance CubeSats generate a lot of heat relative to their size. This heat must be rejected to prevent overheating. The standard thermal control solutions for CubeSats, such as body mounted surfaces, are not sufficient. This thesis proposes a dedicated deployable radiator to solve this thermal control problem. Furthermore, it investigates the deployable radiator's thermal performance by two lumped parameter numerical models with thermal modelling software. One model for the deployable radiator individually and one model of a system with a CubeSat dummy with the deployable radiator integrated. These models are verified by simplified models and a test with a prototype. The thesis's goal is to answer the following research question: *What is the effect of an external radiator using High Performance Radiator (HiPeR) to the temperature progression of a CubeSat over the course of a polar orbit?*

The deployable radiator should be light, foldable and have high thermal efficiency. A laminate of adhered sheets of the highly conductive material Pyrolytic Graphite (PG) with protective Kapton sheets on the external surfaces is used to achieve this. This laminate is developed by Airbus Defence and Space Netherlands and is called HiPeR. This laminate is semi-flexible but not enough to fold it sufficiently and with specific design elements can be folded such that it can be stored with minimum volume. Given that the CubeSat's available internal volume is limited, it is proposed that the radiator is folded around the external surfaces of the CubeSat. The radiator has the shape of the letter T (inverted). This allows for folding around the cubical shape of a CubeSat. Typically, the laminate is not flexible enough to achieve the required bending radius to fold around the sharp edges of the CubeSat. The adhesive is not applied to the folding parts of the radiator to increase the local flexibility, allowing a tighter bending radius. These parts are called the hinges. The flexible hinges require additional stiffness once deployed to maintain the radiator shape in orbit. Additionally, actuation is also required to deploy the radiator. Typical hinges used for deploying solar arrays are too big, whereas a tape spring offers a novel way of using a stiff beam to function as a hinge when elastically deforming the shape. This creates a tape spring hinge. These hinges are located in the hinge parts. When folding the tape spring hinge, stresses are induced in the material, and potential energy is stored like a spring. This potential energy can be used to deploy the radiator passively. The heat generated internally is connected to the radiator thermal interface via a thermal link. This thermal link can be a heat pipe or a conductive strip of material. However, this is out of the scope of this thesis. The T-shaped radiator made from 12 sheets of PG is able to fold around the cubical size of a CubeSat and able to deploy with a tape spring hinge.

The thermal performance of the deployable radiator is analysed with a numerical model in ESATAN-TMS-2019 to achieve optimisation of the design. This includes the number of layers of PG sheets, the size of the hinge parts and the shape of the radiator. Each layer of the radiator laminate is modelled individually. A heat flow boundary condition is applied on the edge of the base part, and the environment boundary condition is deep space. Modelling the radiator individually, achieved that the steady-state temperatures and heat flows are demonstrated to be fit for purpose with this design concept.

Analysing the thermal performance of the radiator individually provides not enough information on whether the radiator reduces the temperature of the high-performance CubeSat in orbit around Earth. To analyse this, the radiator is integrated into a dummy CubeSat to analyse the combined influence on the performance. The dummy CubeSat has dummy payloads to simulate the heat generated during an orbit. Deployable, rotating and Sun pointing solar arrays have been modelled at the top of the CubeSat to represent the view factors and shading. The size of the solar arrays is representative for the power requirements. The radiator is located on the bottom side of the CubeSat perpendicular to the axis of rotation of the solar arrays to minimise Sun illumination on the radiator. The radiator is connected to the heat-generating payloads via a thermal link. The deployable radiator is integrated on a representable CubeSat to analyse the in-orbit thermal performance.

The design of the dummy CubeSat with the radiator is analysed also using ESATAN-TMS-2019. The research question is answered by comparing the temperature progression of the dummy payloads inside the CubeSat over an orbit in two cases: one with the deployable radiator and one without a dedicated radiator. It is found that the radiator causes the payload temperatures in a specific heat load case to drop from 85°C to 20°C. This reduction is caused by the improved thermal coupling of the payloads to space via the radiator. On average, the heat dissipated by the payload to space is 12 W with a heat load of 30 W. The remaining 22 W is radiated to space via the CubeSat body. This demonstrates that the deployable radiator is capable of reducing the temperatures of the CubeSat.

The sensitivity analysis showed that some design assumptions on the parameters have a significant impact on the thermal performance of the radiator. These parameters include the thermal conductivity of the thermal link between the dummy payloads and the radiator and changes in the orbit of the CubeSat around Earth due to the Earth revolving around the Sun. The sensitivity analysis showed that the radiator is insensitive for the number of layers. Increasing to 24 layers reduces the temperatures only with a few degrees, while it almost doubles the mass of the DRW laminate.

A test with a prototype of the radiator has been performed. The test was performed in a vacuum oven. Due to the COVID-19 pandemic, testing in a vacuum chamber with low pressure was not possible. The alternative test facility, the vacuum oven did not achieve enough vacuum such that radiative heat transfer is dominant over the heat transfer via the air. It is estimated that around 52% of the total heat is dissipated via radiative heat transfer. It is desired that the radiative heat flow is dominant because this is more representable for the circumstances in space where there is almost no air at all. Furthermore, for the numerical simulation of the test, the model to predict the influence of the air overestimated the heat flows via the air. Thus the verification by testing has high uncertainty. Therefore, the results are inconclusive. Further testing in a more representative test environment is required to verify the numerical results in ESATAN-TMS-2019. The test showed that the deployable radiator is able to dissipate heat efficiently. However, it was not possible to verify the numerical model.

In conclusion, the deployable radiator is verified by analyses that it reduces the temperature of the payloads significantly within the requirements for the assumed load case. This reduction is demonstrated by the efficient heat flow path between the payloads and space via the radiator. The deployable radiator makes it possible to design CubeSats that use increasingly higher power dissipating payloads. The design concept demonstrated as part of this thesis has shown compatibility of a CubeSat payload of up to 30 W of power without the risk of overheating.

Contents

List of Figures

List of Tables

List of Symbols

Greek

ϵ	Emissivity	-
Ω	Longitude of the ascending node	°
Φ	Angle between two plates	°
σ	Stefan Boltzmann constant	W m^{-2} K^{-4}

Roman

a	Width of plate 2	m
a	Width	m
A	Area	m^2
b	Length	m
b	Width of plate 1	m
B_{ij}	Gebhart factor from surface i to j	-
c	Distance between two plates	m
c	Length of both plates	m
F_{ij}	View factor from surface i to j	-
k	Thermal conductivity	W m^{-1} K^{-1}
L	Fraction of the width and the length of a plate	-
L	Length	m
N	Fraction of the width and the length of a plate	-
T	Temperature	K
X	Fraction of the width and distance for two opposing square plates	-
Y	Fraction of the length and distance of two opposing square plates	-

List of Abbreviations

ASD Acceleration Spectral Density.

COTS Commercial of the Shelf.

DOT Design Option Tree.
DRW Deployable Radiator Wing.

ESATAN-TMS-2019 ESATAN Thermal Modelling Suite 2019.

GUI Graphical User Interface.

HDRS Hold Down and Release System.

HiPeR High Performance Radiator.

IR Infrared.
ISS International Space Station.

LEO Low Earth Orbit.

P-POD Poly-Picosatellite Orbital Deployer.
PCB Printed Circuit Board.
PG Pyrolytic Graphite.

TRL Technology Readiness Level.
TU Delft Delft University of Technology.

1 Introduction

In recent years space has become increasingly accessible for companies, researchers and students due to CubeSats. These small satellites contain only small payloads. Developers made instruments and subsystems much smaller and lighter in the past few years. Thus it is possible to put more payloads and instruments on the same platform. More payload and instruments increase the economic and scientific value for CubeSats. Where the miniaturisation of equipment continues, the power density increases and therefore the total power too. This increase in power density will cause the systems to be operating at higher temperatures. Instruments and electronics have a maximum operating temperature limit and exceeding this limit, harms the systems. Therefore, a solution is needed to prevent the systems from overheating. To solve the issue of overheating, the heat flow to space should become more efficient. This means that for the same heat flow, the temperature gradient is smaller. This thesis project focuses on designing, analysing, prototyping, and testing a system for radiating excess heat, called Deployable Radiator Wing (DRW).

First, a general introduction is given in Section 1.1 to provide a need for a system for radiating excess heat for CubeSats. From this need follows a problem with a proposed solution, which will be discussed in Section 1.2. How this solution is tested to the research question, is explained in Section 1.3. Finally, the thesis outline is explained in Section 1.4.

1.1. General introduction

This section will explain the need for a system for radiating excess heat for CubeSats. First, an introduction is given about the rise of CubeSat in Subsection 1.1.1. Next to the trend of miniaturisation of spacecraft systems for CubeSat, a byproduct emerges: high-performance CubeSat. Subsection 1.1.2 explains the byproduct[1].

1.1.1. Rise of CubeSat and miniaturisation

The growing trend in spacecraft design is in miniaturisation [30, 32] and the use of nanosatellites such as CubeSats [7]. Miniaturisation means creating smaller and smaller components and (sub)systems in terms of size and mass. This must be achieved while maintaining or increasing performance, however, this comes with increased power consumption. This trend of miniaturisation creates challenges in designing miniature versions of existing technologies.

This miniaturisation also creates many opportunities. Combining miniaturisation with the low-cost advantages of scale, more previously expensive technologies become more available for the general public. These technologies can be used for scientific, educational and commercial purposes. Furthermore, the costs can be reduced by increased use of Commercial of the Shelf (COTS) products. These are already existing components, usually used in other sectors and thus there is no need to design these components again [36]. The problem is usually that COTS products are not sufficiently reliable for space applications [6]. However, this risk can be mitigated by testing in representative environments to demonstrate fitness for purpose and reliability. Testing hardware for the environment for which they

[1] Parts of this chapter are taken from the Literature Study.

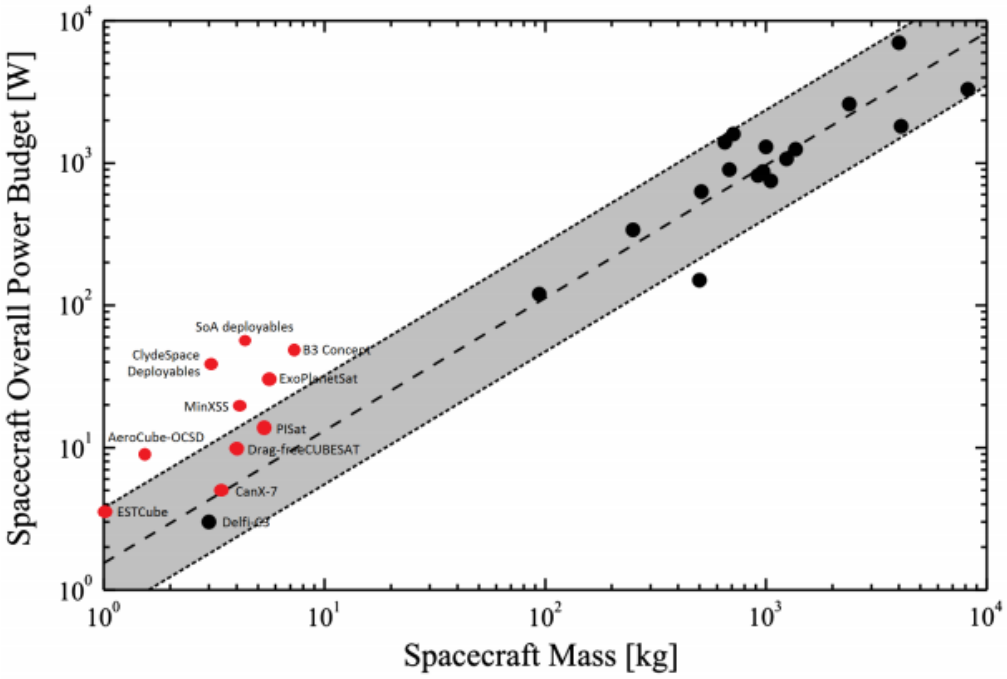

Figure 1.1: The relation between the power and mass of smaller satellites with bigger satellites, modified by [5] from [35].

were not designed, adds additional cost. The original goal of CubeSats was for educational purposes and technology demonstrations. Currently, because of the rise of CubeSats, they are used for other purposes as well [6]. More CubeSats are being launched with commercial goals, thus increasing the potential market of CubeSat products.

Miniaturisation could also be achieved by reducing the empty volume between the spacecraft systems and within these systems. The reason for this empty volume is typically for thermal reasons, accessibility reasons, etc. In addition to reducing component size, this space can also be reduced, or at least more efficiently managed, to achieve miniaturisation. Miniaturisation in this way reduces the total volume and, to a lesser extent, the total mass. However, it does not reduce the power consumption.

The distance between the stacked Printed Circuit Board (PCB) is decreasing, thus reducing volume. However, since the power usage is not much decreasing, the result is much higher power density [6]. Especially, since the now freed up space is filled with other instruments. This results in challenges for the design of the heat transfer path. More heat must flow from the source to the sink. (How to do this is not in the scope of this literature review. The different ways of transporting heat are explained and how this applies to CubeSat can be found in [5, 6]). This also means that more heat is put into the heat sink and thus must be dissipated away from the spacecraft to minimise operational temperatures which may contribute to failures.

1.1.2. High-performance CubeSat

Subsection 1.1.1 showed that as a result of the increased miniaturisation high-performance CubeSat will be used more in the future. This subsection analyses those CubeSats in terms of the power usage, the generation of that power and finally the implications of these two points.

Adding ion thrusters, high-power electronics, high-power transmitters, high-power optics, high-power payloads and more onboard processors increase the required power output and thus the amount of generated heat. With this increased required amount of power, also the power generation must increase. Figure 1.1 shows that small satellites have much higher power density than the larger ones. This trend will only increase.

Traditionally CubeSats have only body-mounted solar cells. For 1U and 3U CubeSats, this limits the power to a maximum of 5 and 12 W peak respectively. Recently, with the introduction of four hinged solar panels doubles the power for a 3U CubeSat to 25 W peak [27]. More research is performed over

the last years of how to equip CubeSats with large solar panels [8]. Clark [8] investigates CubeSats with 40 W peak power and 20 W average power. Furthermore, multi-hinged and solar pointing solar panels are under development and will increase the available power for a 3U CubeSat to 50 to 75 W peak [27, 29]. These increased power requirements will result in new challenges for the design of CubeSat.

From the accompanying presentation [8], Clark says that the increased power usage will be a problem for the thermal regulation. Current thermal dissipation requirements are limited to 40 W [28]. The amount of energy collected by the solar arrays will be between 50 and 75 W in the future. Most of this will result in heat generation. Thus the heat dissipation capabilities must be increased.

This section provided the trends currently in the space industry about miniaturisation and high-power CubeSats. There will be more CubeSats launched every year. Each will have more available power because of the miniaturisation and power-hungry subsystems. This will result in higher required heat dissipation requirements. Due to the limited space on the solar cells covered outside walls, a deployable radiator is a solution.

1.1.3. Problem validation

The proposed need is improved thermal rejection capability. A deployable radiator is a solution for this need. Because a deployable radiator improves the thermal coupling between the satellite and space by increasing the radiating area. The potential for radiators for CubeSats is that it increases the capabilities of CubeSats which were not possible before. Without radiators the performance of CubeSat is typically between 5 to 20 W [23] [2] while staying in a reasonable temperature range. Radiators allow the CubeSat to increase its capabilities. If the potential is reached, the benefits are CubeSats with higher performances. Quantifying these benefits is hard. But increasing the power with 50% the performances could also be increased with up to 50%. This is because more instruments can be used at the same time, more data can be send to Earth and more processing can be performed in-situ. Most of these benefits do require other improvements, most notably miniaturisation.

1.2. Research question

From the identified problem and potential solution, the research question follows:

Main research question *"What is the effect of an external radiator using High Performance Radiator (HiPeR) to the temperature progression of a CubeSat over the course of a polar orbit?"*.

This research question is meant to investigate the added benefit of an external radiator on the thermal performance of a CubeSat. From this research question, multiple smaller questions follow. These are listed below:

RQ-1: What is the influence of different radiator shapes to the temperature gradient?

RQ-2: How does the temperature gradient behave in the in-plane and out-of-plane directions of the surface of the radiator?

RQ-3: How does the temperature progression of the CubeSat behave over the course of a full orbit, with and without the radiator?

RQ-4: What is the influence to the temperature progression of the CubeSat for different orbits?

RQ-5: What is the influence of the thickness of the radiator to the temperature progression of the CubeSat?

1.3. Method

This thesis provides a solution to the problem addressed in Section 1.1. The solution to this problem is analysed individually, in a submodel for sizing and determining the optimal characteristics and the performance. The resulting design is analysed for the thermal performance of the radiator by a numerical model. This model is verified.

The solution integrated in a system is analysed in more detail for a specific case of a CubeSat mission in a system model. This second numerical system model is used for the analysis of the thermal performance of the radiator in a satellite system. Then this model is verified. Ideally, the radiator is

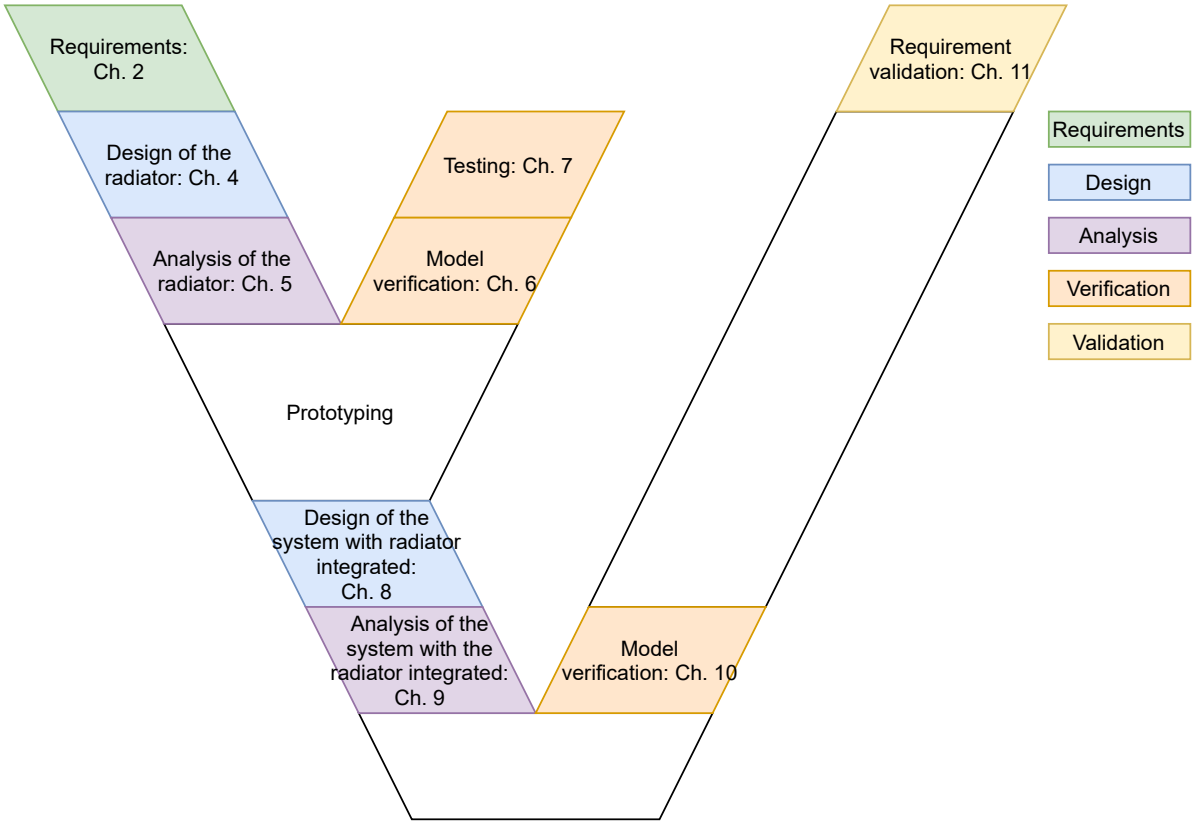

Figure 1.2: Overview of the method and chapters used in this thesis.

tested integrated in a system and with a simulated space environment. However, this is not possible due to test facility limitations. As an alternative, the radiator is verified by testing in a vacuum oven. For this test, the submodel is adapted for the test to verify the solution. Finally, the requirements are validated with the results from the verified numerical analyses. The outline of the method is presented in Figure 1.2. This model shows the bottom up analysis performed. The analysis, model verification and testing of the radiator design is first performed to optimise the design before analysing the performance of the radiator integrated in the system.

1.4. Thesis outline

This thesis report starts with the introduction in this chapter, Chapter 1. This chapter introduces the topic and explains the importance of CubeSats and the rise in its usage for various space applications. Next to the increased popularity for CubeSats, another trend is happening. This trend is the increase of power in CubeSats. This trend will influence various aspects of the (sub)system design, one of which is the thermal subsystem. This thesis will focus on one part of the thermal subsystem: the design of a radiator. A study case for which the radiator is designed is presented in Chapter 2, along with the top level requirements. Secondly, some literature about the state of the art is provided on the various elements used in this thesis in Chapter 3. Most of this is discussed in more detail in the Literature Study. With the problem explained in the introduction and with the requirements from the study case, a solution is proposed. This solution is generated and explained in Chapter 4. It is explained what design options were considered and how it influences the design. The thermal performance of this design is analysed and verified in Chapter 5. This analysis is performed with the thermal analysis tool ESATAN-TMS-2019. This chapter explains the assumptions taken for the numerical model. The results from the analysis are also discussed in this chapter. The verification on the model is performed in Chapter 6. A system test is not feasible. Therefore, the test is performed on the radiator model with a prototype of the radiator. The process and the test results are discussed in Chapter 7. The radiator solution is then integrated into a CubeSat system defined in the study case in Chapter 8. The thermal performance of

this solution integrated in a CubeSat system is analysed in Chapter 9, along with the sensitivity. The system model is verified in Chapter 10. In order to link the results of the analyses and verification back to the requirements, a validation is performed in Chapter 11. The results of the two numerical models and the tests with the prototype are concluded in Chapter 12, with some recommendations.

2

Study case and requirement identification

This chapter presents a study case in Section 2.1 for which a radiator is designed. From these functions, requirements follow. These requirements are identified and presented in Section 2.2.

2.1. Study case CubeSat model

The solution for the thermal problem for high-performance nanosatellites, is a radiator. This radiator will be used on CubeSat. Therefore, it is important to know for which CubeSats a radiator could be used. This section proposes a dummy CubeSat model for which the radiator can be used. This dummy CubeSat will also be the base for the system model CubeSat used for the system thermal analysis in Chapter 9. This section explains each part of the study case CubeSat model: the size, power consumption, power generation, payloads and orbit.

The most common CubeSat has a size of three standard units, shortened to 3U CubeSat.

Typical CubeSat have body-mounted solar cells and, sometimes, with additional deployed solar panels. However, these are all stationary. To get a higher power generation, deployable and Sun pointing solar arrays could be used. These solar arrays will be capable of delivering up to 75 W peak power [27, 29]. Using three panels of 10x30 cm^2 on each side of the CubeSat with solar cells could potentially provide 75 W. However, this is not feasible because of the orbit orientation and that not the whole panel could be covered in solar cells.

This large amount of available power is used to power the instruments on-board the CubeSat. From this peak power, it is estimated that the power consumption during day time operations is 30 W which is halved during eclipse time. This results in an equal heat generation.

The type of payload is not of much importance. Just the orientation of the satellite with respect to the Sun and Earth and the view angles of the satellite are important. It is assumed that there is a view angle on the bottom side of the CubeSat and that the bottom side must view Earth all the time.

Typical CubeSat orbits are in Low Earth Orbit (LEO). The inclination is depended on the launch location and available fuel. CubeSats launched from the International Space Station (ISS) have an inclination similar to the inclination of the ISS. CubeSat are usually launched as a piggy-back payload on larger satellite launches. These orbits are constrained to the primary payloads. New developments introduce dedicated launchers for smaller satellites which give more freedom in the choice of inclination. Most Earth observing satellites fly in polar orbits. When using such a high power CubeSat, it is expected that the mission could have more dedicated orbits as well. Therefore, this thesis assumes for this high-performance satellite in a polar orbit at 500 km.

To summarise, these assumptions are listed below:

- 3U CubeSat with large Sun-pointing solar arrays
- 30 W heat generation distributed evenly on a stack of PCBs and two payloads
- Halved heat generation during eclipse
- Polar orbit at 500 km

Table 2.1: Requirement identifier legend

Requirement identifier abbreviation	Explanation
DRW	Deployable Radiator Wing
Per	Performance
Pod	Poly-Picosatellite Orbital Deployer
Sto	Stowage
Dtc	Deployment constraints
Ddc	Deployed constraints
CSc	CubeSat constraints

2.2. Requirements

The function of the radiator is to dissipate heat from the satellite to prevent the satellite from overheating. From this function, the requirements follow. Table 2.1 show the meaning of the identifiers for the abbreviations used in the requirements.

Part of the heat generated internally and received from external sources, is released via the radiator. The maximum heat dissipation per 10x10 cm^2 face at a temperature of 30°C is 4.8 W, from the Stefan-Boltzmann law in Equation 2.1 [37]. The energy required to radiate is the added capability of what the maximum is of what typical CubeSat are able to do [2]. This amounts to 10 W (DRW-Per1). To radiate this heat, a large surface is required, more than one side of the CubeSat of 100x100 mm^2 (DRW-Per2). Since the area on the surface of the CubeSat is limited, the radiator should be external to have a more efficient CubeSat surface usage and to maximise radiating power (DRW-Per3). Furthermore, it should be deployable to create a large surface outside the CubeSat (DRW-Dpl1).

$$Q = A\sigma\epsilon T^4 = 0.1^2 * 1 * 5.67 * 10^{-8} * (273.15 + 30)^4 = 4.8\ W \tag{2.1}$$

DRW-Per1 The radiator shall radiate at least 10 W.

DRW-Per2 The total area of the radiator shall be larger than 0.01 m^2.

DRW-Per3 The radiator shall be located on the outside of the CubeSat.

DRW-Dpl1 The radiator shall be deployable.

The cost of launching satellites is high. In order to keep this cost low, the mass should be low. Adding a mass at large distance from the centre of mass, increases the mass moment of inertia. This high mass moment of inertia makes the satellite more resistant against rotation. A high mass could lead to a reduced capability of the attitude control. Therefore, the mass shall be minimised. An educated guess of a maximum of 100 g is assumed DRW-Per4.

DRW-Per4 The radiator shall have a mass of at most 100 g.

The radiator uses volume on the inside and outside of the CubeSat. This requires constraints on the used volume. Inside the CubeSat, the radiator should not exceed the available CubeSat stowed volume (DRW-Sto1). CubeSats are stored typically in a Poly-Picosatellite Orbital Deployer (P-POD) [17]. These storage devices keep the CubeSat safe during the launch of the rocket. Since CubeSat have standardised dimensions, these P-PODs have standardised dimensions too. Therefore, the radiator should be compatible with P-PODs. A CubeSat with any deployable equipment, should fit in the P-POD (DRW-Pod1-Sto2). For storage and during launch, the CubeSat is inside a P-POD. To fit inside the P-POD the deployable radiator shall be folded (DRW-Dpl1-Sto5). The volume in the P-POD is limited and the ISISPOD from ISISpace [15] allows 9 mm on the sides (DRW-Pod1-Sto3). This is more than the 6.5 mm that other P-PODs allow [22]. The CubeSat is supported inside the P-POD on guide rails [15]. Regulations require the rails to have a width of at least 8.5 mm [22]. The CubeSat Design Specification, [22], also allows 25% of the rail on the CubeSat not to contact the rails of the P-POD. The deployable radiator should not interfere with the guide rails (DRW-Pod1-Sto4).

DRW-Sto1 The radiator shall not exceed the available CubeSat stowed volume allowables.

DRW-Pod1 The radiator shall be able to be stored in a P-POD.

DRW-Pod1-Sto2 The radiator shall not exceed the available stowed volume allowables of the P-POD.

DRW-Pod1-Sto3 The radiator shall extend in folded configuration at most 9 mm from the surface of the CubeSat.

DRW-Pod1-Sto4 The radiator in folded configuration shall not interfere with the rails of the CubeSat while stowed inside the P-POD.

DRW-Dpl1-Sto5 The radiator shall be foldable.

The radiator should be deployed only after it is released from the P-POD. Accidental deployment before CubeSat release should be prevented (DRW-Dpl1-Dtc1). Otherwise it could damage the P-POD, the radiator itself or other deployables of the CubeSat such as the solar arrays. The radiator should not add unnecessary complexity to the system. Therefore, the radiator shall be deployed passively (DRW-Dpl1-Dtc2).

DRW-Dpl1-Dtc1 Accidental deployment before CubeSat release shall be prevented.

DRW-Dpl1-Dtc2 The radiator shall be deployed passively.

The radiator is deployed volume on the outside of the CubeSat. This could cause interference with other deployed volumes such as the solar arrays and antennae. Therefore, the radiator should not interfere with these subsystems (DRW-CSc1). When the CubeSat accelerates in either transnational direction or rotation, the deployed radiator should not bend (DRW-Dpl1-Ddc2 and DRW-Dpl1-Ddc3). This bending becomes dangerous when the hinges fail or when the radiator is so flexible that it could hit other subsystems. More detailed requirements are not possible to define at this stage. These requirements depends on the materials, shape and structure.

DRW-Dpl1-Ddc1 The radiator shall not interfere with other deployed subsystems.

DRW-Dpl1-Ddc2 The hinges of the radiator shall not bend due to a lateral acceleration.

DRW-Dpl1-Ddc3 The hinges of the radiator shall not bend due to a rotational acceleration.

The deployable radiator is part of the whole CubeSat. The function of the radiator is to radiate the heat from the heat producing instruments of the CubeSat to space. Therefore, the internal environment shall be connected to the radiator via a thermal link and interface (DRW-CSc1).

The radiator has an influence on other CubeSat subsystems. These subsystems need extra requirements. The attitude actuation should be active (DRW-CSc2) because it is assumed that the solar arrays are Sun pointing and the instruments require Earth view, as explained in Section 2.1.

The thermal link between the internal environment of the CubeSat and the radiator creates a heat path with low thermal conductivity. When the internal heat load, and thus temperature, is high, excess heat is radiated easily away. When the internal heat load is low the temperatures are low too. Still, the high conductive thermal link provides an easy heat path to space. This could result in low temperatures for the internal environment. This could be solved for example by designing the thermal link such that the conductivity is less when the temperature is low. The design of the thermal link is out of the scope of this thesis project. Therefore, this problem too. Nonetheless this problem is addressed in requirement DRW-CSc3.

DRW-CSc1 The interface shall link the radiator with CubeSat internal environment with a thermal link.

DRW-CSc2 The attitude actuation shall be active.

DRW-CSc3 The radiator shall prevent temperatures below 0°C.

Figure 2.1 provides an overview of all the requirements and their dependencies.

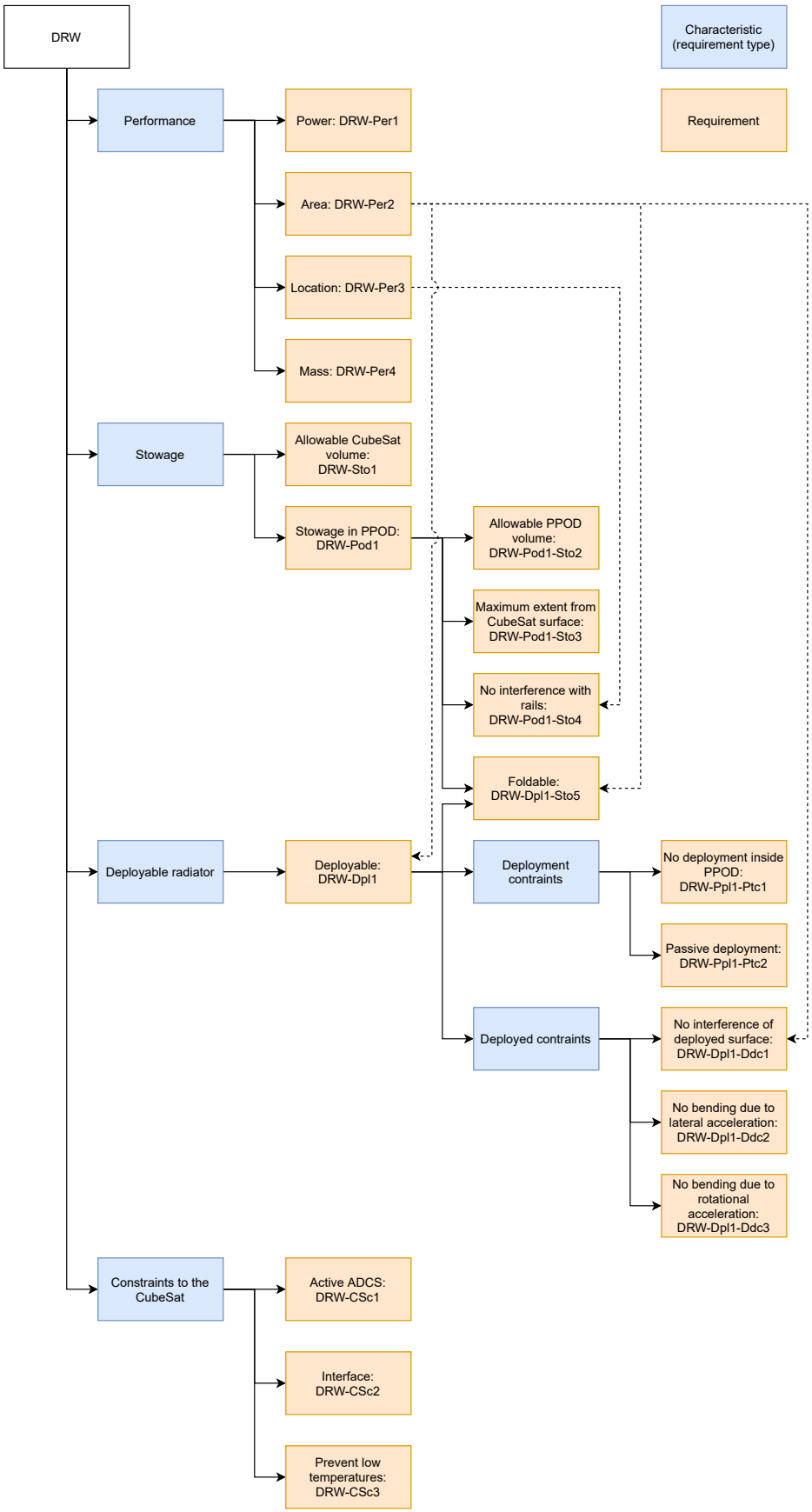

Figure 2.1: Overview of the requirements by characteristic including small description and the requirement identification code.

3

State of the art

The design follows the function and requirements of the radiator presented in Section 2.2. The design follows in the next chapter. This chapter presents most of the possibilities for the design, which could be used to construct a solution to the research question about how to solve the thermal control problem. Since most of this research is already performed in the Literature Study prior to this thesis, this chapter will provide a concise overview of the Literature.

This chapter starts in Section 3.1 with the explanation of the solution Airbus Defence and Space Netherlands designed for distributing heat efficiently. Section 3.2 explains the two methods of deploying the radiator: active and passive deployment. This section concludes that the use of passive deployment is preferred over active deployment. Section 3.3 provides more background information about a type of passive deployment option: the tape spring. This chapter is concluded with a concise summary in Section 3.4.

3.1. High Performance Radiator

High Performance Radiator (HiPeR) is a lightweight semi-flexible radiator solution developed by Airbus Defence and Space Netherlands. The functional material is Pyrolytic Graphite (PG). This material has high in-plane thermal conductivity and low mass density properties. HiPeR is a semi-flexible laminate of PG sheets laminated with a adhesive and a protective Kapton sheet on both sides, see Figure 3.1. The similar, non-laminated technology has already been flown as a thermal strap [21], thus reaching a Technology Readiness Level (TRL) of 9. This laminate is flexible and it is able to bend around corners.

PG has an in-plane conductivity of 1350 W/mK and the out-of-plane conductivity is 3.5 W/mK for sheets with a thickness of 40 μm [25]. The out-of-plane conductivity is much lower than the in-plane conductivity because the carbon atoms are laid in the in-plane direction. Also, the in-plane conductivity of PG is temperature dependent, see Figure 3.2. Furthermore, the conductivity depends on the thickness of the sheets, the thinner the sheets the higher the conductivity is [25]. However, the data collected in Figure 3.2 used PG with an unknown thickness. It is assumed that the gradient of the thermal conductivity with respect to temperature is constant for different thicknesses of PG. The conductivity of PG is higher than that of aluminium or copper, which is typically in the range of 170 to 400 W/mK respectively. Furthermore, the density is lower than that of those metals, resulting in an even lower specific conductivity. Multiple PG sheets can be laminated together to improve the heat transfer capability. Even though the out-of-plane conductivity of the PG and adhesive is low. Since the sheets and the adhesive are thin and the area large, the out-of-plane temperature gradient over many layers is low. The thickness of a PG sheet is 40 μm [25]. Airbus Defence and Space Netherlands uses Kapton sheets to cover the fragile PG sheets [21].

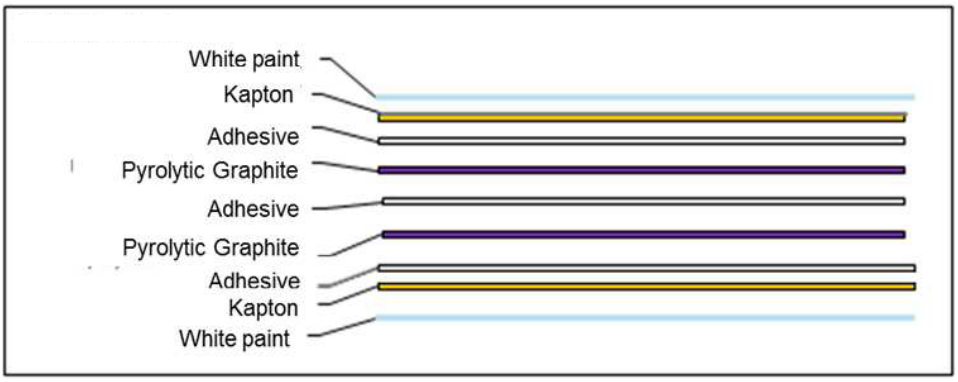

Figure 3.1: Cross-section of the HiPeR laminate with each of its layers explained [21].

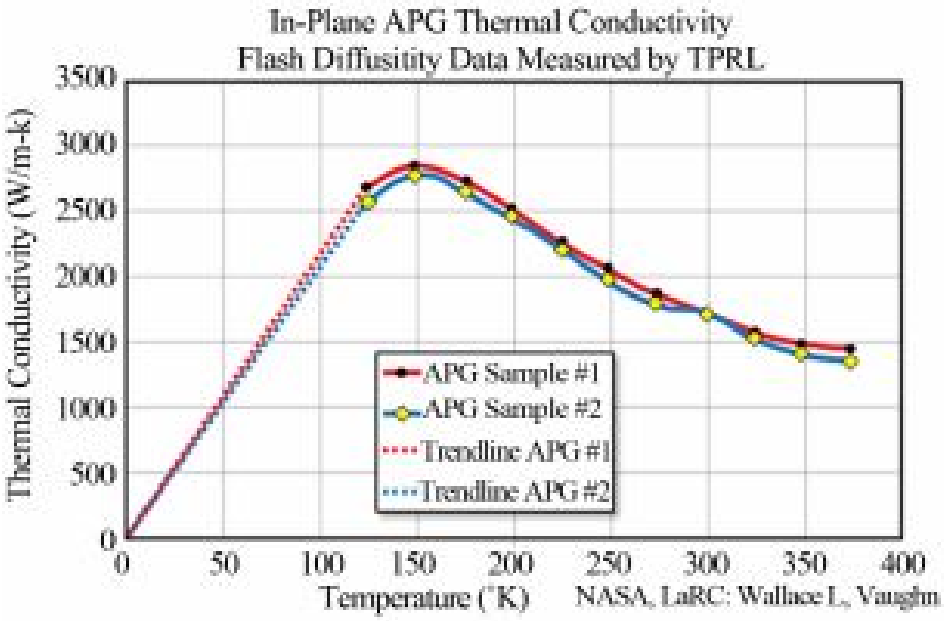

Figure 3.2: The temperature dependency of the thermal conductivity of PG [1].

3.2. Deployable radiator design options

From requirement DRW-Dpl1 and DRW-Dpl1-Dtc2 the radiator shall be deployable and be deployed passively, respectively. Passive deployment means that the deployment is not active, hence the deployment requires no electrical energy. This excludes all deployment systems that require electrical energy, such as motors. Passive deployment systems can make use of the stored potential energy in springs. There are many type of spring deployment systems for space applications. The Literature Study prior to this thesis, revealed that using the the tape spring would be the most suitable option to use in this design. Section 3.3 provides more information about the working of the deployment of these tape springs.

3.3. Deployment of tape spring hinges

A tape spring is a thin strip with a slightly curved cross-section, often used as tape measure. This curvature provides more stiffness than a flat plate. In this curved state, there are no internal stresses [33]. The higher moment of inertia of the curved shape, makes the tape spring more resistant against bending. When flattening the curve by pushing the sides down, the moment of inertia reduces and it becomes easier to bend and thus fold the tape spring hinge. Bending the tape spring introduces internal stresses. The flat strip wants to form to the neutral, curved state. This build up potential energy could

Figure 3.3: Folding of a tape spring [26].

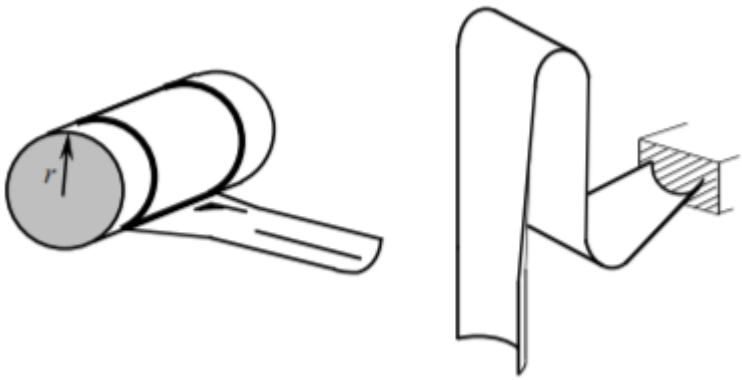

Figure 3.4: Two different ways of folding the tape spring [31].

be used for actuating the folded structure, back to its neutral state. The possibility to flatten the tape spring and then folding it to make foldable structures results in a hinge, the so-called tape spring hinge. Because of the potential energy stored when folding it, these hinges deploy passively upon releasing.

3.3.1. Bending behaviour of tape springs

A tape spring is able to be bend in two ways. The first is the opposite sense bending, as shown in Figure 3.5. The second is the equal sense bending, as shown in Figure 3.6. The behaviour of bending and releasing the tape spring is non-linear [31] and follows the graph in Figure 3.7. Starting in point O in Figure 3.7, the origin, and bending the tape spring in the opposite sense, follows the blue line to point A. When the moment increases, the angle increases and the tape spring flattens. At point A, the tape spring suddenly looses it's curved shape and becomes flat. Then it only curves locally in the longitudinal direction around the flattened area and the rest of the tape spring is straight, see Figure 3.3. When the tape spring clicks (point A, Figure 3.7), the bending moment decreases and follows the line to point B. When increasing the angle further, the angle still increases, but the moment remains constant to point C.

The tape spring behaves different in the reverse direction. To bring the tape spring back in the neutral position, e.i. curved, the bending angle should be reduced. This is seen in Figure 3.7 by following the red line from point C to B. The bending moment stays constant until point D. This is instead of following in the same way back to point A, with an increase in bending moment and a constant bending angle. This happens because the tape spring stays flattened at the bent part. At point D the tape spring clicks to point E and the localised flattening and bending disappears. Finally, following the path back to the origin, unloads the tape spring.

For bending the tape spring in equal sense, the relation between the moment and the (negative) bending angle is linear and has the same slope as for the opposite sense [10]. Bending the tape spring to a negative angle, the green line is followed from the origin to point F, as depicted in Figure 3.7. At point F, the tape spring buckles, but there is no click and the behaviour stays linear with increasing bending angle. The moment required to reach this buckling is lower than the moment required for buckling when bending in the opposite sense. The tape spring flattens and a local bend forms in a

ht

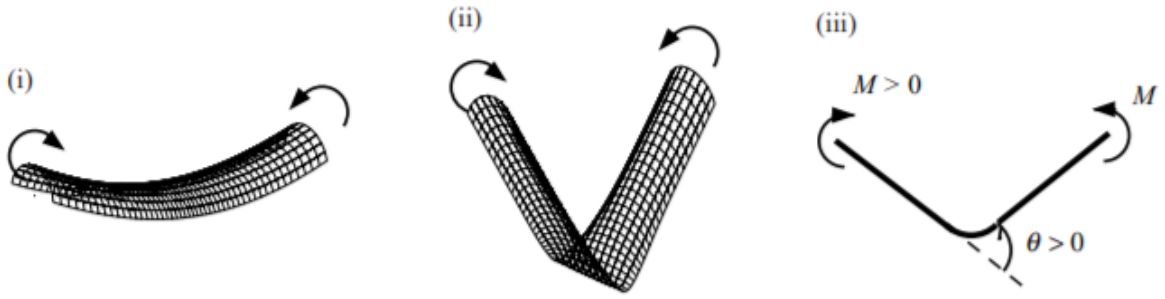

Figure 3.5: Opposite sense bending of a tape spring [31].

ht

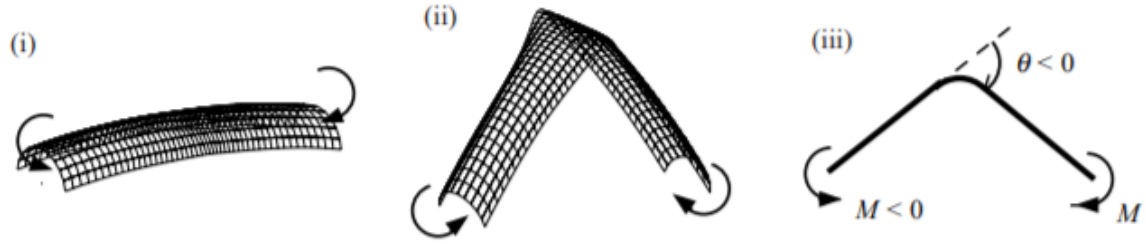

Figure 3.6: Equal sense bending of a tape spring [31].

similar manner as for opposite sense bending. The reverse behaviour follows the same line back to the origin, this is commonly assumed according to [10].

3.3.2. Deployment overshoot of tape springs

The potential energy stored during the bending of the tape spring into the stowed configuration, is released as kinetic energy during deployment. As a pendulum in the middle point, there is no potential energy but a still kinetic energy left. This energy is enough to let the pendulum swing the other way and to transfer it to potential energy again. The same is true for tape spring. This kinetic energy must be more than the energy required to go past point F in Figure 3.7. If that is the case, the tape spring will bend in the equal sense, thus transforming kinetic energy to potential energy. For releasing the tape spring from the equal sense bending more potential energy is required because the angle and required moment is much higher, see point A in Figure 3.7. Therefore, releasing the tape spring from an equal sense bending position, will hit a full stop around the origin in Figure 3.7 and thus a shock wave is introduced into the system. Releasing the tape spring from an opposite sense bending, will cause the tape spring to overshoot and then bend in equal sense for it to go back. When it goes back and it does not have enough kinetic energy to pass the clicking point, it will stop and a shockwave is formed.

3.3.3. Guiding and damping of deployment

The tape spring hinge will overshoot when released from the opposite sense bending position as explained in Subsection 3.3.2. This overshoot may not be favourable since it could damage systems on the wall of the CubeSat or other deployed structures. To reduce the overshoot, energy must leave the system during deployment. This can be achieved by introducing a dampening system. This must be done on the interval between point E and F in Figure 3.7, such that the energy required, does not exceed that of point F.

Another way to reduce or remove the overshoot is to introduce two tape spring hinges facing each other in equal sense.

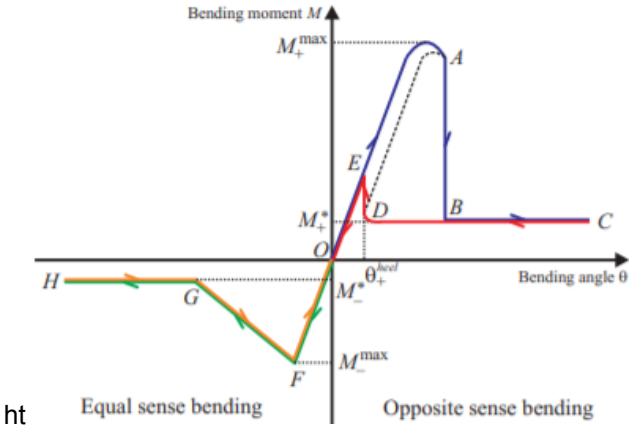

Figure 3.7: The relation of the bending moment and the bending angle when bending a tape spring [10].

The behaviour of the tape spring hinge is chaotic upon release. This is especially the case during the overshoot. To reduce the chaotic behaviour, the overshoot could be reduced or the deployment could be guided.

3.4. Chapter summary

This chapter provides background information on the elements used for a solution of the thermal control problem. HiPeR provides a high conductive material to spread the heat over a large surface. However, this is not stiff on itself. Therefore, it needs a supporting structure. This structure requires the possibility to fold. A tape spring provides the stiffness required, while also allowing for folding and passively-actuated deployment.

4

Design of the Deployable Radiator Wing

This chapter explains in depth the design of the solution to the thermal control problem for high powered CubeSat: the Deployable Radiator Wing (DRW). It starts in Section 4.1 by identifying the various design options. From these design options a selection is made, covered in Section 4.2 to 4.7. Some of these design options were already performed in the trade-offs in the Literature Study prior to this thesis and will not be covered in depth here. It was found in the Literature Study that the shape of the DRW did not have an appropriate analysis. Therefore, this is done in Section 4.7. Section 4.8 explains the heat interface. Section 4.9 provides additional information on the possibilities of the scalability of the DRW. This design, however, could create problems for the functioning of other spacecraft elements. This is explained in Section 4.10.

4.1. Design options for the DRW

Before designing the DRW, the potential options should be identified. These options are presented in a DOT which is shown in Figure 4.1, 4.2 and 4.3. The design options can be subdivided into six options: material (Section 4.2), folding and stowing (Section 4.3), radiator structure (Section 4.4), deployment (Section 4.5), thermo-optical surface finish (Section 4.6) and shape (Section 4.7). Each of the six elements of the DRW is explained in the section noted as before. Even though the shape of the radiator is not a design option but an optimalisation, it is included in the DOT because optimisation performed in Section 4.7 is for maximising the surface area. Some CubeSat may not require such a large area. Nonetheless, Figure 4.2 presents the possible shapes.

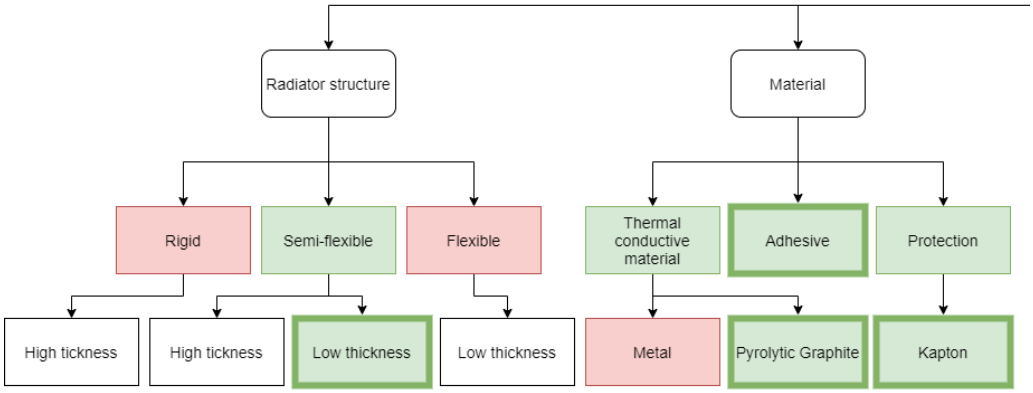

Figure 4.1: The DOT for the radiator structure and material for the DRW.

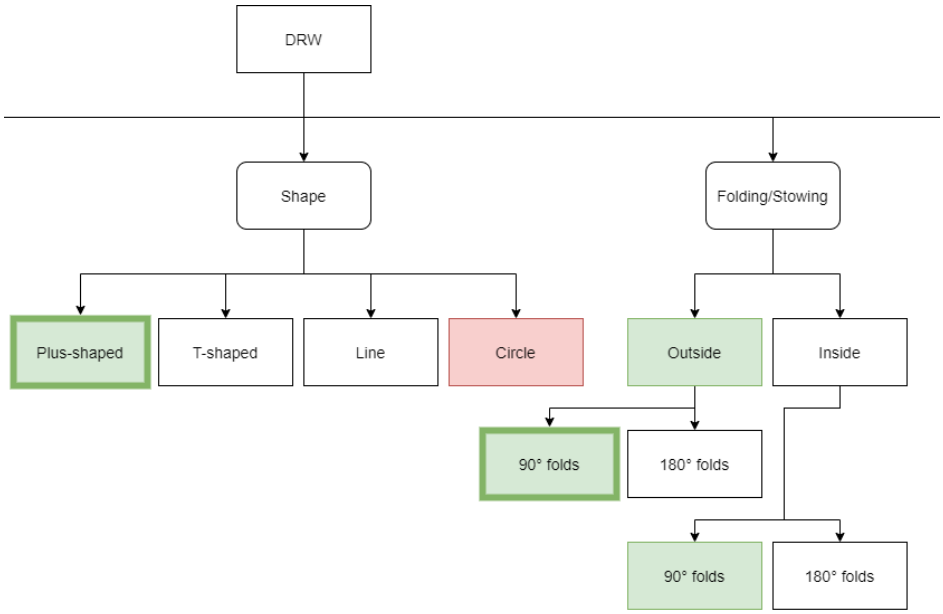

Figure 4.2: The DOT for the shape and the folding/stowing method for the DRW.

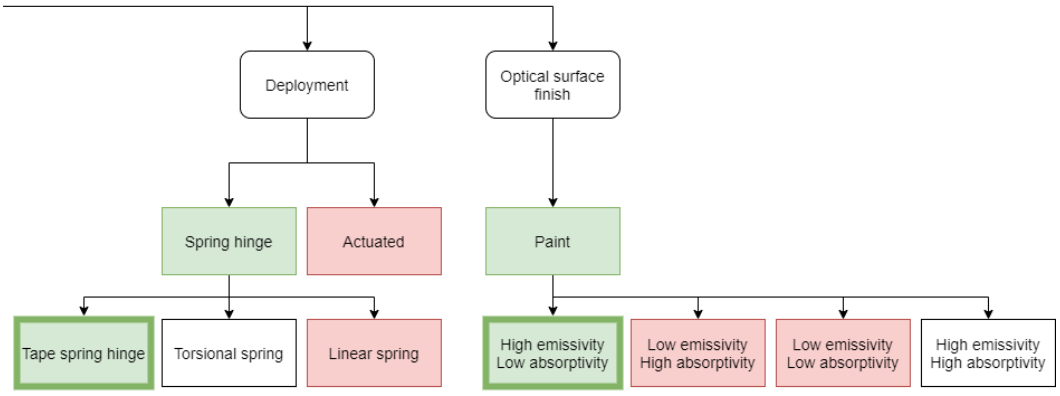

Figure 4.3: The DOT for the deployment mechanism and the type of thermo-optical surface finish DRW.

4.2. Material

Figure 4.1 shows the design options for the material that is used to conduct heat through, the adhesive to adhere or connect the various materials and a cover material to protect the product. The goal of the thesis is to investigate applications for a deployable CubeSat radiator using HiPeR developed by Airbus Defence and Space Netherlands. HiPeR is a semi-flexible material consisting of multiple, adhered layers of of the highly conductive material PG. However, other materials with high conductivity, such as metals, could be used. Using HiPeR will have implications but also opportunities, which rigid and fully flexible materials do not have.

HiPeR is a laminate consisting of adhered layers of PG sheets with a protective top and bottom layer of Kapton. This laminate HiPeR is developed by Airbus Defence and Space Netherlands. PG is explained in Subsection 4.2.1, Kapton is explained in more detail in Subsection 4.2.2 and finally Subsection 4.2.3 covers the adhesive.

4.2.1. Pyrolytic Graphite

The conductivity of PG is not constant with respect to temperature. The highest conductivity is at a temperature of 150 Kelvin and decreasing almost linearly with increasing temperature as depicted in Figure 3.2. For small temperature differences, the temperature has only a small influence on the thermal conductivity. Figure 4.4 shows the thermal conductivity of various materials used for distributing heat over surfaces. It is clear that PG outperforms all other materials.

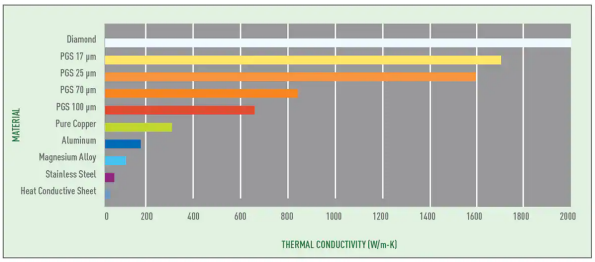

Figure 4.4: Comparison of PG to various materials used for distributing heat over surfaces.

4.2.2. Kapton

Kapton is a polyimide film that is used within Airbus Defence and Space Netherlands and the aerospace industry. Within Airbus Defence and Space Netherlands it is used as protective cover for the thermal FlexLinks and HiPeR [21]. The Kapton protective sheets are covered with white paint for optimal thermo-optical performance with high emissivity and low Sun absorbtivity.

4.2.3. Adhesive

The purpose of the adhesive is to adhere the stacked layers of PG and Kapton protective sheets. Thus it must stick to those materials. Since adhesives have generally low conductivity, these layers must be as thin as possible. Furthermore, since the space environment induces high temperature differences and high rates of bombardments with radiation and particles, the adhesive must withstand these as well.

Within Airbus Defence and Space Netherlands the adhesive 3M966 is used for more prototypes to adhere the HiPeR laminate. Its properties are listed in Table 9.2.

4.3. Folding and stowing

The radiator should be larger than one square of a CubeSat unit (requirement DRW-Per2). This large flat surface would not fit in a deployed configuration in the launch pod. Therefore, it must be stowed in the available volume of the CubeSat. Stowing it inside the CubeSat, the surface must be folded. Folding it in a small volume, the radiator must make 180° folds, see Figure 4.5. Folding it for 90°, see Figure 4.5, the stowage volume will be larger and, therefore, this is not a desired option. Stowing it on the outside of the CubeSat, saves space inside. Folding the radiator as a package with 180° folds, could end up too thick. This would cause the CubeSat not to be able to fit in the launch pod anymore. Wrapping the radiator around the CubeSat and, therefore, covering multiple faces is more efficient. This saves space on the inside and increases the width and height less than folding it on the outside. The radiator will make 90° angles in this case.

HiPeR could be produced with hinge elements to allow for a localised low radius of curvature. Without these hinge elements for any practical applications for CubeSat, the radius of curvature is too large and highly dependent on the amount of layers used. The hinge elements increase folding capabilities by not adhering the PG sheets in some sections. This allows for a much smaller radius of curvature. Allowing for the folding of the DRW, requirement DRW-Dpl1-Sto5. The thin PG sheets could tear and break. Therefore, HiPeR has a protective sheet of Kapton on the top side and the bottom side.

Storing the DRW over the outside surface of the CubeSat will influence the possibilities to use those surfaces for other applications. Furthermore, the CubeSat is stored in a CubeSat P-POD. Usually CubeSat are stored in this box on a rail for easy ejection. These rails are on the corners of the CubeSat. The rails can only be covered up to 25% of the length [22]. However, the DRW will extent to up to one-third of the rails. Thus, covering the rails with the folding of the DRW is not feasible. This will also satisfy requirement DRW-Pod1-Sto4.

Instead of folding it over the outsides, it could be folded inside a box. This box can be placed inside the CubeSat. This way of storing gives more flexibility for the location of the radiator on the CubeSat. However, this way of storing decreases the volume inside the CubeSat and has potentially a higher mass due to the required casing.

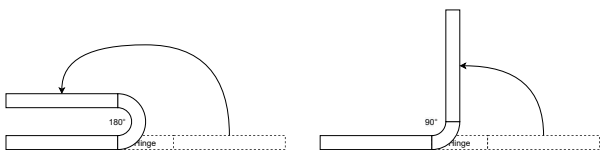

Figure 4.5: Schematic view of folding the DRW over 180°and 90°angles.

4.4. Radiator structure

The radiator structure provides stability and structural integrity for the radiator, in stowed and in deployed configuration (requirements DRW-Dpl1-Ddc2 and DRW-Dpl1-Ddc3). Rigid panels provide high structural integrity, whereas flexible panels do not. Semi-flexible panels provide lower rigidity but allow for some flexibility. Some flexibility is needed to allow for the folding and stowing of the radiator, as explained in Section 4.3.

HiPeR is semi-flexible, so it might be able to provide part of the structure itself. However, the parts that require more flexibility need an external structure. This external structure could also be used as a potential hinge. See more on this in Section 4.5.

4.5. Deployment

There are two principles to deploy the radiator. The first principle is active deployment actuation which requires power to operate. The second principle, the opposite, is a passive deployment actuation and does not require any power to operate. The deployment of the radiator should be passive, see requirement DRW-Dpl1-Dtc2. This means that only passive deployment actuation is possible. There are multiple types of passive deployment actuation. These are shown in the Design Option Tree (DOT) in Figure 4.3.

4.6. Thermo-optical surface finish

Radiators need to radiate as much heat as possible to their surroundings. Two properties influence the efficiency of radiating and absorbing heat: the emissivity and the absorbitivity. These two properties have values between 0 and 1. To simplify, the values of these properties are shown in Figure 4.3 as high and low.

To radiate more heat, the radiator requires a surface finish with high emissivity. It is preferable to keep radiators outside direct sunlight, but this is not always possible. To prevent the radiator from absorbing too much heat from the Sun, the absorptivity should be low. Therefore, the optimal surface finish for a radiator has a high emissivity and low absorptivity [18].

4.7. Shape of the Deployable Radiator Wing

There are multiple possible shapes for the DRW. A tool ESATAN-TMS-2019 is used for calculating the temperatures for the different shapes of the radiator. It is important that the total area of the radiator is larger than one face of the standard unit CubeSat. In order to achieve a large surface, it should extend from the CubeSat. It is important to consider that it should still be able to be folded into a surface smaller than one face of the standard unit CubeSat for stowing purposes (requirement DRW-Dpl1-Sto5). An overview of the design options is presented in Figure 4.2. In this section the most optimal shape for the deployable radiator is explained.

In order to get the maximum heat flow from the interface to space the following parameters are of importance: thermo-optical properties, material heat transfer and area. Each of these must be as high as possible. The thermo-optical property emissivity, close to its maximum of 1, results in a higher radiated heat transfer to its surroundings, as explained in Section 4.6. Materials with high conductivity increases the heat flow through the material, as explained in Section 4.2. The heat spreads from the heat input via the interface over the surface of the material. If the conductivity is not infinite, the temperatures decrease further away from the interface. Since radiative heat transfer is proportional with the temperature to the fourth power, the higher the temperature of a surface, the higher the emitted thermal energy is. Equation 4.1 shows the emitted thermal energy from a surface [37].

$$Q_{radiative} = \epsilon A \sigma T^4 \tag{4.1}$$

The most optimal shape, in terms of heat output per unit of area (or mass), is any area with an area heat source with the size of the whole area. However, this is unrealistic. With a point heat source, the most optimal shape is a circular disc with the heat input (interface) in the centre. This means that the heat flows radially outwards with constant temperature over the concentric circles, see Figure 4.12. This shape is inefficient to fit on a CubeSat because of inefficient folding and storing reasons, therefore,

another shape must be determined. To analyse the behaviour to find the optimal shape for the DRW, multiple models are proposed that would simulate the initial circular disc. This section assumes a model of a 1 mm thick disc with a radius of 15 cm and a conductivity equal to PG of 1350 W/mK. The interface has a temperature of 20°C and the surrounding temperature of deep space is -270°C.

The disc has to fit the satellite on the outside (requirement DRW-Per3). Requirement DRW-Per2 states that the minimum area shall be larger than one face of a standard unit CubeSat: 10x10 cm^2. Assuming a standard CubeSat with sides of 10 cm, the 30 cm diameter disc is too big. This will not fit in the launch dispenser where CubeSats are stored during launch. Hence, the radiator has to be smaller (diameter less than 10 cm) or foldable. However, the radiator should have a diameter larger than 10 cm per requirement DRW-Per2. Thus, the radiator shall be folded (DRW-Dpl1-Sto5. How to fold the radiator depends on the attachment point, thus the interface. The interface is the location where the excess heat of the satellite flows into the DRW. There are two possible locations for the interface on the disc: in the centre of the disc, see Figure 4.6 and on a side of the disc, see Figure 4.7. When folding a disc over a cube, the disc will wrinkle at the corners of the cube. This extra material causing the wrinkles, has to be removed. In Figure 4.8 and Figure 4.9 the red squares indicate the area to be removed. Now, the resulting geometry is shaped as a plus, see Figure 4.10 and Figure 4.11.

The temperature maps of the disc with the boundary condition of 20°C are shown in Figure 4.12 with the interface in the centre of the disk and Figure 4.13 with the interface on the positive x-axis. As described earlier, the shape has to be changed in order to account for the folding of the radiator. First, two cut-outs for two corners are made, as shown in Figure 4.8 and Figure 4.9. This results in Figure 4.14 with the interface in the middle and Figure 4.15 with the interface on the positive x-axis. This allows the radiator to be fold over one axis. However, it will still not fit inside the launch pod, since the semicircle has a radius of 20 cm. The radiator must be folded over the cube so that five out of its six sides are covered. Thus, four cut-outs are needed as presented in Figure 4.8 and Figure 4.9. The resulting temperature maps for the two different configurations are shown in Figure 4.16 with the interface in the middle and Figure 4.17 with the interface on the positive x-axis side. The difference in temperature map for the two locations of the interface will be further discussed in Section 4.8.

The shape of the disc with the four square cut-outs is similar to a plus-shape, see Figure 4.10 and Figure 4.11. To convert the model to the new shape, a square grid with the heat input in the centre or on the side is implemented, see Figure 4.20 and Figure 4.21.

The efficiency of the radiator in terms of power per unit area increases when the area is smaller. This is because the finite conductivity makes the points further away from the interface colder than the points close to the interface. Reducing the area and, thus, the distance to the interface, increases the efficiency. It is also observed that more cut-outs will increase the temperature in the flaps (the legs of the plus) and in centre as well. When comparing Figure 4.12 with Figure 4.14 the flap that results after the cut-outs has a higher temperature than the semidisc on the other side of the centre. Furthermore, after the four cut-outs, see Figure 4.16, the temperature on the flaps is even higher. This is also observed in Figure 4.18, Figure 4.20, Figure 4.22, Figure 4.19, Figure 4.21 and Figure 4.23. This behaviour is caused by the decrease in total area, but no decrease in the heat load boundary condition. To radiate the same heat load at the boundary condition with a smaller area, the temperature must be higher to compensate for the loss in area. This is shown with the use of Equation 4.1. In contrast, for the disc with the interface on the sides this is not the case, see Figure 4.13 and Figure 4.15. This is probably caused by the fact that the cut-outs reduced the heat path to the other side. However, the cut-outs of the shapes with the interface in the centre do not cut the heat flow paths to the outsides. This might also explain why the temperature profile of Figure 4.15 and Figure 4.17 are almost identical; there are no heat flow paths cut by the extra two cut-outs.

For designing the radiator, PG is used. The PG used for the prototype, has a fixed width. Because of this width, the plus-shape is not possible. That is why the radiator is designed in a T-shape, with three flaps, instead of the plus-shape with four flaps. The T-shape reduces the total area and because of that also the performance decreases. The radiator with T-shape is still usable for the CubeSat.

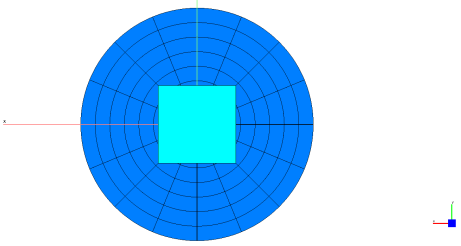

Figure 4.6: Disc with interface location in cyan in the centre.

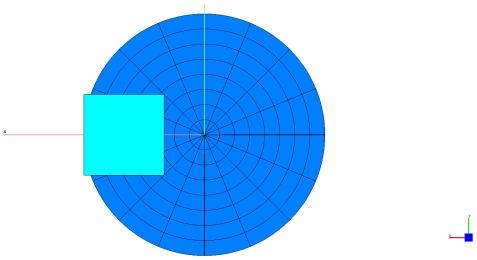

Figure 4.7: Disc with interface location in cyan on the side on the positive x-axis.

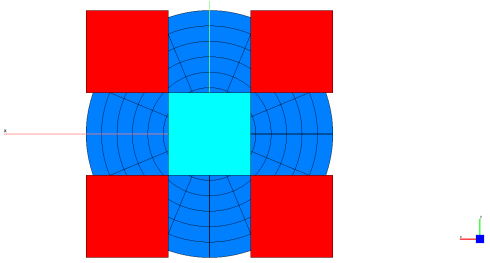

Figure 4.8: Disc with interface location in cyan in the centre and the corners to be removed in red.

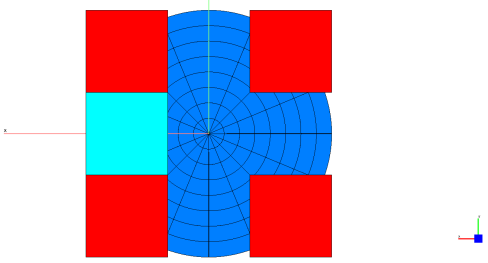

Figure 4.9: Disc with interface location in cyan on the side on the positive x-axis and the corners to be removed in red.

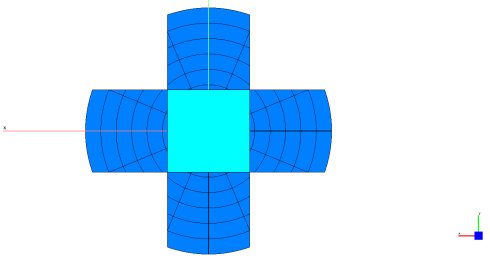

Figure 4.10: Disc with the cut-out corners with interface location in cyan in the centre.

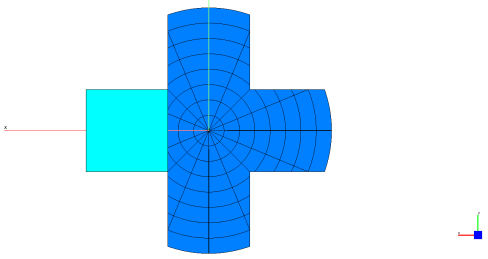

Figure 4.11: Disc with the cut-out corners with interface location in cyan on the side on the positive x-axis.

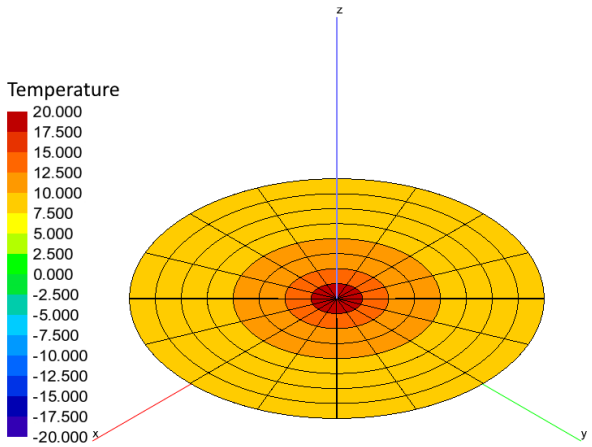

Figure 4.12: Disc with constant temperature in the centre.

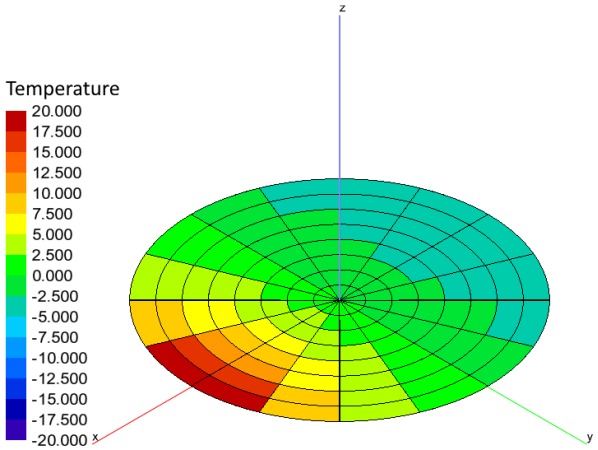

Figure 4.13: Disc with constant temperature at one of the sides.

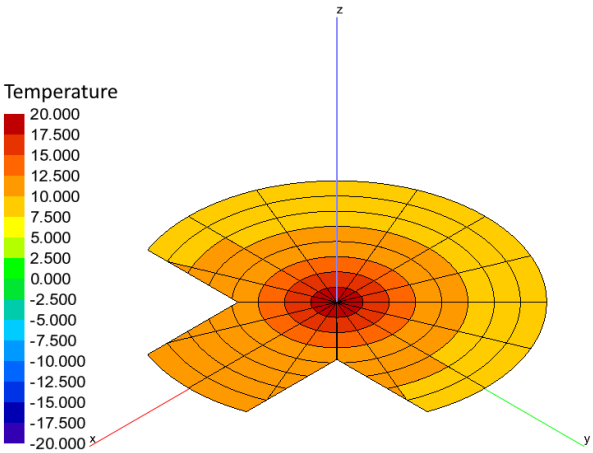

Figure 4.14: Disc with constant temperature in the centre with 2 square cut-outs.

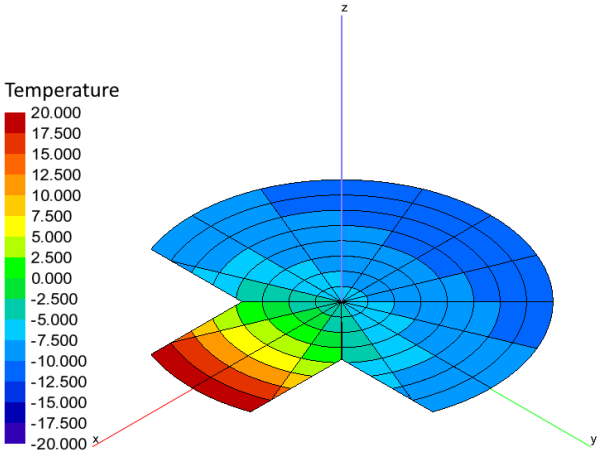

Figure 4.15: Disc with constant temperature at one of the sides with 2 square cut-outs.

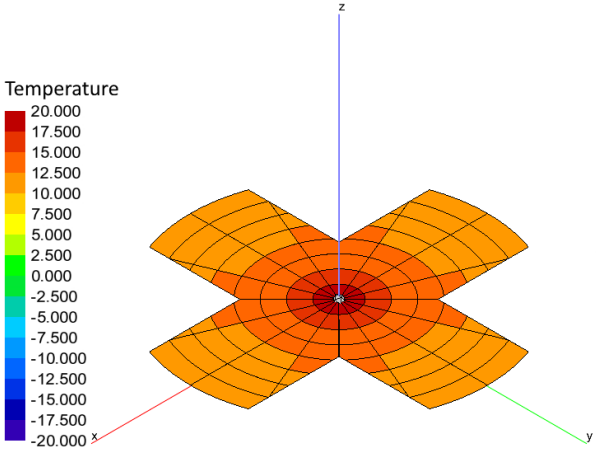

Figure 4.16: Disc with constant temperature in the centre with 4 square cut-outs.

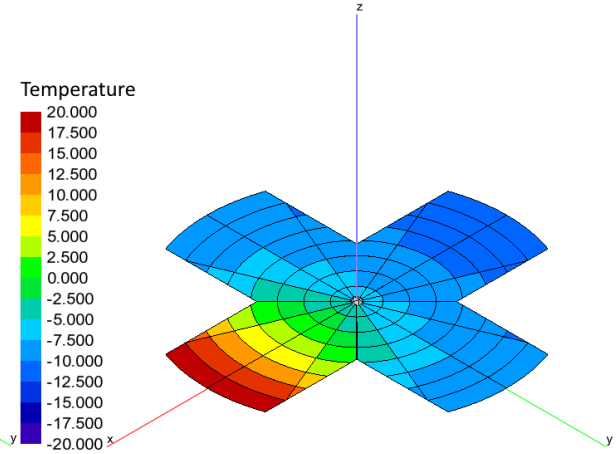

Figure 4.17: Disc with constant temperature at one of the sides with 4 square cut-outs.

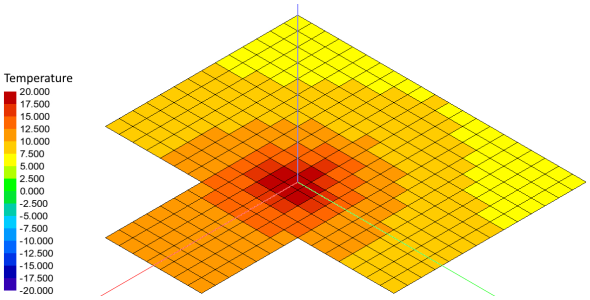

Figure 4.18: Rectangle with constant temperature in the centre with 2 square cut-outs.

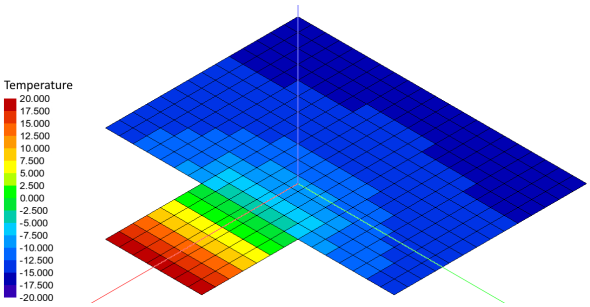

Figure 4.19: Rectangle with constant temperature at one of the sides with 2 square cut-outs.

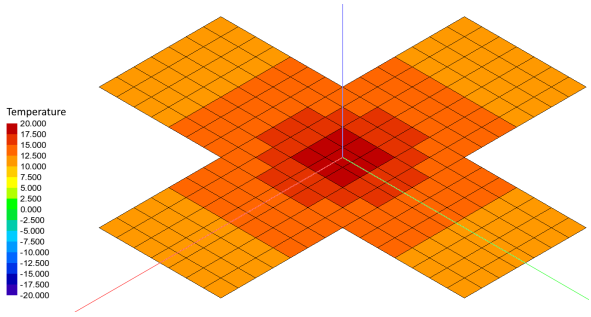

Figure 4.20: Rectangle with constant temperature in the centre with 4 square cut-outs.

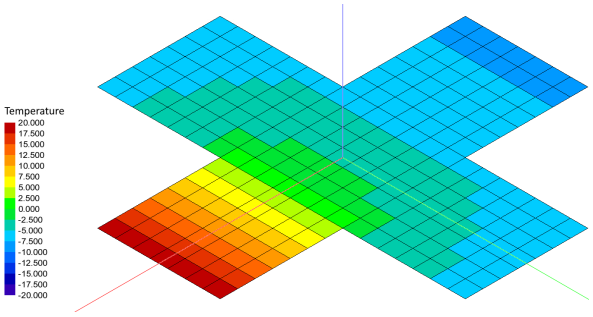

Figure 4.21: Rectangle with constant temperature at one of the sides with 4 square cut-outs.

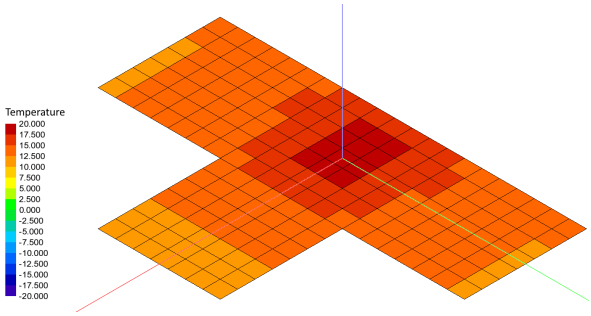

Figure 4.22: T-shape with constant temperature in the centre.

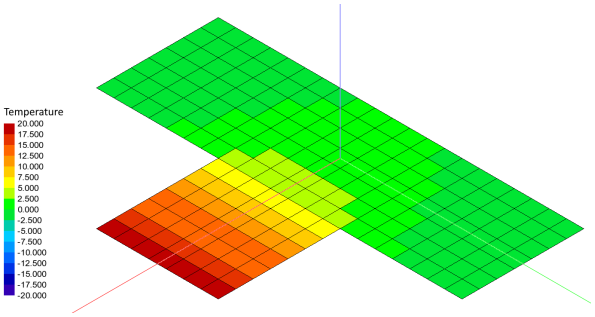

Figure 4.23: T-shape with constant temperature at the stem of the T-shape.

4.8. Heat interface

This section investigates the influence on the location of the interface on the heat transfer. This interface is the part of the radiator where the heat enters (requirement DRW-CSc1). Heat transfer is proportional to temperature, see Equation 4.1. A high temperature is desired over the full area of the radiator. As expected, having the heat source in the centre of the radiator, the radiator surface will result in a higher temperature, Figure 4.12, than having the heat source on the side, Figure 4.13. This is supported by the conductive heat transfer Equation 4.2. This equation shows that, with an increasing distance, the heat transfer is lower.

The location of the DRW depends on the available surface of the CubeSat. This thesis assumes in Section 8.3 that the top and bottom of the CubeSat are not available. This causes the DRW to be located on the sides. In this position, the location of the interface is preferred to be on one of the flaps.

The internal environment of the CubeSat is connected with a thermal link to the DRW via the heat interface. The interface can be a simple metal plate. On one side it is connected to the thermal link and on the other side it is glued to the laminate of the DRW.

$$Q_{conductive} = -\frac{kA}{L}(T_1 - T_2) \tag{4.2}$$

4.9. Scalability

Even though the proposed T-shape design can fit on a one standard unit (1U) CubeSat, the design is scalable. This means that the proposed design would also work for larger CubeSat sizes. Also, the shape can be made wider to use the whole width of 6U or larger CubeSats. The number of layers can be varied for different applications.

4.10. Implications of the design on the CubeSat system level design

The DRW has a low mass, but a large area. The result depends on the presence of other systems and instruments. This section will investigate the implications of the design of the CubeSat on system level.

4.10.1. Implication of folding

Folding the radiator over the outside of the CubeSat, covers the sides of and bottom. During storing, this is not a problem. If after deployment of the CubeSat from the launch vehicle, the radiator fails to deploy, these areas stay covered. This depends on the Hold Down and Release System (HDRS) or on the passive tape spring hinges. An alternative is to fold the radiator inside the CubeSat. This reduces the available volume on the inside of the CubeSat. However, on a failed deployment of the radiator, other systems are not covered.

When the radiator is folded over the outside of the CubeSat, it can be used as cover of the systems and instruments on the surface such as cameras. This could save mass and reduces failure modes of deploying the covers individually.

4.10.2. Implication of a large deployed surface

The DRW is a large surface that extends downwards from a side of the CubeSat. This means that it could interfere with other elements of the CubeSat. This should be prevented per requirement DRW-Dpl1-Ddc1. It is possible that the DRW casts a shadow over the solar arrays. To mitigate this, the solar arrays are installed at the top and the DRW is installed on the bottom, the Earth facing side. This minimises the chances of radiator to cast a shadow on the solar arrays. Other examples include the blocking the view angle of cameras installed at the bottom of the CubeSat and facing the Earth and the exhaust plume of engines.

4.11. Design summary

This chapter analysed the potential options for the design of the DRW. This section provides a summary of all design choices made.

The DRW is made of the material HiPeR. This material provides a high thermal conductivity with low mass and is flexible. This flexibility makes it possible to bend the DRW. To decrease the bending radius to fold the DRW for efficient stowing, the PG sheets in a small section of each flap are not adhered. This increase in flexibility, reduces the stiffness. Thus, a structure is required to provide additional stiffness, while also allowing for rotation to fold. A tape spring provides this structure and allows for local flexibility thus acting as a hinge. In addition, the tape spring also functions as an actuation system for the deployment of the DRW by storing potential energy when folding and releasing this energy when deploying.

In order to maximise the heat radiated while minimising the heat absorbed from the Sun, a thermo-optical surface finish with high emissivity and low absorbtivity is used. This includes most white paints.

The T-shape allows for foldability and provides the option to stow the DRW. This shape also provides an efficient heat spread over the surface of the DRW. Section 4.7 provide an answer for RQ-1. A shape with cut-outs have lower temperature gradients when the heat source is in the middle of the shape. When the heat source is at an edge of a disc, the temperature gradient is increases with more cut-outs. However, for square, plus and T-shaped radiators, the opposite effect is visible.

The interface of the DRW is located on the part which is connected to the CubeSat. A small metal plate connects the internal environment to the DRW.

In Section 4.7, the T-shape has three flaps and a centre. The DRW is attached to the CubeSat at the flap. This creates confusion with the name conventions. From here forward, the flap that is the interface to the CubeSat is called the base and the centre of the T-shape is the flap. This is detailed further in Figure 5.1.

5

Deployable Radiator Wing thermal performance analysis

The previous chapter provided the design for the DRW. This chapter will describe the thermal analysis model based on the design from Chapter 4 and provide the results of the numerical analysis of the DRW. This chapter starts with the assumptions to model the design of the DRW in Section 5.1. With the model assumptions, the model parameters are defined in Section 5.2. This model is analysed and the results are presented in Section 5.4 and the results are discussed in Section 5.5. The numerical analysis for the prototype from Chapter 7 is detailed in Section 5.6.

5.1. Model assumptions

This section summarises the design explained in Chapter 4 and makes assumptions to model this design in ESATAN-TMS-2019. The model is the T-shaped DRW. The HiPeR laminate is represented as a stack of geometries. A geometry for each of the three materials: PG, Kapton and the adhesive. This is explained in detail in Subsection 5.2.1. A heat load boundary condition is applied to the base part of the DRW, see Figure 5.1. The dimensions of the DRW are detailed further in Subsection 5.2.1.

From Section 4.7 the optimal shape to use is the T-shape. This allows for a large, foldable area which does not interfere with the deployment rails of the CubeSat.

It is unknown what the influence is on efficiency of the heat transfer between the PG sheets and the adhesive and the Kapton sheets and the adhesive. This requires additional research and testing. For this thesis I assume there is no thermal contact resistance between PG and Kapton sheets and the adhesive.

The PG adhered sheets are fully encapsulated by the top and bottom Kapton sheets. Thus the PG and adhesive sheets do not radiate to space.

To summarise, these assumptions are listed below:

- T-shaped DRW in free space.
- No thermal contact resistance between the PG and Kapton sheets and the adhesive.
- No radiative heat flow for the PG and adhesive sheets.

5.2. Model parameters

The model parameters describe the model physically in the numerical model. With the assumptions from Section 5.1, the model parameters can be estimated.

5.2.1. Deployable Radiator Wing

The DRW is modelled as the laminate. Each layer, either PG, Kapton or the adhesive, is modelled as a solid rectangle box. It consists of 12 layers of PG with a Kapton layer on the top and bottom and thus also 13 layers of adhesive. The properties of the geometric definitions are summarised in Table 9.1.

In order to simplify the explanation of the DRW, the surface distinguishes seven parts: four squares and three hinges, see Figure 5.1. These four squares are arranged in the shape of a fat letter T (inverted). These squares are connected with each other via a flexible part of the HiPeR laminate, the hinge, thus three hinges in total. The square on the vertical bar of the T is the base of the DRW. The horizontal bar is connected to the base with a middle hinge. The middle square of the horizontal bar is called the flap. The flap has on the right side and the left side a hinge with an square connected. On the left side of the DRW are the left hinge part and the left side part. On the right side are the right hinge part and right side part. The base, the flap, the left part and the right part of the DRW are squares with sides of 95 mm each. The hinge parts have the same width as a side of the square parts and a length of 10 mm.

The adhesive and PG sheets are radiatively inactive, except for the parts of the PG that are in the hinge parts. This means that the adhesive and PG sheets do not contribute in the radiative calculation performed by ESATAN-TMS-2019. This is to decrease the analysis run time and because these geometries do not radiate to any other surface or to space.

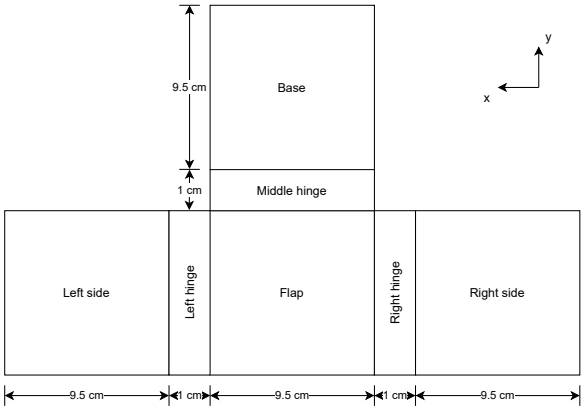

Figure 5.1: Schematic drawing of the DRW as seen from the $+z$-direction including the boundary heat load location.

5.2.2. Orientation and environment

The DRW is situated in empty space with a temperature of -270°C. This is the same as normal space because this analysis is performed without any external heat sources. Since there are no external heat sources, the orientation of the DRW, with respect to the surroundings, does not matter.

5.2.3. Boundary conditions

There is one heat load boundary condition on the base part of the DRW. The first option is a applied heat load to a strip of the base of the radiator near the flap, the second option is a heat load to a strip of the base of the radiator furthest away of the flap and the last option is a heat load to the full base. This option creates the largest temperature gradient over the base part and is, therefore, the least efficient option. For this analysis a quarter of the base part is chosen close to the flap, as shown in Figure 5.1. This allows for flexibility for the application of the DRW on a CubeSat. An average temperature of 20°C is desired. This amounts to an applied heat load of 20 W. The DRW radiates this heat to space with a boundary temperature of -270°C.

5.2.4. Nodes and grid patterns

There are only a few surfaces seeing each other. Therefore, this is not the governing factor on the node and grid patterns. The accuracy of the temperature gradient is much more important. The out-of-plane temperature difference is expected to be the largest at the base part, further to the flap and sides parts of the radiator the temperature gradient is expected to reduce to almost zero, because of the small thickness of the DRW. Each sheet of PG, adhesive and Kapton has one node in the out-of-plane direction. With the 27 layers the laminate consists of, this should be enough to model the out-of-plane temperature gradient. For in-plane temperature gradient, it is expected to have the largest temperature gradient at the base part, the middle hinge part and the first part of the flap part.

5.3. Deployable Radiator Wing sizing

The interface is located anywhere on the base part. To find what the implications are of the location of the interface, the DRW is simulated with the same temperature boundary condition applied at various locations on the base part.

The temperature gradient over the surface of the bottom and top of the DRW are presented in Figure 5.2 and Figure 5.3 for the interface location near the hinge, Figure 5.4 and Figure 5.5 for the interface location far from the hinge and Figure 5.6 and Figure 5.7 for the interface location near the hinge. The amount of heat dissipated for each interface location is presented in Table 5.1. The lowest temperatures are observed for the designs where the interface location is further away from the deployed part of the DRW. This is as expected because the heat load paths are longer and supported from the analysis from Section 4.7. In contrast, an interface close the hinge part is reduces the length of the heat load paths and is, therefore, more efficient. A large interface is more efficient because the average temperatures are higher and thus the dissipated heat is higher. Optimally, the interface should be large and close to the deployable part near the hinge part of the DRW. However, the place at the bottom of the CubeSat is potentially reserved for cameras or other instruments facing Earth. This reduces the possibility to utilise the optimal configuration. Therefore, further results are presented using the design with the interface far from the hinge part.

Interface location (input 30°C)	Dissipated heat [W]
Near the hinge	19.4
Far from hinge	17.0
Full base part	20.6

Table 5.1: Dissipated heat for the three locations for the interface

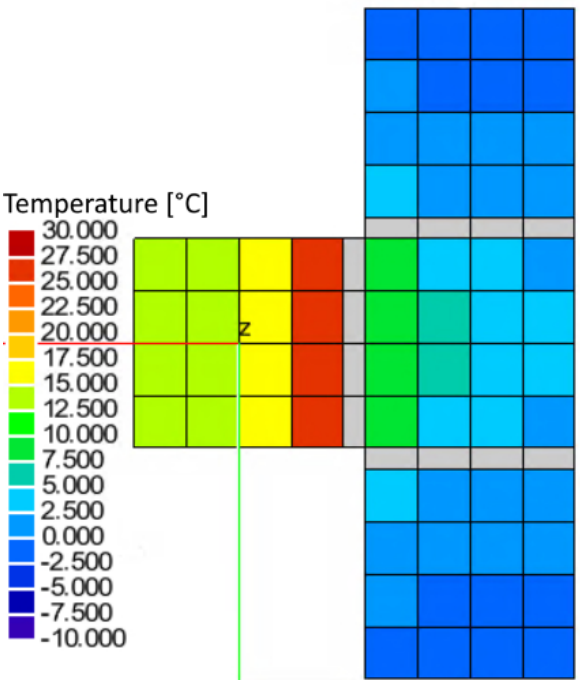

Figure 5.2: The temperature gradient on the back side of the DRW with a boundary temperature of 30°C near the hinge part.

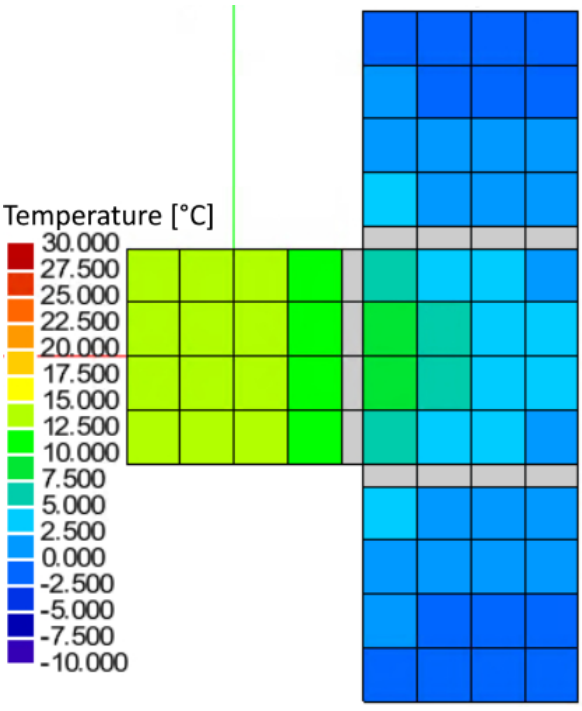

Figure 5.3: The temperature gradient on the front side of the DRW with a boundary temperature of 30°C near the hinge part.

To determine the optimal dimensions for DRW, the length of the base part, the length of the hinge and the number of layers are varied. The figures show the dissipated heat flow for a variation between the number of layers and the length of the base part. Figure 5.8, Figure 5.9 and Figure 5.10 vary the length of the hinge parts between 0.5 and 1.5 centimetres. Varying the length of the hinge parts does

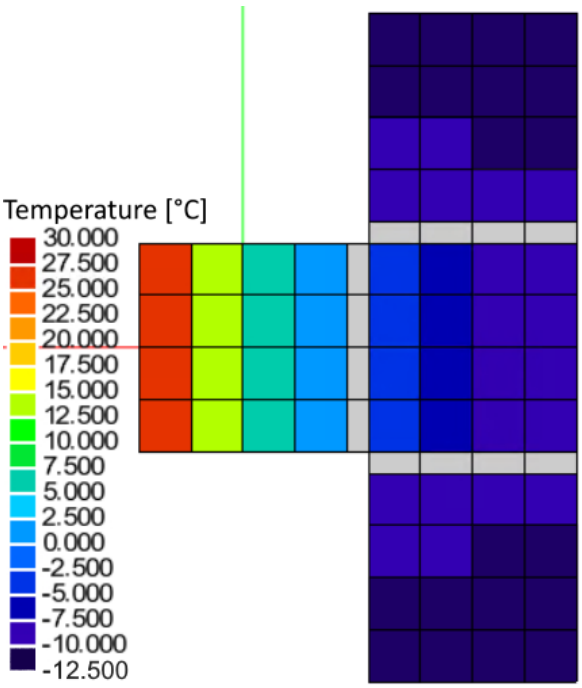

Figure 5.4: The temperature gradient on the back side of the DRW with a boundary temperature of 30°C far from the hinge part.

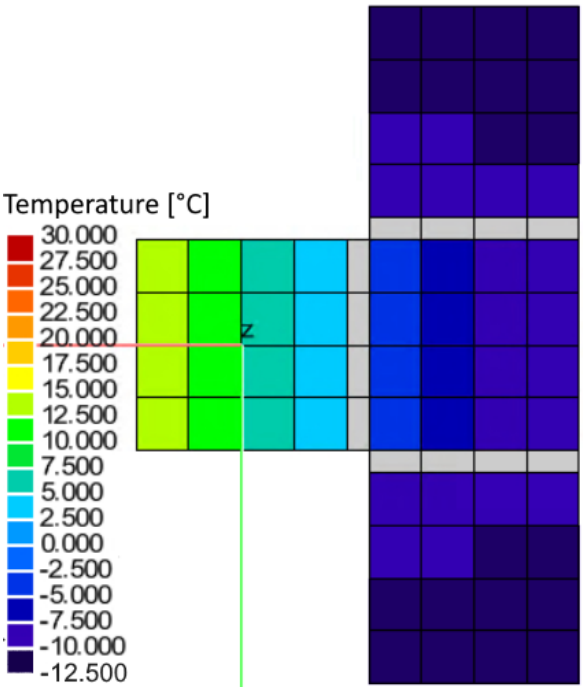

Figure 5.5: The temperature gradient on the front side of the DRW with a boundary temperature of 30°C far from the hinge part.

not change the performance of the DRW significantly. More than 18 layers does not provide more performance. Interestingly, an increase in the length of the base part improves the performance only significant for a higher number of layers and low length of the base part. This is because the the distance between the interface and deployed part is increasing as well, which reduces the thermal efficiently. This is compensated by the increase in total area and the larger interface as its length is defined as a quarter of the total length of the base part. The most significant factor is the number of layers up till 18 layers after which the gradient becomes vertical and the length of the base part becomes more dominant. The optimal number of layers is between 12 and 18. However, the difference in performance is only 1 W, therefore, 12 layers is sufficient. It is better to increase the length of the hinge part, but 0.1 m is sufficient for this design and increasing it at 12 layers does not increase the performance significantly.

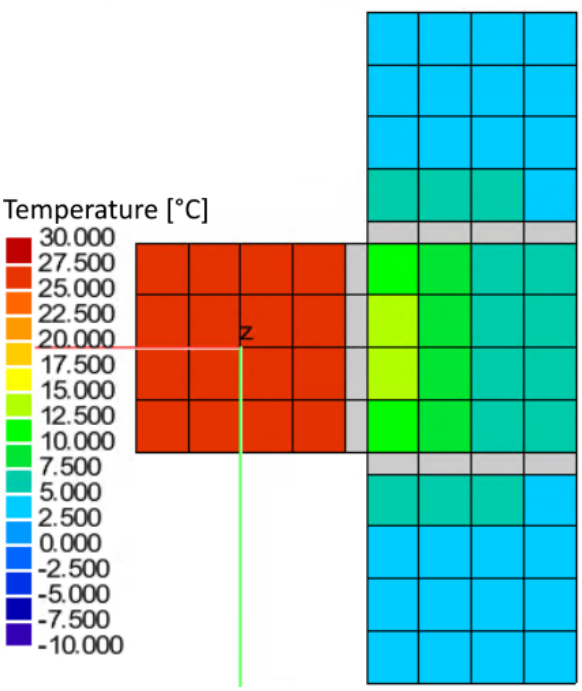

Figure 5.6: The temperature gradient on the back side of the DRW with a boundary temperature of 30°C on the full base part.

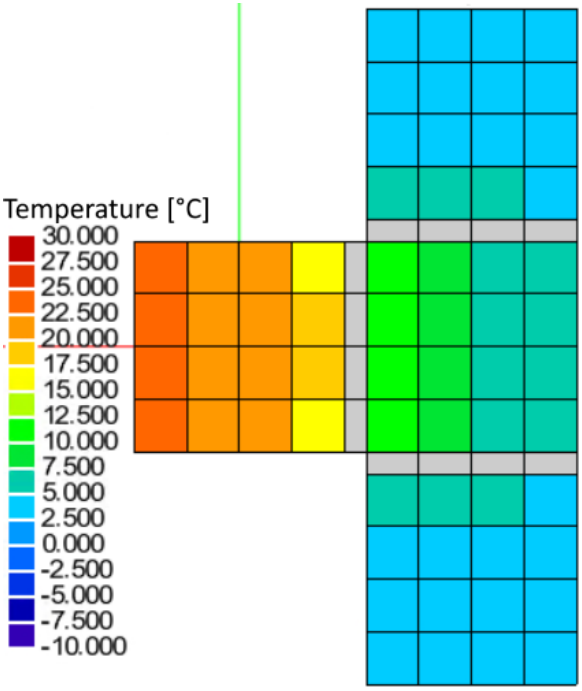

Figure 5.7: The temperature gradient on the front side of the DRW with a boundary temperature of 30°C on the full base part.

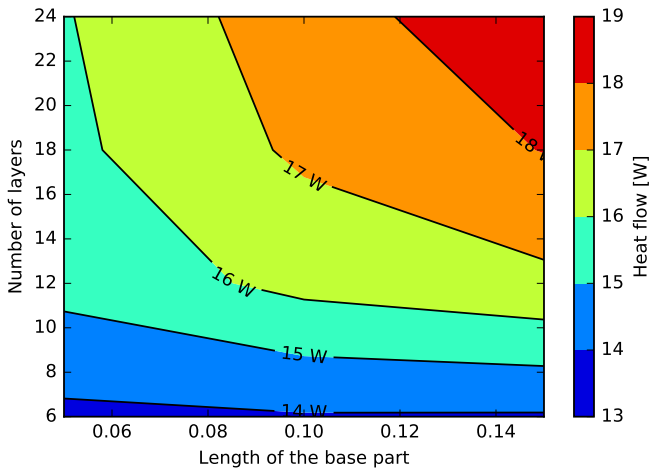

Figure 5.8: The temperature gradient on the back side of the DRW with a boundary temperature of 30°C on the full base part.

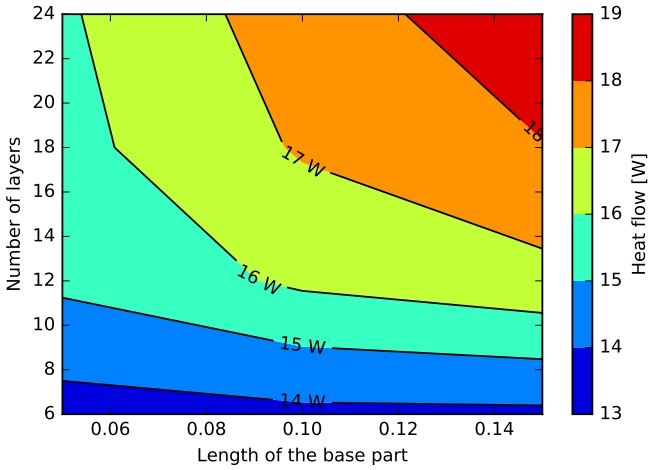

Figure 5.9: The temperature gradient on the front side of the DRW with a boundary temperature of 30°C on the full base part.

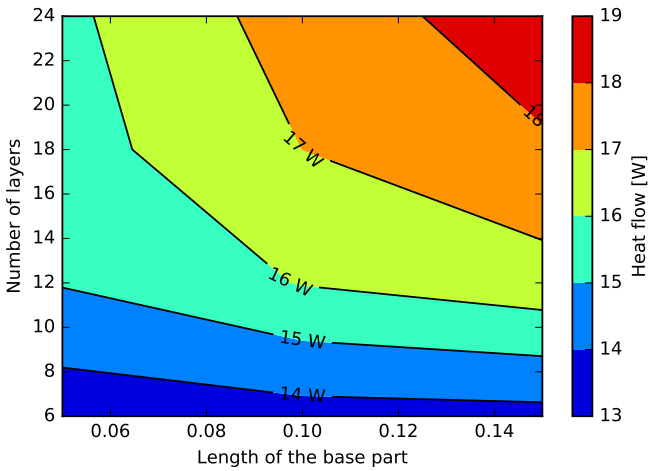

Figure 5.10: The temperature gradient on the front side of the DRW with a boundary temperature of 30°C on the full base part.

5.4. Numerical model results

This section present the results for the analysis of the DRW with the boundary conditions defined in Subsection 5.2.3. The model is with the thermal modelling software ESATAN-TMS-2019. This is further detailed in Appendix D

The temperature gradients are presented in Figure 5.11 for the back side and Figure 5.12 for the front side. These figures show clearly the temperatures and the gradients over the bottom and top surfaces. The grey areas are the hinge parts. These are grey because the temperature is lower than the minimum temperature presented in the legend. These parts are around -70°C. For some relevant locations on the top and bottom side of the DRW, the temperatures of the nodes are given in Table 5.2. Section 5.5 discusses the results presented here.

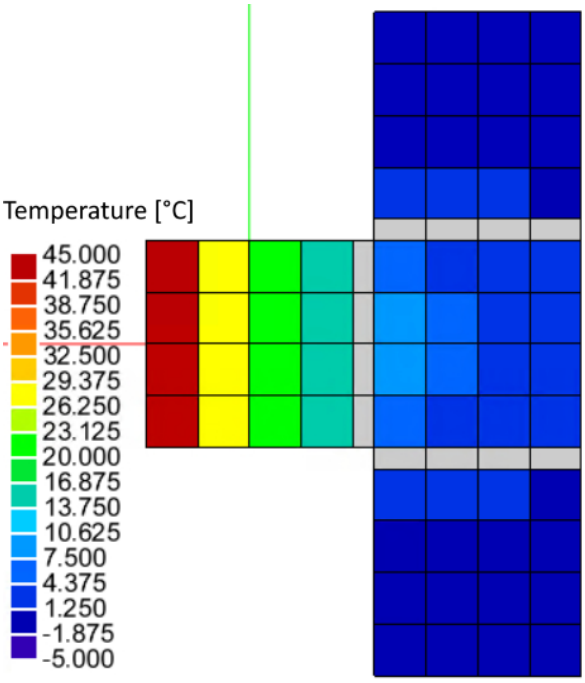

Figure 5.11: The temperature gradient on the back side of the DRW with a heat load of 20 W.

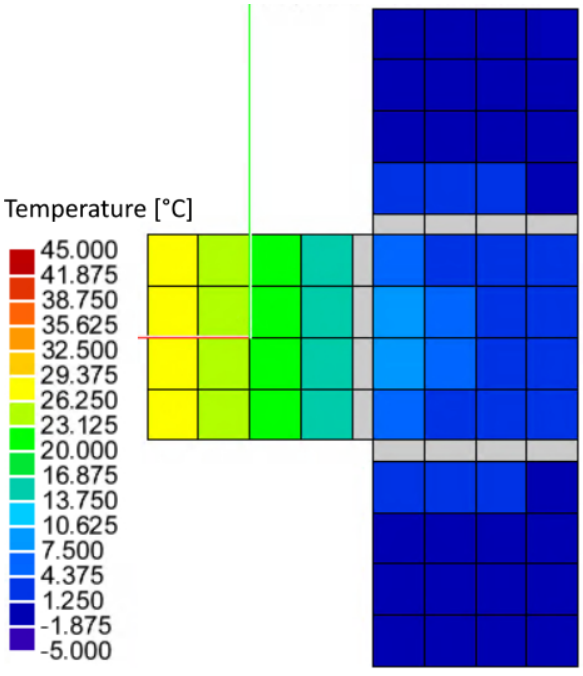

Figure 5.12: The temperature gradient on the front side of the DRW with a heat load of 20 W.

Table 5.2: Temperature results for the DRW to space of -270°C and with a 20 W boundary conditions.

part		Location	Node number	Temperature [°C]
Bottom	Base	Near heat input	10027	43.32
		Near hinge	10024	14.9
	Flap	Middle close to base	10219	8.14
		Middle close to side	10221	2.732
	Side (right)	Corner near hinge	10147	2.567
		Furthest point	10156	-0.8917
Top	Base	Near heat input	17557	29.07
		Near hinge	17554	15.39
	Flap	Middle close to base	17749	8.193
		Middle close to side	17751	2.732
	Side (right)	Corner near hinge	17677	2.576
		Furthest point	17686	-0.8922

5.5. Discussion of the results

This section tries to answer RQ-2 by analysing the temperature gradients of the DRW.

From Table 5.2, Figure 5.11 and Figure 5.12 it is observed that the temperature gradient is largest in the base part for the in-plane and the out-of-plane directions. The left and right side parts the temperature gradient is very small in both directions. The flap part has only a temperature gradient in the in-plane direction. This means that the heat is spread evenly after the base part. The high in-plane thermal conductivity makes up for the low out-of-plane conductivity of the PG and adhesive by spreading the heat in-plane first and later spreading the heat out-of-plane. It is observed that the back side of the DRW is not always warmer than the front side. In some places, layer 9 is actually the warmest of the nodes.

The grey nodes in Figure 5.11 and Figure 5.12 are -70°C. However, this is only the case for the Kapton sheets. The PG sheets below it, do have the temperatures similar to the nodes next to it. This results from the assumption that PG in the hinge parts does not radiate to the covering Kapton sheet. And since there is no adhesive between the PG sheets and between the Kapton and PG, there is no out-of-plane heat transfer. The low conductivity of Kapton and the thin sheets, result in low in-plane heat transfer, which results in low temperatures.

It is observed that the layers do not have a uniform temperature distribution. This is especially the case for the base part. The flap and side parts are more uniform. The temperatures for various locations on the top and bottom surface is presented in Table 5.2.

In conclusion the DRW is able to radiate 20 W with a maximum temperature of 45°C to just space. However, this does not take into account the heat absorbed from Earth and the Sun nor the interaction with a whole CubeSat. This will induce heat loads on the surface of the radiator and causes the thermal performance to reduce. This effect is investigated in more detail in Chapter 9.

5.6. Numerical model of the prototype used for testing

The numerical model described above, is changed for the test of the prototype. These changes are necessary because of the test location. For this thesis, the prototype test would take place in a vacuum chamber at Airbus Defence and Space Netherlands. But because of the COVID-19 pandemic, this facility was not accessible and an alternative test has been performed. For this alternate test, the model had to be adjusted because the alternate test facility cannot achieve sufficient vacuum. The model is adjusted for the alternative test environment: surrounding conditions, heat input, size, orientation and extra conductive heat flow definitions to take the influence of the air into account. This numerical model for the prototype test is modelled as the prototype defined in Chapter 7.

5.6.1. Numerical model changes

This subsection explains the differences between the analysis model and the model that will be used for the verification by test. The shape of the DRW is the same as presented in Figure 5.1. Only the dimensions differ and a cube is attached on the back side of the base part for mounting and performing other tests. The square parts are each 92 mm on each side and the hinge part is 8 mm long. The aluminium cube has side of 100 mm. The emissivity is 0.83 for the HiPeR laminate with a transparent Kapton top sheet with a grey PG sheet behind it. The emissivity of the aluminium cube and the walls of the vacuum oven are assumed to be 0.15.

The verification by test is performed in a low vacuum. This low vacuum still has some air molecules. These molecules allow for some heat conduction. Therefore, the verification by test is not purely radiation. The model must take this factor into account. In order to calculate the conductivity via the air a tool provided by Airbus Defence and Space Netherlands is used. This tool depends on the temperature of the DRW and the surrounding walls, the distance between the DRW and the surrounding walls and the pressure of the chamber. These expected values are summarised in Table 5.3. This results in thermal conductivity of 0.02616 W/mK. This thermal conductivity is modelled from all surfaces to a boundary node, which represents the air. This boundary node is constant at 28°C. The walls of the vacuum oven are represented by shell geometries which only radiate on the inside. These walls have a constant boundary condition of 27°C. Boundary conditions for the walls and the air are taken from the results from the test in Chapter 7. These parameter did not change much over the course of the test and are, therefore, considered constant.

The surroundings conditions are the walls of the vacuum oven with a constant temperature. The

Table 5.3: The parameters needed to calculate the thermal conductivity for an enclosed surface to the air.

Name	Value	Unit
Wall temperature	27	°C
DRW temperature	40	°C
Chamber pressure	120	$mBar$
Wall separation	0.2	m
Thermal conductivity of air	0.02616	W/mK

Table 5.4: The temperature boundary conditions for the walls and air and the heat load boundary conditions for the three test.

Boundary location	Value
Walls	27 °C
Air	28 °C
Power test 1	5.1 W
Power test 2	8.0 W
Power test 3	11.5 W

heat input will be the same as used in the verification by test from Chapter 11. For clarity the these conditions are listed again in Table 5.4.

5.6.2. Numerical model results of the prototype used in testing

The results for the numerical model of the prototype will be discussed along with the results of the thermal performance test of the prototype in Subsection 7.2.2.

5.7. Deployable Radiator Wing analysis summary

This chapter explains the model of the DRW to analyse for the thermal performance and presents the results. The DRW is modelled as a laminate of PG, adhesive and protective Kapton sheets. The thermal performance is analysed for in deep space with a boundary condition of -270°C. At the base part of the DRW, a heat load of 20 W is applied. This heat load represents the heat generated in the internal environment of the CubeSat. With ESATAN-TMS-2019 the temperatures and heat flows are calculated for the steady state solution. With these boundary conditions, the interface temperature is 43°C and the minimum temperature is -1°C. The in-plane and out-of-plane temperature gradients are the largest in the base part. The in-plane temperature gradient reduces for the flap and two side. The out-of-plane temperature gradient is almost negligible in the flap and two side parts. This answers RQ-2.

The test with the prototype is compared to a numerical model. This model is modelled to the test conditions and includes a simplified representation of the air and the walls of the vacuum oven. The results of this analysis are presented in Chapter 7.

Chapter 6 verifies the model presented in this chapter in a simplified way.

6

Model verification of the Deployable Radiator Wing

The large numerical model from Chapter 5 has many nodes and variables. This could lead to errors. Therefore, this model is verified in this chapter. A boundary mistake where the radiative calculations for the view factors are wrong is discussed. A solution is proposed in Section 6.1. The numerical model of the DRW is verified in Section 6.2.

6.1. View factor verification

For any surface all view factors to all other surfaces and space, should add up to 1. However, this was not the case for the Kapton surfaces of the DRW. Most surfaces of the DRW integrated on the CubeSat see only space. Some are perpendicular to other surfaces. This is the case for the bottom of the CubeSat and the DRW and the sides of the CubeSat and the solar arrays, see Figure C.1. The result is a view factor between the surfaces of the CubeSat and DRW to space close to 1. This is shown as orange in Figure 6.1. From Figure 6.1 the blue DRW is remarkable. It is expected that the view factor is more orange, just like the side of the CubeSat just above the DRW. This is also supported by the theory from the view factor equations from Appendix B. Further analysis showed that when the thickness of the solid elements is smaller than 0.1 mm, the view factors are not calculated correctly by the ray-tracing of ESATAN-TMS-2019. This explains the blue DRW in Figure 6.1. Since the radiantly active Kapton sheets are only 0.05 mm, the view factors are not calculated correctly. So for all the analyses in this thesis, the thickness of the Kapton sheets is doubled. It is expected that this does not have any influence on the performance. This is because the sheets are still very thin and have a low thermal conductivity and the influence on the in-plane heat transfer is, therefore, negligible compared to the high conductive PG sheets. However, due to the increased thickness, the heat flow out-of-plane it decreased. This could result in lower surface temperature and, therefore, lower heat flows to space. However, since the thickness of the Kapton sheets are still small, this is considered negligible.

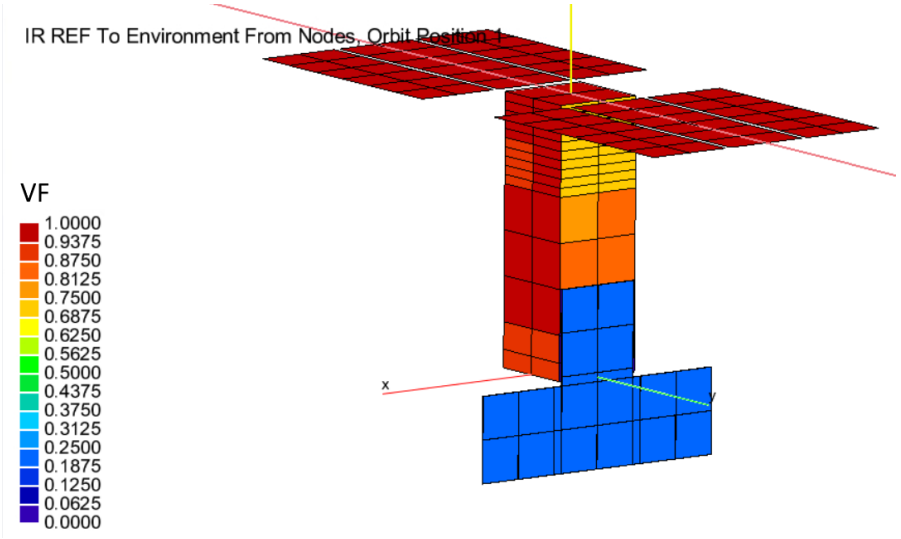

Figure 6.1: Whole satellite model with the wrong view factors.

6.2. Model verification by model nodes reduction

The model as defined in Chapter 5 is verified with a reduced model. The model is reduced to a few nodes to represent the DRW and its surroundings. Then equations for each of the conductive links between the nodes are set up. This system of equations is too hard to solve analytically, so a thermal modelling software is used. Since ESATAN-TMS-2019 is already used for the main model, this reduced model is solved by ThermXL. ThermXL is software, an Excel extension, that calculates the temperatures of a nodal network.

The base part of the detailed model has a large temperature gradient between the top and bottom (14.3°C). At the flap part, this gradient quickly reduces to below 1°C and at the side parts this reduces below 0.1°C. The large temperature gradient at the base part requires more nodes to simulate it than the other parts. The DRW has 12 layers of PG with adhesive in between each layer. Some of the layers are grouped into one node for the base part but for the other parts, all layers are grouped into one node.

The model consists of three nodes for the base part, each node represents four layers, and three nodes for the flap and two side parts, one node each comprising of all the layers in that respective part. Including the space node the model has a total of seven nodes, as shown in a schematic overview in Figure 6.3. Out of the six nodes of the DRW, four see just space, the other two are not radiantly active.Therefore, the view factor for the four nodes to space is 1. ThermXL solves this model for the steady state solution with the same boundary conditions as the detailed model: space at -270°C and a internal heat load of 20 W.

Table 6.1 presents the results of the reduced and detailed numerical models. The temperature differences at the interface and the base part are 5 to 10°C. The difference at the flap and the side parts is 5°C. The temperature gradient is for the reduced and detailed model very similar. This is shown in Figure 6.2. The higher temperatures for the reduced model is probably caused by the fact that the heat load in the detailed model is applied at the start of the base whereas for the reduced model the heat load is applied at the whole base part. This causes the temperature of the detailed model to be locally high (45°C), see the red parts in Figure 5.11. This drops to 15°C near the flap part. Thus, the average is 30°C.

In conclusion, the verification is accepted. The detailed and reduced model have similar gradients. However, due to the in-plane nodalisation of just one node per part, the temperature is averaged out over the node. This average flows down and thus causes the temperature of the other parts to be higher too.

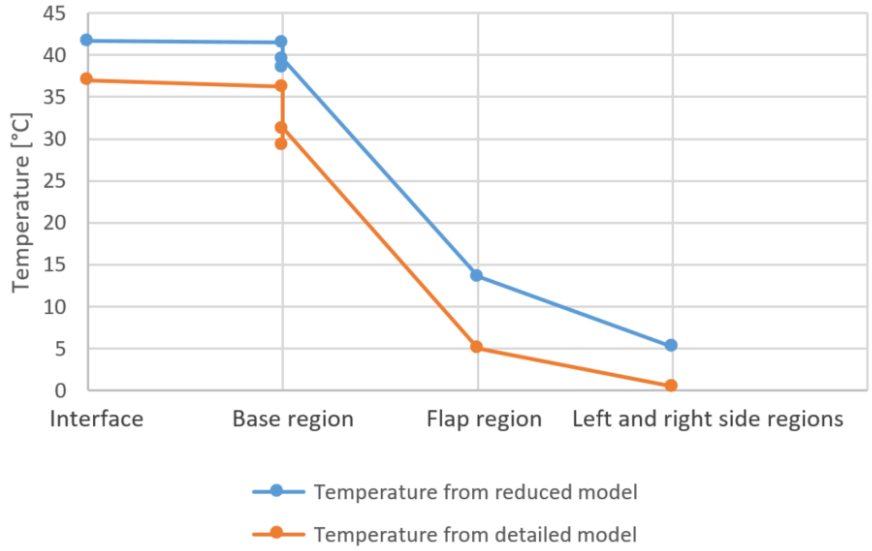

Figure 6.2: The temperature gradient for the reduced and detailed models for the parts of the DRW.

Table 6.1: The temperature results for the verification of the DRW for the reduced and detailed model from Chapter 5.

Element	Boundary condition: Internal power [W]	Temperature from reduced model [°C]	Temperature from detailed model [°C]
Base bottom		41.46	36.2
Base middle		39.61	31.3
Base top		38.44	29.3
Flap		13.61	5
Left		5.22	0.5
Right		5.22	0.5
Interface	20	41.66	37
Space (boundary condition)		-270	-270

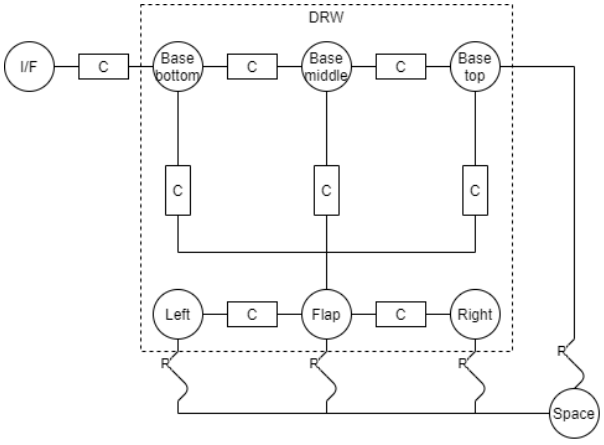

Figure 6.3: Schematic of the nodal network for the DRW with interface and space.

6.3. Verification summary

During the verification, it was found that ESATAN-TMS-2019 does not calculate the view factors correctly for solid type of geometries when the thickness is less than 0.1 mm. The PG, adhesive and Kapton sheet are all less than 0.1 mm. This caused ESATAN-TMS-2019 to underestimate the heat flow from the DRW. To circumvent this issue, the thickness of the Kapton sheet is increased to 0.1 mm. There was no solution found that would solve this issue without increasing the thickness of the material other than changing the model to shell elements which has its limitations. The PG and adhesive sheets are not increased in thickness because they are not used in the radiative calculation, thus there are no view factors calculated for those geometries. In addition, increasing the thickness would alter the performance significantly and thus the model would not resemble the design. The influence on the performance of the Kapton sheets are not significant because the thermal conductivity is not high and does not provide a significant contribution to the in-plane heat flows. The increased thickness, reduces the out-of-plane heat flows, but since the thickness is still small, this is considered negligible.

To prove that the detailed model from Chapter 5 is suitable for analysing the thermal performance of the DRW, a reduced model it created using different thermal modelling software ThermXL. This found that the overall temperature of the reduced model is higher Figure 6.2.

7

Prototype testing

Chapter 4 explained the design of the DRW. This design was used in the numerical models to determine the thermal performance in Chapter 5 and Chapter 9. This chapter shows the application of the DRW with a prototype. Section 7.1 provides the design of the prototype. With this prototype, tests can be performed to verify the performance predicted by the theory and numerical models.

Not all the planned tests could be performed because of the complications by the COVID-19 pandemic. Because of these complications, the prototype could not be tested in the vacuum chamber at Airbus Defence and Space Netherlands as intended. Alternatively, the prototype was tested in a vacuum oven at the Delft University of Technology, with measurement equipment from Delft Aerospace Rocket Engineering. The plan for the test of the prototype in the vacuum chamber and vacuum oven is described in Section A.1. The results of the test in the vacuum oven are described in Section 7.2.

7.1. Design of the prototype

The prototype specifically built for this thesis project, consists of two elements: the radiator and the support structure. The radiator is made from a laminate of PG, adhesive and Kapton sheets as described in Section 4.2. The support structure is a dummy CubeSat made from aluminium. It is an aluminium cube with one side open. On one of the sides the DRW is adhered. This dummy is used as support structure and to fold the DRW around. To simulate the heat generated by the instruments of the CubeSat, the prototype for the thermal performance test has a heater. The heater is located on the inside of the aluminium dummy CubeSat at the opposite side of the wall where the radiator is adhered to.

At the request of Airbus Defence and Space Netherlands, the production of the laminate of the DRW cannot be shared in this thesis. The final prototype of the laminate of the DRW is presented in Figure 7.1.

The aluminium support structure is made from 2 mm aluminium plates. Two L-shaped plates are adhered perpendicular. Two smaller plates allow a gap for the tape spring to fit. This results in a cube with edges of approximately 10 cm each. It has one side open. One face has a gap in the middle where the supporting tape spring can fit in. The final product can be seen in Appendix E.

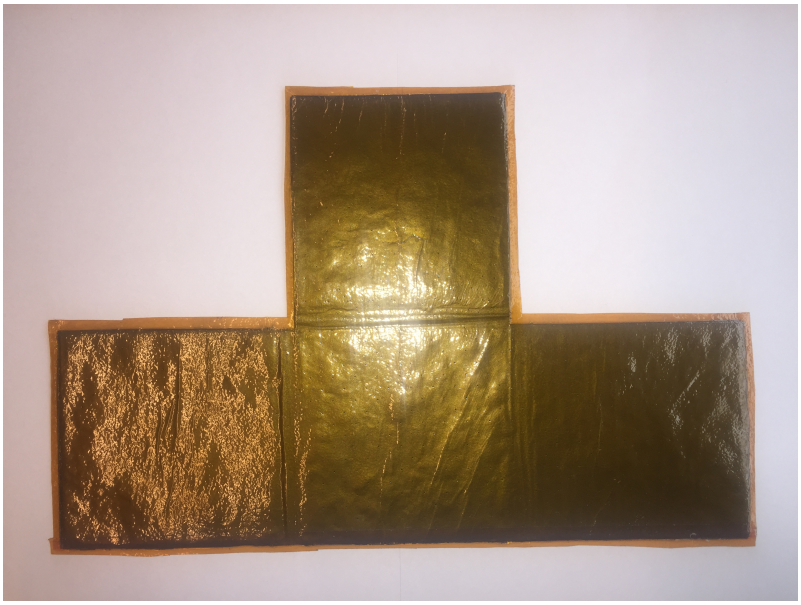

Figure 7.1: Final product of the DRW

7.2. Thermal performance of the prototype

The numerical analysis performed in Chapter 9 requires verification by testing. This means that a prototype of the DRW will be put in similar conditions to those in the analysis. However, not all conditions can be replicated artificially, most notably the assumed orbit. In order to replicate the orbit, the DRW must be placed in a vacuum chamber that simulates the incoming Solar, albedo and Earth IR radiation which also changes over the orbit. In addition, the cold temperature of the space environment should be simulated. The replication of the orbit is not deemed achievable for this thesis project due to budget and equipment constraints. Only the vacuum conditions could be simulated in a vacuum chamber. The prototype test was supposed to be performed in the vacuum chamber from Airbus Defence and Space Netherlands, however, due to the consequences of COVID-19 this was not possible. As an alternative, the vacuum oven from the Delft University of Technology is used, with measurement equipment from Delft Aerospace Rocket Engineering. The result of this is that the desired vacuum of less than 0.001 Pa, as advised by Airbus Defence and Space for testing where radiative heat transfer is dominant, could not be achieved. Instead, the achieved pressure was 12,000 Pa.

Testing the DRW can be represented as just the DRW. An aluminium dummy cube is used as mounting and to fold the radiator around it. Unfortunately, the prototype will not resemble much of the model defined in Section 9.4. Therefore, a new model was defined in Section 5.6 that is representable for the test set-up including the appropriate surrounding boundaries.

7.2.1. Prototype test description

The prototype is placed in the middle of the vacuum oven on an elevation. Thermocouples are placed on the Kapton sheets with aluminium tape to allow for good conduction to the thermocouples. A thermocouple is placed in the middle of each of the four parts on the top and bottom side. The bottom side of the base part is adhered to the aluminium cube and is, therefore, placed on the cover plate of the heating element. Additional thermocouples are place on the top and bottom wall of the vacuum oven and one free hanging to measure the air temperature.

7.2.2. Test results

This section presents the data from the prototype test and the prototype model from Section 5.6 so a comparison can be made. The discussion is explained in Subsection 7.2.3.

The temperatures are continuously measured during the test. The comparison can only be performed for the steady state situations. Therefore, this analysis is performed with the temperatures when the temperature change is less than 0.05°C per minute, thus assuming that the steady state

situation is sufficiently reached. These temperature results are presented in Figure 7.2 along with the results obtained from the numerical analysis of the prototype model which is described in Section 5.6. This figure shows the temperatures measured at the different parts of the DRW for the top and bottom. The nodal network diagrams of the numerical analysis for the three boundary conditions of 5.1, 8.0 and 11.5 W are presented in Figure 7.3,Figure 7.4 and Figure 7.5 respectively.

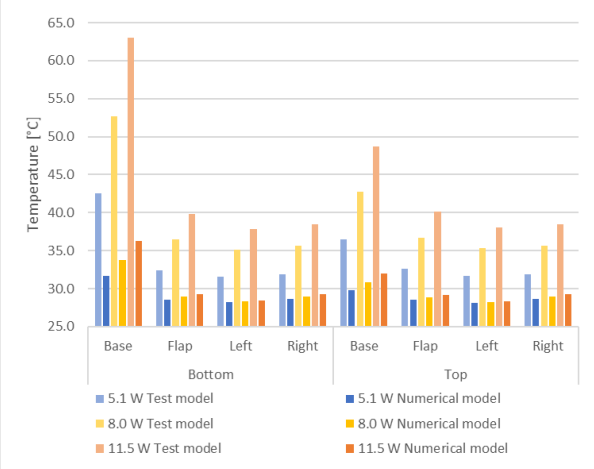

Figure 7.2: The steady state results for the prototype test and numerical model of the prototype test.

7.2.3. Discussion of the test results

There are various observations obtained regarding the results presented in Subsection 7.2.2. In this section, first, the observations of the test are discussed. Second, the observations for the test are combined with the observations for the numerical model adjusted for the prototype test as discussed in Section 5.6.

The temperatures measured during the tests show what is expected on basis of the thermodynamic principles [3]. Increasing the heat load boundary condition, causes the heat flows in the DRW and from the DRW to the surroundings to increase. To accommodate for this increase in heat flows, the temperatures should increases following from Equation 4.2 and Equation 4.1. The difference between the temperatures of the top and bottom of the flap, of the left part and of the right part are small. This is supported from previous analyses of the detailed models in Chapter 5 and Chapter 9. The interface between the heating element and the base part of the DRW has the highest temperature. This temperature gradient decreases in the out-of-plane direction over the thickness of the radiator and the in-plane direction toward the flap part. This behaviour is also observed in the analyses of the detailed models in Chapter 5 and Chapter 9.

Comparing the prototype test results with the results from the numerical model adjusted for the prototype test as described in Section 5.6, a large difference becomes apparent. The temperatures of the DRW are significantly lower for the numerical model for the prototype test than for the prototype test itself. This discrepancy is further illustrated by Figure 7.3, Figure 7.4 and Figure 7.5. These figures show the nodal network of the numerical model for the prototype test as defined in Section 5.6 with the heat flows from the DRW and the dummy CubeSat to the air and the walls of the vacuum oven. The interface contains the heater. This heater provides a heat load into the system. Most of this heat is conducted to the DRW and the aluminium dummy cube. Instead that this is radiated to the walls, it is conducted to the air instead.

As an alternative to the model in ESATAN-TMS-2019, the heat flow and temperature calculations are performed analytically. The nodal network from Figure 10.1 is used. This can be used to estimate the conductivity of the material and test whether this complies with the theory. The flow of heat through the various parts of the DRW is shown in Figure 7.6. The heat flows from the input on the left through the PG sheets and is radiated to the walls of the vacuum oven or conducted to the air. The test provides the surface temperatures. This allows for calculating the radiative heat flows from the DRW to the walls of the vacuum oven. However, the heat flow from the DRW to the air is significant, as explained before.

Calculating this is more difficult because the air properties are dependent on the temperature and the thermal conductivity via air is dependent on many factors such as temperature, pressure, geometry, distance to other surfaces and air flow [34]. The heat flow between each square is the sum of the the heat entering the square minus the sum of the heat leaving the square. For calculating this, the only unknown values are the heat flows to the air. However, the heat flow via the air can be estimated by introducing constraints to the values. The constraint is that the heat flow from each of the squares of the DRW is similar. The temperatures do not differ much and the surface area is equal. Only the heat flow to the air from the heater will be different. For simplicity, all heat flows to the air are assumed to be equal. The total heat flow to the air is the heat applied by the heater minus the radiative heat transfer. This results in an estimation for the heat flow to the air inside the vacuum oven. The total heat flow to the air is for each of the three tests around 52% of the incoming heat. Finally, the thermal conductivity between the squares can be calculated. The thermal conductivity between the base and the flap is almost 0.6 W/K and between the flap and the left and right side is 0.8 W/K for all three cases. The theoretical value for the thermal conductivity between two squares of the DRW is 0.6 W/K for 12 sheets of PG at 1350 W/mK. The influence of the adhesive to the thermal conductivity is negligible. This means that the heat flow is higher than the theoretical value for the thermal conductivity between the flap and the left and right side parts. The difference between the estimated and theoretical values for the thermal conductivity has two causes. The first cause is that heat flow to the air is underestimated for the heater, base and flap parts. This causes the calculated heat flow to the flaps to be overestimated and thus the thermal conductivity is higher. Second, the corners of the left and right side parts are actually very close to the base part. This is not reflected in the assumed nodal network of Figure 10.1. This causes an overestimation of the heat flow between the base and the flap part and add heat flow path between the base and the left and right side parts of the DRW.

As explained in Section 5.6, the test environment was changed from a vacuum chamber into a vacuum oven, with different vacuum level. The desired vacuum for purely radiative thermal links is less than 0.001 Pa. This could only be achieved with a vacuum chamber. In the vacuum oven the achieved pressure was 12,000 Pa. Therefore, the model for testing was also adjusted to take the air into account. The conductivity of the heat flows to the surrounding air, as explained in Section 5.6, is probably in reality lower than in the model. This high conductivity causes the temperature to be lower as observed in Figure 7.2.

It is recommended to perform the test in a vacuum chamber or remodel the numerical model for the prototype test the heat flows to the surrounding air.

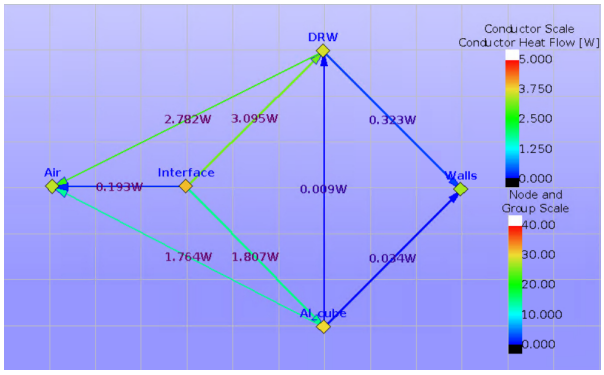

Figure 7.3: Numerical model of the prototype test in air with a 5.1 W heat input.

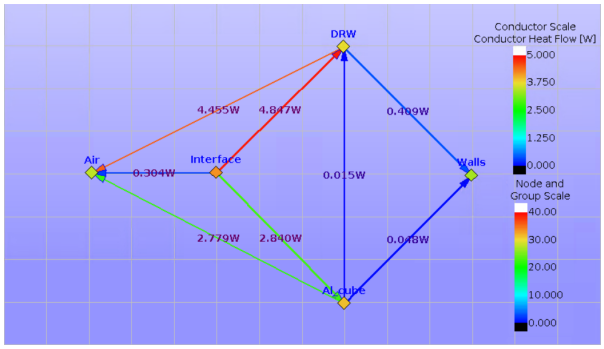

Figure 7.4: Numerical model of the prototype test in air with a 8.0 W heat input.

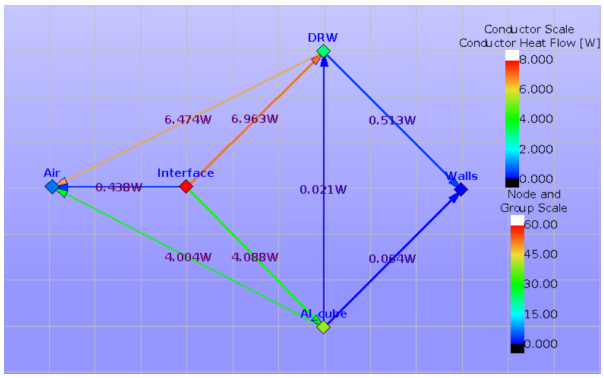

Figure 7.5: Numerical model of the prototype test in air with a 11.5 W heat input.

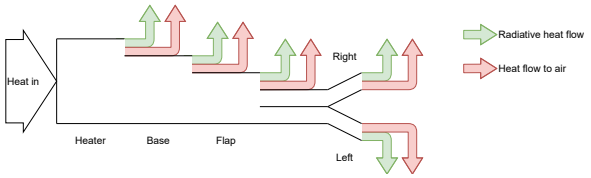

Figure 7.6: Heat flow throught the DRW to the air and via radiation.

7.3. Test summary

This chapter explained the design of the prototype and performed the thermal performance test for the DRW. Due to the COVID-19 pandemic, additional tests were not able to be performed and the thermal performance test was performed in a vacuum oven instead of a vacuum chamber. This required an adjustment of the numerical model to take the influence of the air into account during testing. This model probably overestimated the heat flows from the prototype to the air, thus producing lower temperatures than measured during the prototype test. The verification of the numerical model by testing is undetermined.

By calculating the radiative heat flows and estimating the conductive heat flows, it is possible to estimate the thermal conductivity. The thermal conductivity of the prototype is around 0.6 W/K. This matches the expected theoretical value for 12 sheets of PG.

8

Design of the Deployable Radiator Wing integrated on a CubeSat

Chapter 5 provided the results of the numerical analysis for the DRW and Chapter 6 provides the verification of this numerical analysis. This chapter provides an overview of the design of the satellite including the DRW. This design is based on the study case presented in Chapter 2. The analysis of this system is performed in Chapter 9 and the verification is performed in Chapter 10.

The design of the DRW integrated into a satellite system is comprised of the various system elements: the CubeSat with the internal instruments and the solar arrays. The CubeSat design is explained in Section 8.1 and the design of the solar arrays is explained in Section 8.2. In Section 8.3 is explained how the DRW is integrated into the full system.

8.1. CubeSat design

The DRW, explained in Chapter 4, is attached to the CubeSat. This CubeSat is modelled to an expected but simplified example. The CubeSat is three standard units. Each of these units have a system that produces heat. These three heat producing units are a stack of PCBs and two dummy payloads. All three are modelled as a surface for simplicity, more about this in Section 9.1. The stack of ten PCBs are placed at the top near the solar arrays and the two dummy payloads are located at the bottom and below halfway the CubeSat body as can be seen in Figure 8.1.

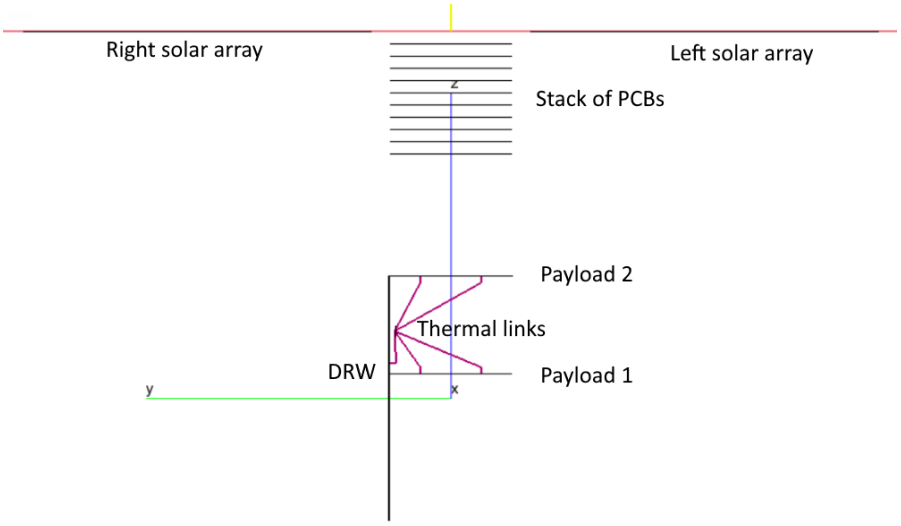

Figure 8.1: The inside elements of of the CubeSat model viewed from the $-x$-direction.

8.2. Solar array

The solar arrays are located at the top. As discussed in the study case in Section 2.1, the solar arrays will be Sun pointing for a higher power generation and that the orbit is polar. Thus, the solar arrays rotate with respect to the CubeSat such that it is kept perpendicular to the Sun. The solar arrays consist of a series of three panels on each side. This configuration is able to generate up to 42 W, which is enough for the amount of heat it generates. This is assuming six arrays of 6.9 W [14] each. The Sun rotates around the x-axis in the xz-plane. In order to generate more power, the rotating solar array should also rotate around the x-axis. The solar arrays are the horizontal lines on both side of the top of the CubeSat in Figure 8.1. The axis of rotation is the red horizontal line crossing the solar arrays. Perpendicular to that line is the Sun vector point upwards to the Sun.

As Earth revolves around the Sun, the orientation with respect to the Sun shifts. This is not taken into account, however, the effects from this are analysed in Subsection 9.5.3.

8.3. DRW integration

The solar arrays are at the top. This does not leave space for the deployable radiator especially with the rotating solar array mechanisms. For a satellite in Nadir orientation, the payloads probably require a view of Earth. This excludes the bottom of the satellite for the interface. From Section 4.3 follows that the radiator shall be kept from direct sunlight and that it is folded over the outside of the CubeSat. To prevent the radiator from direct sunlight, which reduces the performance of the radiator, the DRW should be perpendicular to the angle of rotation of the solar arrays, see Figure 8.1. From Section 4.7 follows that the DRW has a T-shape. The T-shaped DRW is integrated at the side of the bottom part of the CubeSat body. The DRW is seen as the blue T-shaped structure in Figure C.1 and C.8 with the Sun orbiting the xz-plane.

The connection between the interior of the CubeSat and the radiator can be any thermal link. Possibilities include thermal straps and heat pipes. This thesis does not investigate efficient methods for these thermal link, therefore, it is assumed that the conductivity is large.

Payloads in the bottom of the CubeSat are close to the radiator. A thermal link is between both payloads and the DRW for easy heat exchange. The thermal links are shown in Figure 8.1.

8.4. System design summary

The DRW is part of a larger system, the CubeSat. Before analysing the thermal performance of the DRW integrated in the CubeSat system in Chapter 9, the system must be defined. It is assumed that the system is a 3U CubeSat that is Nadir pointing. The CubeSat generates heat. To model that, it has two dummy payloads on the bottom side of the CubeSat for Earth view. At the top, there are 10

elements that simulate the PCBs.

The solar arrays generate the required energy. Since this is a CubeSat with a dedicated thermal control system, it is assumed that the energy generation system is advanced. Deployable, rotating and Sun pointing solar arrays are located on the top side of the CubeSat.

The DRW is integrated on the lower side of the CubeSat such that the plane of the radiator is perpendicular to the axis of rotation of the solar arrays to minimise direct illumination from the Sun. The heat-generating elements of the CubeSat are connected to the DRW with a thermal link.

Chapter 9 translates this design in a model and analyses the thermal performance of the whole system in an orbit around Earth.

9

System thermal performance analysis

This chapter analysis the thermal performance of the DRW based on the design of the DRW, explained in Chapter 4, integrated into a system, explained in Chapter 8. This chapter provides an answer to the Main research question: *"What is the effect of an external radiator using HiPeR to the temperature progression of a CubeSat over the course of a polar orbit?"*. This chapter starts with the explanation of the model assumptions in Section 9.1. With the list of assumptions stated, the model can be constructed using the model parameters in Section 9.2. To analyse the thermal performances and behaviour of the model, the workings of the tool, ESATAN-TMS-2019, is explained in Section 9.3. At this point, everything is defined and thus the model can be analysed. This analysis involves solving the nodal network, presenting the results and discussing these in Section 9.4. Many of the assumptions explained in Section 9.1 are made because parameterising these is difficult or even unknown. Section 9.5 analyses the influences of these assumptions on the thermal performance. Some of the assumptions from Section 9.1 are based on an educated guess. This guess is changed in Section 9.6 to other values to look at the influences on the thermal performance. For this thesis, a common model CubeSat is used.

9.1. Model assumptions

In order to model the radiator accurately predictions must be made on how the DRW will be used and what its properties are. The DRW is meant to be used on high-performance CubeSats. The size of a CubeSat ranges from small 1U to large 12U. This standard unit is a cube with sides of 10 cm each. It is expected that smaller unit CubeSats will not be needing a lot of heat dissipation. The minimum expected size would be a 3U CubeSat. This radiator is designed to be scalable, more about this in Section 4.9. Hence, the model assumes a 3U CubeSat as the baseline. It is assumed that the DRW is mounted on the bottom side of the CubeSat, so it will not interfere with the solar arrays on top.

In order to increase the power generation, deployable and even Sun-pointing solar arrays will be needed. Since the DRW is only needed when there is a high power generation, the model assumes a large deployable Sun-pointing solar panel. With rotating and Sun-pointing solar arrays, some form of Attitude Determination and Control System (ADCS) must be present. Thus, it is logical to conclude that the payloads also need some pointing requirements, such as permanent Nadir pointing. Therefore, it is assumed that the negative z-axis, the bottom of the CubeSat, points towards Earth at all times.

This generated electricity is almost all converted into heat. To model the heat generation on the inside, it is assumed that the CubeSat will have 1 unit of PCBs and two payloads (identical for the purpose of generating heat and its properties). During daytime the solar arrays collect a lot of energy. However, during eclipse there is no energy generation. Thus, spacecraft rely on batteries to cover the gap between the cycles of power generation. Batteries are quite voluminous and heavy. To limit the mass of these batteries, usually, the power consumption is decreased during eclipse. It is assumed that the heat generation is halved during the eclipse. There may be instances when (some of) the systems are operated at full capacity, however, if these occurrences only last a few minutes, the previous assumption still holds true.

The heat from the internal components must be led to the DRW for higher efficiency. For this model,

it is assumed that the internal conductivity is high. To achieve this high internal conductivity thermal straps made from PG or heat pipes could be used. Subsection 9.6.2 investigates the influence and sensitivity of varying this thermal conductivity. In addition to this, it is assumed that there is no thermal contact resistance between the PG and Kapton sheets to the adhesive. In addition, it is assumed that the interface is simple and does not have any thermal resistance.

For Earth observation satellites, the largest Earth coverage is achieved in a polar orbit, thus such an orbit is assumed. CubeSats are generally used in low orbits, so an orbit in LEO range is assumed. Over the course of the orbit of Earth around the Sun, the orientation of the CubeSat with respect to the Sun is held constant. This assumption is investigated in the sensitivity analysis in Subsection 9.5.3.

The DRW is a laminate of PG layers with adhesive in between. On the top and bottom of the radiator, Kapton sheets are adhered to protect the thin and fragile PG layers. The laminate consists of 12 layers of PG adhered with 3M966 adhesive. In Subsection 9.5.2 the sensitivity on the number of layers is analysed. The DRW is located parallel to the xz-plane as described in Section 8.3.

The heat dissipation and absorption are not only dependent on the temperature but also on the emissivity and absorptivity. These two thermo-optical properties have a high influence on the heat balance and, thus, the thermal performance. A CubeSat which requires a dedicated system to dissipate heat, also needs dedicated surface properties. Therefore, it is assumed that the surfaces of the CubeSat will have special surface finishes. All outside surfaces, the CubeSat, solar arrays and DRW, are coated with white paint. However, since the top side of the solar arrays is covered with solar cells, this cannot be painted. Therefore, these will use average values for solar cells. The inside surfaces of the CubeSat, the PCBs and the payloads are assumed to be black. This is typically done to improve the radiative capabilities inside the satellite [19].

For simplicity it is assumed that the body of the CubeSat and the solar arrays are made from aluminium and that the payloads and PCB stack are all made of the same medium conductive material. Furthermore, the payloads are assumed to be flat plates in the radiative calculations, however, the total heat capacity is still high.

To summarise, these assumptions are listed below:

- 3U CubeSat (scalable)
- DRW attached to the bottom
- Sun-pointing rotating solar arrays
- Nadir pointing negative z-axis
- Heat input: PCBs and two payloads
- Heat input halved during eclipse
- Internal conductivity is high
- No thermal contact resistance between the PG and adhesive layers
- No interface resistance
- Polar LEO
- DRW parallel to the solar rays
- Layered sheets of PG
- Protective Kapton layer
- Thermo-optical properties
- Materials

The assumptions described above are translated into (model) parameters in Section 9.2.

9.2. Model parameters

The model parameters describe the model physically. With the assumptions from the previous section, the model parameters can be estimated. This model parameters consists of the dimensions of the model which are described in Subsection 9.2.1, the properties of the materials and thermo-optical surfaces in Subsection 9.2.2 and the orbit and orientation with respect to the Sun and Earth in Subsection 9.2.3. Then the boundary conditions are defined in Subsection 9.2.4 and finally the grid pattern is explained in Subsection 9.2.5. This section expands and defines parameters for the assumptions presented in Section 9.1.

9.2.1. Geometric definitions

The geometries of the model can be divided into three groups. This subsection explains the parameters for each of the defined geometries. The first group is the CubeSat body and the payloads which is explained in Subsection 9.2.1. This is followed by the explanation of the geometric definition for the solar arrays in Subsection 9.2.1. Finally, the geometry of the T-shaped DRW are explained in Subsection 9.2.1.

CubeSat body and instruments

The body of the CubeSat consist of three standard unit CubeSat cubes stacked on top of each other, forming one rectangular shell box of 10 by 10 by 30 cm, has a 2 mm aluminium wall thickness and with dual thermo-optical properties for the inside and outside to model the different paints that could be applied. This holds the payloads and stack of PCBs on which the heat load boundary in placed on. The stack of PCBs consists of 10 PCB plates spaced at 1 cm and are modelled as a rectangular shell plate at the top unit of the CubeSat. The payloads are modelled in the same way as the PCBs. One is modelled half-way the first unit and the second payload is between the first and second unit.

Solar arrays

The large, Sun-pointing solar arrays for generating the required power are placed at the top unit of the CubeSat. They consist of a pair, one on each side of the CubeSat. Each pair consists of three faces with the shape a bit smaller than the long side of the CubeSat. They are modelled as rectangle shell plates with dimensions of 9.5 by 28.5 cm with dual material and thermo-optical properties for the bottom and top side to model the substrate and solar cells, respectively.

Deployable Radiator Wing

The geometric definition for the DRW is the same as described in Subsection 5.2.1

Table 9.1: Overview of the geometry definition for all the geometries in ESATAN-TMS-2019

Geometry	Shape	Geometry type	Dual properties
CubeSat wall	Box	Shell	Dual thermo-optical properties for inside and outside
DRW	Rectangle	Solid	-
Payloads	Rectangle	Shell	-
PCBs	Rectangle	Shell	-
Solar arrays	Rectangle	Shell	Dual thermo-optical and material properties for top and bottom side

9.2.2. Material and thermo-optical properties

The high conductive material PG has temperature depended properties, as presented in Subsection 4.2.1. ESATAN-TMS-2019 can easily deal with temperature dependent variables, therefore, this is included in the model. ESATAN-TMS-2019 uses the average temperature to calculate this. This means that for conductors the average temperature is taken between two nodes. However, when the difference in temperature between the nodes is high, this could lead to irregularities. For this application this is considered not to be an issue because the temperatures for the two nodes are quite similar. The temperatures between the nodes are quite similar because either the distance between the nodes is really small (for out-of-plane conductors in the DRW) when the conductivity is low or the conductivity is large when the distance between the nodes is larger (for the in-plane conductor in the DRW).

The PCBs and payloads are modelled as flat plates in the radiative calculation. However, those elements contain the most mass and, therefore, the highest total heat capacity. For simplicity, one value for the heat capacity, heat conductivity and density is used. As a reference value the effective thermal conductivity of PCBs is used. However, due to wide variety of materials of how these laminates are produced of, the thermal conductivity values differs a lot. For this purpose a conservative value of 5 W/mK is used. Usually, they can be higher [20]. For the other parameters, the values of silicon are used. The different geometrical definitions have the following material types as shown in Table 9.2.

Table 9.2: Table of assumed material properties for the CubeSat and DRW.

Material property name	Density $[kg/m^3]$	Thermal conductivity $[W/mK]$	Specific heat capacity $[J/kgK]$
Adhesive: 3M966	1012	0.178	1000
Aluminium	2700	200	902
Kapton	1420	0.46	1090
PG	1800	Temperature dependent, see Figure 3.2 and 3.5 out-of-plane	850
PCB-material	2000	5	710

Table 9.3: Overview of the values for the emissivity and solar absoptivity of the thermo-optical surface coatings used.

Thermo-optical property name	Emissivity	Solar absoptivity
White (MAP SG122FD [9])	0.9	0.18
Black [19]	0.88	0.96
Solar cells	0.64	0.85

As mentioned in the model assumptions in Section 9.1, all of the outsides are painted white, except for the solar cells. White paint has high emissivity and low absorptivity. This increases the heat emitted and minimises the heat absorbed from the Sun. Furthermore, the insides and the electronics are painted black and the solar cells will use average values for the emissivity and absorptivity. The values for emissivity and absorptivity for the different types of surface finishes are listed in Table 9.3. The different geometrical definitions have the following types of surface finishes as shown in Table 9.4. The top of the solar arrays are covered in solar cells. These cells consist of various different materials with different material properties. For simplicity, it is assumed to be the same material as the substrate on the bottom of the solar arrays. This does not have any large implications because the solar arrays do not influence the DRW directly.

9.2.3. Orbit and orientation

The lower face of the CubeSat will always point towards Earth and the Solar arrays to the Sun, as explained in Section 2.1. ESATAN-TMS-2019 is able to take this into account. The result is that the view factors change over the course of the orbit, more on this at the end of this subsection.

The assumed orbit is optimal because the Sun does not radiate directly onto the DRW because the Sun rays are parallel to the DRW. For simplicity it is assumed the Sun is at the equator and the prime meridian for these calculation. Since the albedo of Earth is assumed to be constant over the orbit, thus the Sun being over the equator does not influence the results. However, the Sun is not always over the prime meridian as Earth revolves around the Sun. Subsection 9.5.3 will investigate the influence

Table 9.4: All geometries with their respective material and thermo-optical properties.

Geometry	Material type	Thermo-optical property type
DRW		
- PG-layers	PG	No radiation
- Adhesive	3M966	No radiation
- Kapton	Kapton	White paint
Solar arrays		
- Top	Aluminium	Solar cells
- Bottom	Aluminium	White paint
Payloads	PCB-material	Black
PCBs	PCB-material	Black
CubeSat		
- Inside	Aluminium	Black
- Outside	Aluminium	White paint

of this assumption. Figure 9.1 shows the orbit of the CubeSat. Note that the solar arrays are always pointing to the Sun, yellow arrows, and that the CubeSat is always Nadir pointing.

The calculations for the view factors are performed at certain points during the orbit. Since the orientation of the CubeSat body with DRW changes with respect to the Sun, Earth and the solar cells, the view factor vary over the course of the orbit. The view factors change gradually over the orbit. However, ESATAN-TMS-2019 can only calculate the view factors discretely, at a specific point in the orbit. The more instances, more location in the orbit, these view factors are calculated, the more accurate the final calculations will be. However, calculating these view factor is a time consuming process for ESATAN-TMS-2019. The minimum number of times to compute the view factors is eight in order to stay accurate because of the changing CubeSat geometry. The geometry changes because the CubeSat always points in the Nadir direction and the solar arrays to the Sun. The orientation of the Sun is the most important. Therefore, just before and after the two eclipse points are taken, atop of the poles and where it crosses the equator. This model will use 16 points and an additional four for the entry and exit points of the eclipse where the view factor is calculated over the course of the orbit as depicted in Figure 9.1.

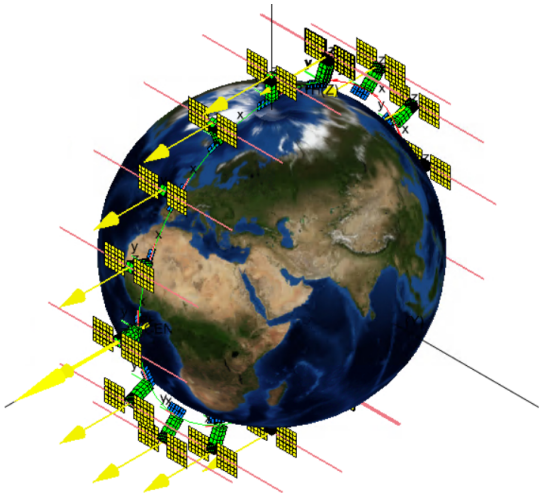

Figure 9.1: Locations of where the radiative calculations of the view factors are performed including the entry and exit points of the eclipse. The yellow arrow points to the direction of the Sun.

9.2.4. Boundary conditions

The baseline is a given power input. Therefore, the boundary conditions are an input power on various geometric definitions. From the assumptions in Section 9.1 it follows that during the eclipse, the heat input is decreased because of reduced operational activities. This makes the boundary condition dependent on where the CubeSat is during the orbit. ESATAN-TMS-2019 is capable of handling time dependent variables. These geometries and the value of the boundary are given in Table 9.5.

In addition to the defined boundaries, ESATAN-TMS-2019 generates boundary conditions from the Sun, Earth Infrared (IR), Earth Albedo and space. Since the orientation of the CubeSat with the rotating Sun-pointing solar arrays constantly change over the course of the orbit, these boundary conditions change over the orbit as well. These boundary conditions also depend on the amount of energy absorbed, which in turn depends on the emissivity, absorbtivity and the reflectivity of the surfaces. The total values are shown in Figure 9.2. A close-up is presented in Figure 9.3. The DRW has only a small drop in power during the eclipse, this is as expected because it is parallel to the solar rays. Especially the solar arrays receive a lot of solar radiation, Earth Albedo and Earth IR. The body of the CubeSat receives less of the solar radiation. ESATAN-TMS-2019 is based on that space acts as a heat sink with a temperature of -270°C, the default value for the temperature of space in ESATAN-TMS-2019. All heat generated is radiated to space. These boundary conditions are used in ESATAN-TMS-2019 to calculate the heat flows and temperatures in the model.

Table 9.5: Boundary condition during daytime and eclipse.

Location	Daylight conditions	Eclipse conditions
PCB (total)	10.0	5.0
Payload 1	10.0	5.0
Payload 2	10.0	5.0
Total	30.0	15.0

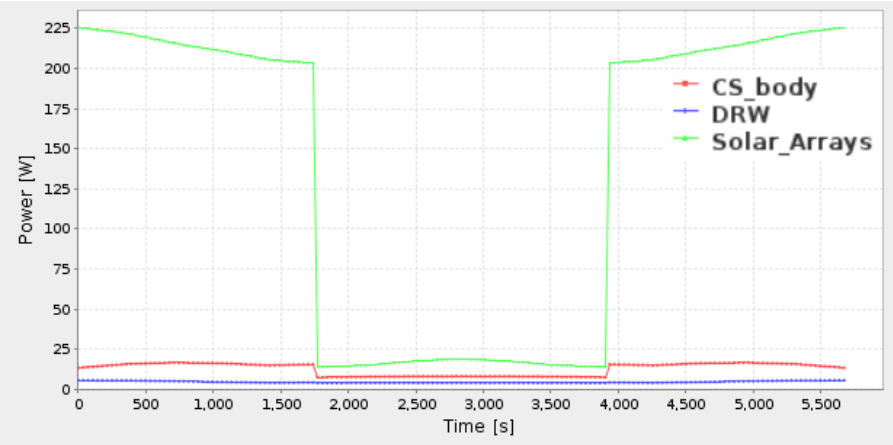

Figure 9.2: Total boundary heat flow over the course of the orbit for the body of the CubeSat, the solar arrays and the DRW calculated by ESATAN-TMS-2019.

9.2.5. Nodes and grid pattern

The geometric shapes defined in Section 9.2, are subdivided in nodes and forming a grid. These nodes are represented as rectangular nodes, because the model does not contain any circles or arcs. The nodes have the shape of a rectangular for the solid boxes and rectangles for the shells. The solar arrays have a dual composition, so they have nodes for each side of the shell surface. Other shell surfaces use the same node for both sides. The solid geometries follow the lumped parameter method. This means that the middle of an item in the grid contains all the mass and capacity. There are also nodes on the sides of this rectangular.

Each group of nodes has its own starting node number as followed from Table 9.6. The node numbering increases with increments of 1. This is used for referencing nodes later in this chapter.

Table 9.6: Node numbering convention for each geometry.

Node numbering	Starting number
DRW	10000
PCBs	40000
Payload 1	50000
Payload 2	60000
CubeSat body	70000
Interface	80000
Solar array	90000
Inactive node	99998
Space node	99999
Node increment	1

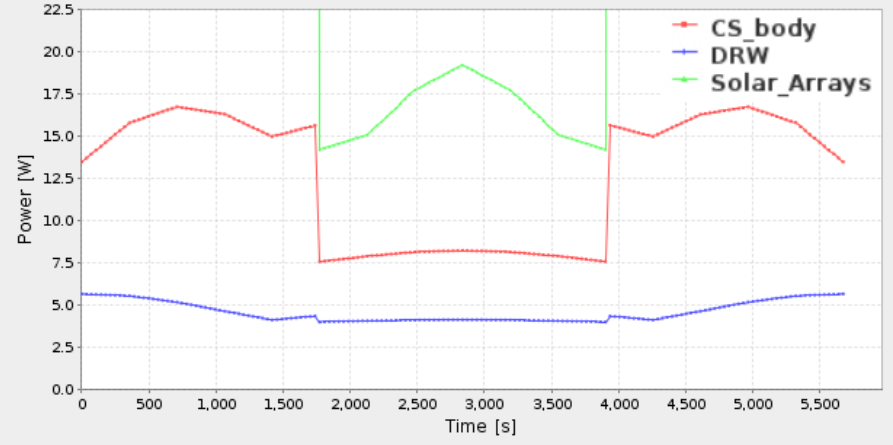

Figure 9.3: Close-up of Figure 9.2 of the total boundary heat flow over the course of the orbit for the body of the CubeSat and the DRW calculated by ESATAN-TMS-2019.

9.3. Model explanation

The model explanation for the system model is the same as described in Appendix D. However, instead of a steady state solution, a cyclic solution is used to model the revolutions around Earth.

The parameters solving the analysis file are defined in the thermal file. To simplify the model calculations over the orbit, it is assumed that the CubeSat is in a stable orbit around Earth and it is assumed that the starting point of the orbit is the same as the end point of the orbit, because the CubeSat revolves around the Earth repetitively. As a result, the temperatures and heat flows are equal at the start and the end of a revolution around Earth. This also means that the temperature profile is the same for each orbit. In order to solve this, the cyclic solver of ESATAN-TMS-2019 is used. This solver iterates over many orbits to find the cyclic solution where the starting conditions are equal to the final conditions.

9.4. Model analysis

In this section the analysis of the model is performed to provide an answer on RQ-3 by comparing the temperature progression over the orbit of two analysis cases: with and without the DRW. First, it starts with the definition of the performance in Subsection 9.4.1. This subsection explains the variables that are important in order to compare the obtained results. Then, the radiative case is defined for which the analysis is performed in Subsection 9.4.2. Then two analysis cases are defined, one model with the DRW and one without the DRW in Subsection 9.4.3 and Subsection 9.4.4 respectively. These two analysis cases are combined with the radiative case and solved with the results presented in Subsection 9.4.5 and the results are discussed in Subsection 9.4.6.

9.4.1. Performance definition

From the output files, the analysis results can be extracted. The results contain the temperatures of all nodes and the heat flows of all conductive links for each time step. In order to reduce the amount of data, the important data is identified. Since the goal is to investigate the effusiveness of the DRW for cooling the hot insides of the CubeSat, thus the temperature of the payloads and PCBs are important to compare for the case with and the case without the DRW. In addition to this, it is useful to know how much heat flows from the payloads and PCBs to the interface of the DRW and the temperature gradient over the DRW for determining its efficiency.

9.4.2. Radiative case: 500 *km* orbit around Earth

The radiative case is defined as a 500 km orbit with a 90° inclination, as explained in Section 2.1, and a 0° right ascension node, such that the Sun does not illuminate the DRW. The bottom of the CubeSat model is always pointing in Zenith direction and the Solar arrays rotate always such that it is perpendicular to the solar rays. The ray tracing is performed on multiple instances over the orbit to take into account the different view factors over the course of the orbit with the changing orientations of the CubeSat and solar arrays with respect to the Sun, Earth and each other, as explained in Sub-

section 9.2.3. Over the course of the orbit every 22.5° the radiative calculations for the view factors are performed, thus creating a total of 16 cases, as shown in Figure 9.1. Furthermore, the are four additional instances to calculate the view factors just before and just after the two eclipse points.

9.4.3. Analysis case 1: with Deployable Radiator Wing

The first analysis case is the model as defined in Section 9.2 including the DRW and with the radiative case defined in Subsection 9.4.2. The results are presented in Subsection 9.4.5 and are analysed and discussed in Subsection 9.4.6. Figure 9.1 shows the CubeSat model including the DRW in orbit around Earth. Figure C.1 shows a schematic overview of the CubeSat model including the DRW. More figures of the model created in ESATAN-TMS-2019 are shown in Appendix C.

The boundary condition is a heat load on the two payloads and all PCBs in the model. This heat load is halved during the eclipse. Table 9.5 provides an overview of the heat loads and their locations. The orbit and orientation is as presented in Subsection 9.2.3. Additional boundary conditions are applied by ESATAN-TMS-2019 on all surfaces to represent the radiation from the Sun and Earth.

9.4.4. Analysis case 1: without Deployable Radiator Wing

The second analysis case is the model without the DRW, otherwise, it is as the analysis case 1 in Subsection 9.4.3 and the radiative case in Subsection 9.4.2. The results are presented in Subsection 9.4.5 and are analysed and discussed in Subsection 9.4.6.

The boundary condition is a heat load on the two payloads and all PCBs in the model. This heat load is halved during the eclipse. Table 9.5 provides an overview of the heat loads and their locations. This boundary condition the same as in analysis case 1 in Subsection 9.4.3 The orbit and orientation is as presented in Subsection 9.2.3. Additional boundary conditions are applied by ESATAN-TMS-2019 on all surfaces to represent the radiation from the Sun and Earth.

9.4.5. Results of the two analysis cases

This subsection presents the results obtained from the two analyses cases defined in Subsection 9.4.3 and Subsection 9.4.4.

Analysis case 1 with the DRW contains more nodes and conductive links than analysis case 2 without the DRW. Some figures may show values for nodes that may not be present in analysis case 2.

The results for the temperature progression of analysis case 1 and 2 are combined into Figure 9.5. The continues lines show analysis case 1 with the DRW and the dashed lines show analysis case 2 where the CubeSat does not have a dedicated radiator. The start and end of the eclipse is shown with two black vertical lines. The temperature progression of multiple locations is shown. The legend contains the node numbers of those locations as per Table 9.6. Since there is no DRW for analysis case 2, the temperature progression is not shown for this (node number series 10000). Note that the green and red lines for the payloads overlap in the model with DRW because of the high conductive thermal link between the payloads and the DRW and thus to each other indirectly too. The temperature of the nodes (T10026 and T10044) on the DRW are at equal distance to the interface and have, therefore, equal temperatures, thus those lines overlap. An overview of the nodes and their location is presented in Table 9.7 and Figure 9.4.

The heat flow over time to the DRW from analysis case 1 is shown in Figure 9.6. The results from Figure 9.5 tells not much about the flow of heat. The model consists of many nodes with many conductive links connecting each other. There are too many nodes to give an overview. Therefore, the nodes of each of the geometries are compressed/combined into one node each for readability. This results in a nodal network diagram of eight group of nodes with only a few conductive links. For analysis case 1 with the DRW this is shown in Figure 9.7 when the CubeSat passes the Sun-Earth plane up ($t = 0\ s$) and the end of the eclipse ($t = 3900\ s$) in Figure 9.8. A nodal network diagram of only the DRW is given in Figure 9.9. Analysis case 2 does not have a DRW and, therefore, has two group of nodes less, the DRW itself and the connector between the payloads and DRW. This results in a nodal network diagram presented in Figure 9.10 at $t = 0\ s$ and Figure 9.11 at $t = 3900\ s$.

Table 9.7: Overview of the locations of the nodes.

Node number	location
10006	DRW opposite of the interface
10026	left side of DRW
10044	right side of DRW
40000	bottom PCB, closest to payload 2
40072	top PCB, furthest from payload 2
50000	payload 1
60004	payload 2
90083	tip of solar array

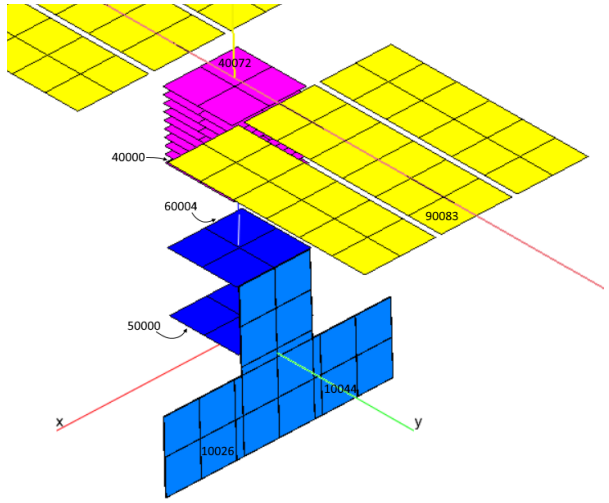

Figure 9.4: Overview of the locations of the node number from Table 9.7 (the CubeSat body geometry is hidden).

9.4.6. Discussion of the results

The temperature of the payloads decrease with the DRW by 23 to 27°C for payload 2 and payload 1 respectively. This drop in temperature is almost constant over the course of the orbit. Even the stack of PCBs decrease in temperature with the inclusion of the DRW. The influence of the DRW is demonstrated by comparing the temperatures of the CubeSat model with and without the DRW. Figure 9.5 shows the temperature progression over the orbit for the nodes from Table 9.7 which are shown in Figure 9.4. This is shown for the case with the DRW as a continuous line and for the case without the DRW as a dashed line. This provides the information to answer RQ-3. This information is later used to answer the Main research question. The temperatures of the model with DRW are much lower. The DRW provides an efficient heat flow path between the payloads and space. Instead of the heat flow going through the walls of the CubeSat and via radiative links to space, it is transported via a conductive links to the DRW (via the interface) and to space. This is supported by the heat flow to the DRW in Figure 9.6. The flow of heat in the thermal links becomes visible in the nodal network in Figure 9.7 and Figure 9.8. The influence of the DRW is illustrated further by the nodal network in Figure 9.10 and Figure 9.11 where there is no DRW installed. In these two figures, the heat from the payloads have to go via the CubeSat body to space. The heat flow between the CubeSat body and space is 18% lower with a DRW. Judging on the lower temperatures in the figures with the DRW the thermal link between the payloads and space is more efficient (low resistance) via the DRW.

In the close-up of the nodal network of the DRW in Figure 9.9, the heat from the payloads in applied in the 'middle' node, led to the 'flap' and to each side of the DRW. It receives some radiation from the solar arrays and radiates some to the CubeSat body, but most of the heat is radiated to space. This makes it efficient.

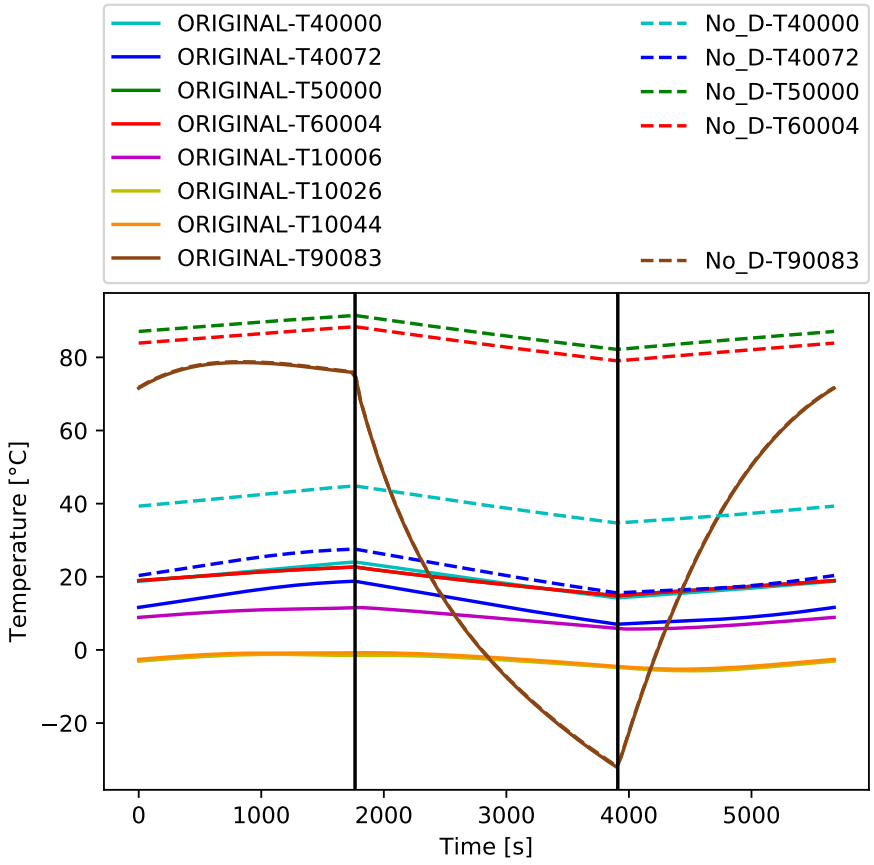

Figure 9.5: Temperature progression of the model with and without DRW for various temperature measurement locations with start and end of the eclipse.

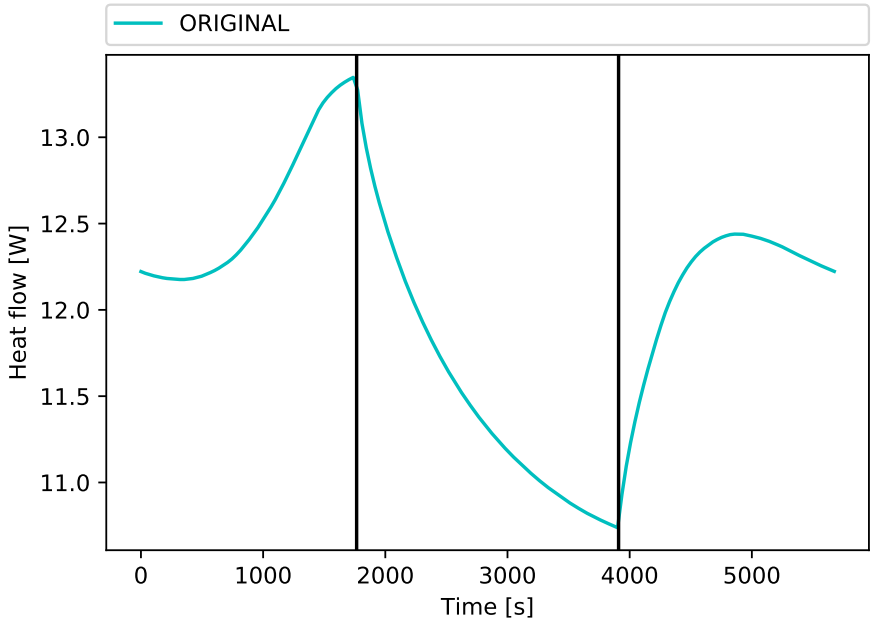

Figure 9.6: Heat flow progression of the model with DRW with start and end of the eclipse.

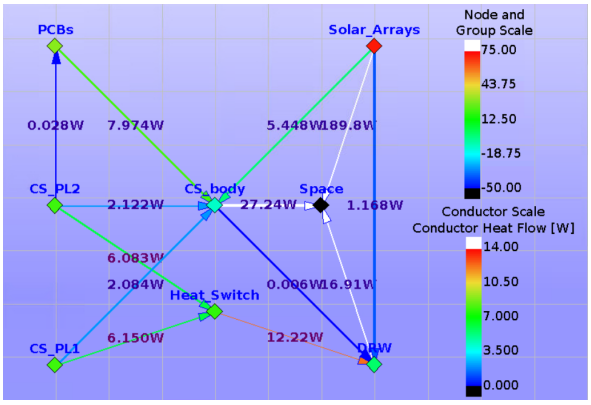

Figure 9.7: Compressed nodal network for the CubeSat model with DRW at $t = 0$ s.

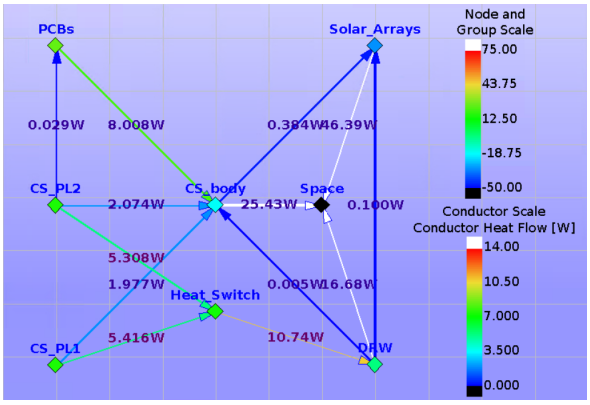

Figure 9.8: Compressed nodal network for the CubeSat model with DRW at $t = 3900$ s.

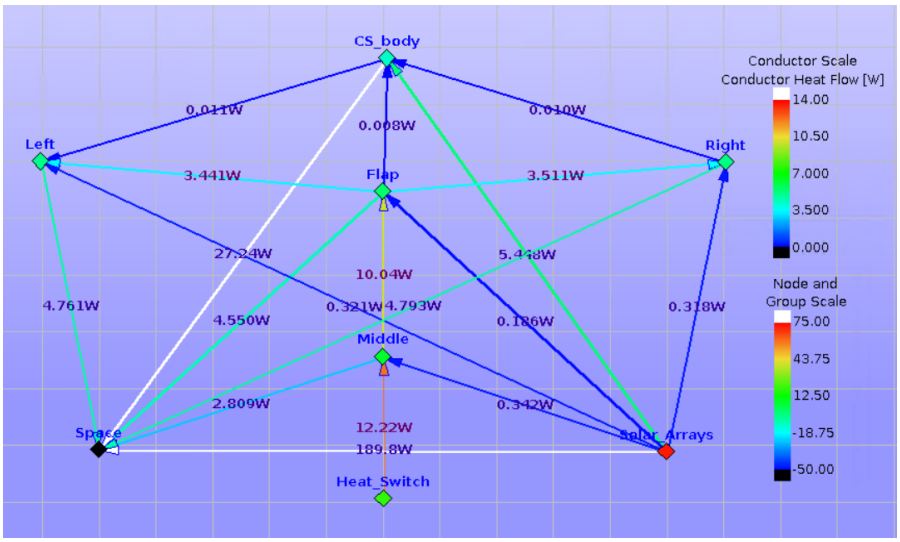

Figure 9.9: Compressed nodal network for the DRW at $t = 0$.

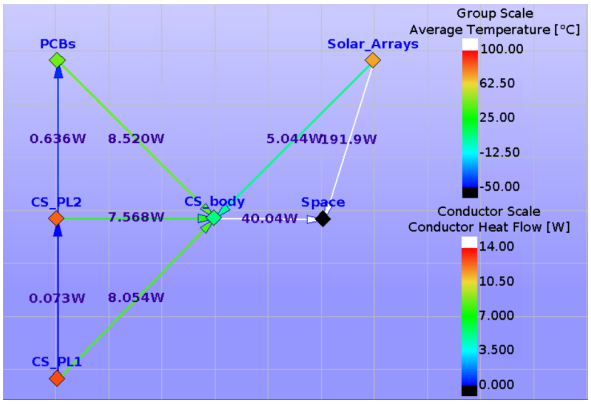

Figure 9.10: Compressed nodal network for the CubeSat model without DRW at $t = 0$ s.

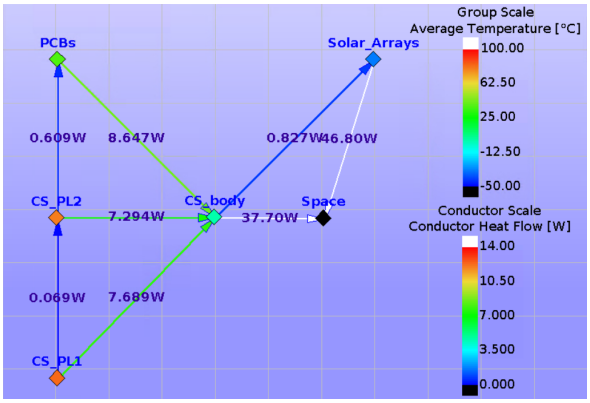

Figure 9.11: Compressed nodal network for the CubeSat model without DRW at $t = 3900$ s.

9.5. Sensitivity analysis of the numerical model

Due to uncertainties in the assumptions and the parameters presented in this chapter, it is necessary to investigate the influence of these assumptions and parameters. By challenging the assumptions and changing the parameters and calculate the model performance, it can be determined whether an unforeseen change in the assumptions and parameters are of influence to the performance of the system.

The temperature and the heat flows could help to investigate how changing assumptions and parameters affect the radiator's performance. CubeSat instruments and subsystems have temperature constraints. A change in the temperatures, is of importance. When comparing the internal heat generated (from the set boundary conditions) to the heat flow from the DRW to space it can be determined how effective the addition of the DRW is. The numerical model has a few hundred conductive links between the DRW and space. To analyse this twice as many output parameters are required in the parametric analysis to calculate the heat flows. However, the output of the parametric analysis of ESATAN-TMS-2019 is constrained to only a few dozen output parameters. So this method is not usable. Alternatively, it is possible to analyse the heat flow between the payloads and the DRW, since that is only one conductive link, it requires only three output parameter to calculate the heat flow (one for the conductivity and two for the temperatures). The heat flow of the payloads to the DRW provides similar information about the performance of the radiator as the heat flow of the DRW to space. However, the heat flow from the payloads to the DRW is not equal to the heat radiated from the DRW to space because the DRW receives heat from different sources, such as Earth and other CubeSat surfaces. Additionally, the alternative measure provides more insight in the influence of creating an additional heat flow path between the payloads and space due to the inclusion of the DRW. However, the true amount of heat radiated from the DRW to space is unknown from the parametric analysis. An other method to obtain the heat flow between the DRW to space is to use a different software package, but that overcomplicates the analysis for this section. Including the many heat flows between the DRW and space in the output parameters is, therefore, not possible. Therefore, the heat flow analysed in this section, is the heat flow between the interface (node 80001) and the first node of the DRW (node 12558). This heat flow is shown in the figures. The temperature is defined as the temperature of payload 1 (node 50000) but the temperature of payload 2 and the other nodes in payload 1 are basically identical. The cyan coloured line with "Original" in the figures presented in Subsection 9.5.1 and further.

9.5.1. Sensitivity on input power

The input power is the amount of heat generated by the systems of the CubeSat such as the instruments, telemetry and electronics. Increasing the amount of heat generated will result in higher temperatures for the systems of the CubeSat. CubeSat systems have a range of temperatures for which it is still possible to operate. It is important to know what the system temperatures are for a range of input power levels.

The power input to the stack of PCBs is kept the same for this sensitivity analysis as for the original model. This is because the stack of PCBs is not connected to the DRW via the thermal link, otherwise this will cause the stack of PCBs to overheat disproportionately more than the payloads, which are connected to the DRW. The input power for each payload is multiplied by a factor of 0.5, 1.25, 1.5, 1.75 and 2.0. The resulting power levels are shown in Table 9.8.

Table 9.8: New input parameters for the input power of the payloads for the sensitivity analysis.

Power conditions	0.5 * normal		Normal		1.25 * normal		1.5 * normal		1.75 * normal		2.0 * normal	
Sunlight conditions	Sun lit	Eclipse	Sun lit	Eclipse	Sun lit	Eclipse	Sun lit	Eclipse	Sun lit	Eclipse	Sun lit	Eclipse
PCB (total)	10	5	10	5	10	5	10	5	10	5	10	5
Payload 1	5	2.5	10	5	12.5	6.75	15	7.5	17.5	8.75	20	10
Payload 2	5	2.5	10	5	12.5	6.75	15	7.5	17.5	8.75	20	10
Total	20	10	30	15	35	17.5	40	20	45	22.5	50	25

The temperature of the payloads increases with increasing heat load on the payloads as can be seen in Figure 9.12. It is observed that the heat flow between the payloads and DRW increases with increasing heat load, see Figure 9.13. This heat flow is proportional to the temperature gradient. To

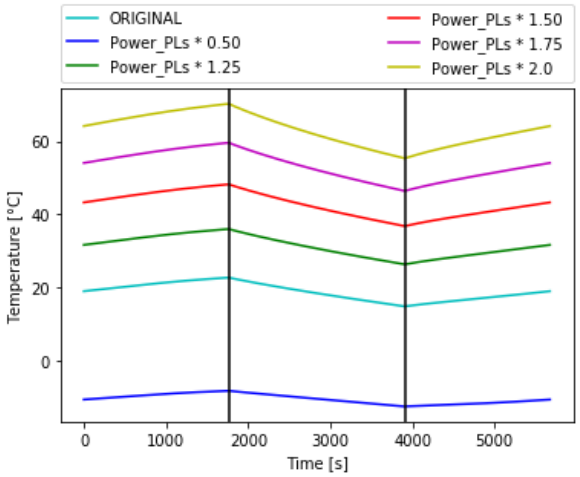

Figure 9.12: The temperature progression over the course of the orbit for increasing internal heat production by the payloads following Table 9.8.

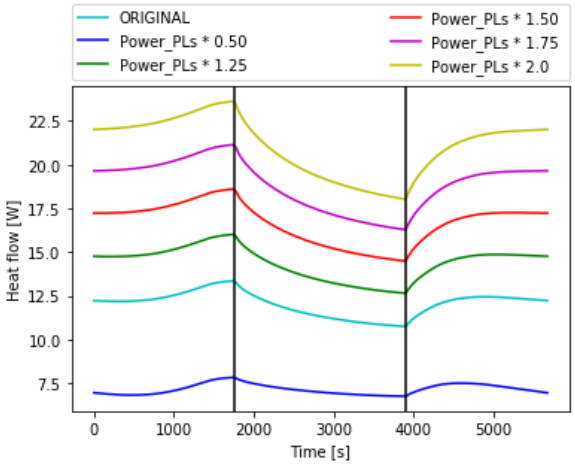

Figure 9.13: The heat flow progression over the course of the orbit for increasing internal heat production by the payloads following Table 9.8.

accommodate this increase in heat flow, the temperature gradient must increase. This can be achieved by an decrease in the sink temperature, an increase in the source temperature or a combination of both factors. The sink temperature is the temperature of space. This is a constant and can, therefore, not decrease. Therefore, the source, the payload, temperature is increased. Thus, explaining the increase in the temperature of Figure 9.12.

When increasing the heat load generated in the payloads the temperature and the heat flow to the DRW increase as expected. The original model has a heat flow between the payloads and the DRW of around 12 W which is 40% of the heat input of 30 W. Increasing the heat load, increases the heat flow to the DRW, see Figure 9.13. The percentage of the heat flow between the payloads and the DRW with respect to the total heat generated in the CubeSat stays constant around 40% for increasing heat load. This means that the DRW scales well with the increasing heat load.

9.5.2. Sensitivity on number of PG layers

The more adhered PG sheets, the thicker the radiator becomes. Increasing the thickness of the radiator creates a more even temperature distribution because the thermal conductivity increases. As a result, the edges have higher temperatures. This increases the radiative heat flow to space. However, a thicker radiator also increases the mass. Therefore, it is important to know to what extend adding PG sheets will influence the thermal performance while keeping the mass low. This subsection provides an answer to RQ-5.

Increasing the number of layers of the DRW will result in a more even temperature distribution over the surface of the DRW. This results in higher temperatures further away from the source and thus more radiative heat transfer to space. From Figure 9.14 it becomes clear that the increase in the number of layers causes the temperature to drop. This drop reaches a limit after 24 layers. However, with 24 layers the mass increases by almost a factor of two with respect to the original 12 layers, while only resulting in a drop of 2°C. Figure 9.15 shows that the heat flow increases during day time, but is lower during the eclipse for increasing number of layers. The average heat flow for an increasing number of layers increases only with up to 2%, from 12.04 W to 12.28 W for 36 layers. The increase in thermal performance for more PG sheets is small. A radiator with more than 24 PG sheets does not have a significant contribution to the thermal performance.

9.5.3. Different orbits

The orientation of the CubeSat with respect to the Sun changes over the revolution of Earth around the Sun. This means that the amount of illumination from the Sun on the DRW changes, depending on where the DRW is located in the Earth's orbit around the Sun. The changing illumination is between minimal when the orbit to be such that the Sun illumination on the DRW is zero. This is assumed in

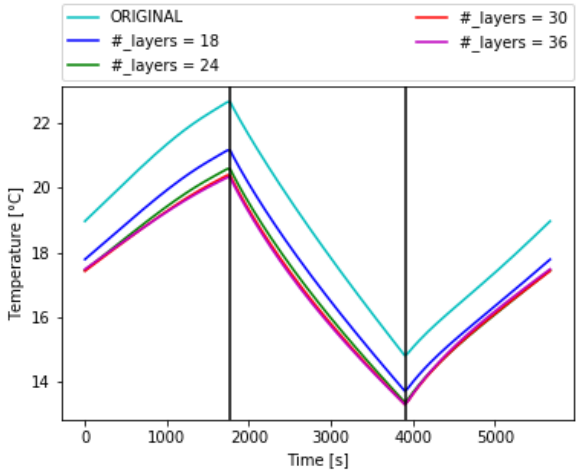

Figure 9.14: The temperature progression over the course of the orbit for increasing the number of layers in the DRW.

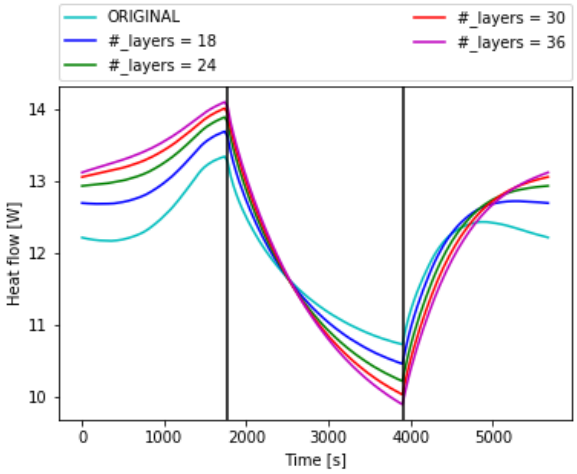

Figure 9.15: The heat flow progression over the course of the orbit for increasing the number of layers in the DRW.

the analysis of the original model in Section 9.4. The illumination is maximal a quarter of a year later. Therefore, the assumption that the radiator is not illuminated by the Sun is not true. This subsection will investigate the influence of this illumination on the DRW on the performance of the DRW and provides an answer to RQ-4. The influence of the Sun during a different quarter is investigated. The assumption in the original model is that the rays of the Sun are always parallel to the DRW. This is not always the case. At certain times, twice per orbit at a quarter year difference from the minimal illumination, the Sun rays will be perpendicular to the DRW, thus adding a solar flux. This will cause the heat flow from the payloads to decrease to keep the net heat flow to space constant. This decrease is unfavourable. When the DRW is installed in the plane perpendicular to the axis of rotation of the solar arrays, there is no sunlight on the solar arrays when the Sun is perpendicular to the DRW. Since it is always favourable to have sunlight on solar arrays, it is likely that the CubeSat is rotated such that there is some sunlight on the solar arrays. As a result, the angle between the DRW and the Sun decreases. A Sun angle of 45° on the solar arrays and DRW is more likely.

Increasing the angle of incidence of sunlight on the DRW, Ω, increases the temperature as seen in Figure 9.16 because the heat flow to the DRW decreases to 9.6 W. This is 20% less at $\Omega = 90°$. However, as stated before, the CubeSat will probably rotate 90°around the z-axis because the solar arrays do not receive any sunlight otherwise. Rotating the CubeSat 90°around the z-axis will reduce the angle of incidence of the sunlight on the DRW reduces to zero and reduces the temperatures. The angle between the DRW and the Sun is depended on the location of the CubeSat in the orbit around Earth and on the location of Earth in the orbit around the Sun. Other factors have an influence too, such as the desired amount of Sun illumination on the solar arrays and the orientation of the CubeSat with Earth depending on the instrument requirements.

9.5.4. Full power during eclipse time

The CubeSat is once per orbit around Earth in an eclipse. In an eclipse, there is no solar heat flux and an assumed reduction in operational power. This causes the temperature of the CubeSat to drop. It may be beneficial to extend periods of high operation even during an eclipse. Increased power during the eclipse will cause the temperature to increase too. In addition, the increased power during eclipse could also cause to a temperature rise during daylight operations and potentially exceeding the temperature constraints of the instruments. Therefore, it is important to know what the influence of these types of operations are on the temperature. For this analysis, it is assumed that the input power is the same for the eclipse and daylight operations for multiple revolutions and that the cyclical equilibrium temperature is reached.

Instead of halving the heat load on the payloads and the stack of PCBs, the heat load is held constant for the eclipse as during day time. There are three significant differences as a result. From Figure 9.18 it is clear that the overall temperature is much higher and quite constant over the course of the orbit in comparison with the original model. Since there is no drop in heat load, the heat flow to

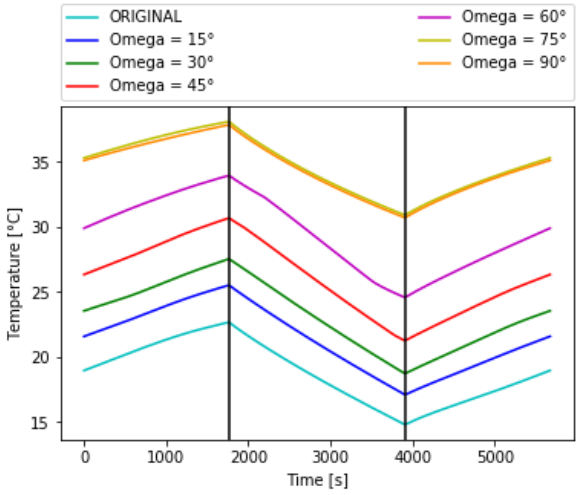

Figure 9.16: The temperature progression over the course of the orbit for orbits with different longitudes of ascending node.

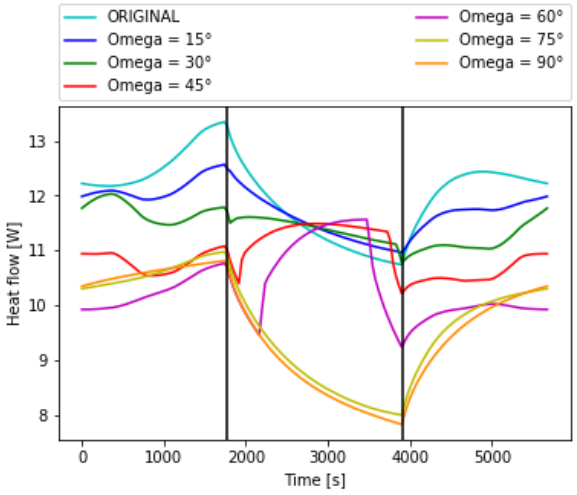

Figure 9.17: The heat flow progression over the course of the orbit for orbits with different longitudes of ascending node.

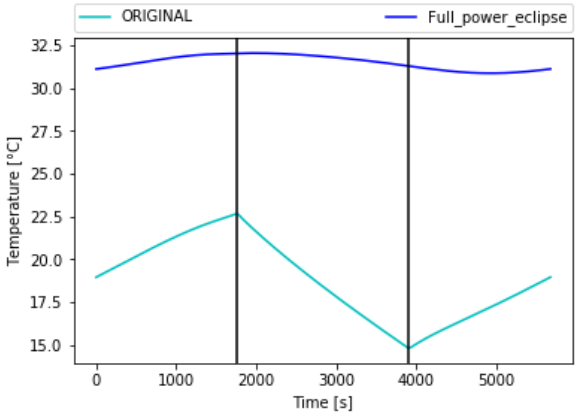

Figure 9.18: The temperature progression over the course of the orbit for when the heat load is not halved during eclipse.

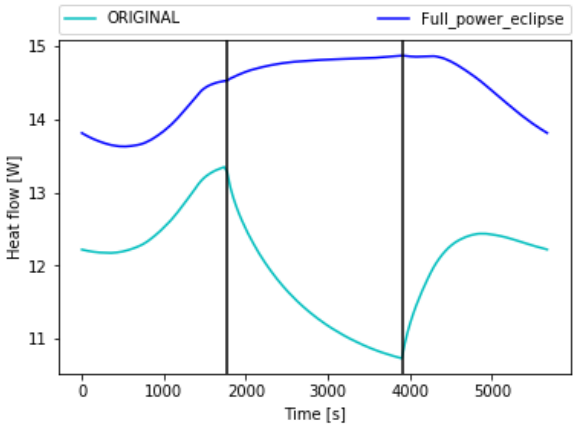

Figure 9.19: The heat flow progression over the course of the orbit for when the heat load is not halved during eclipse.

the DRW stays high during the eclipse, as can be observed in Figure 9.19. As a result there is also no significant temperature drop during the eclipse, as can be observed in Figure 9.18. The heat flow increases during day time (around 15%) and the eclipse (up to 35%).

The increase in the temperature in daytime with the full power eclipse could be explained by the fact that with the half power eclipse, in the original version, the eclipse happens before the spacecraft is able to reach the equilibrium temperature. With full power during eclipse, there is no sudden stop and thus the temperature can rise closer to the equilibrium temperature. The small variation observed in the temperature progression is probably the influence of the Sun. Even though there is no Sun radiating on the DRW, the albedo of the Earth does heat the DRW a bit. This causes the DRW to heat up and with the smaller temperature gradient between the payloads and the DRW the heat flow goes down. During the eclipse there is no albedo and thus with the higher temperature gradient, the heat flow increases.

The maximum temperature from Figure 9.18 is 4.5°C lower than the equilibrium temperature for the spacecraft (37.0°C) from Table 10.2.

9.5.5. Sensitivity on the thermal conductivity of PG

The conductivity of the PG layers is an important factor for the thermal performance of the DRW. This subsection investigates the change in performance for small deviations in the thermal conductivity of the PG sheets. The thermal conductivity of the PG is varied between -20% and +20% of the original which is defined in Figure 3.2.

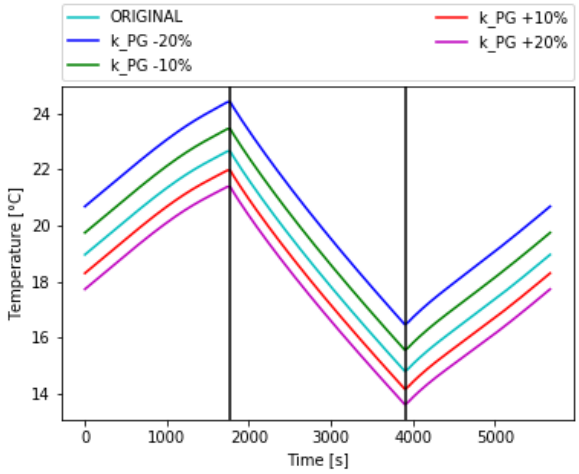

Figure 9.20: The temperature progression over the course of the orbit for variations in the thermal conductivity of the PG sheets.

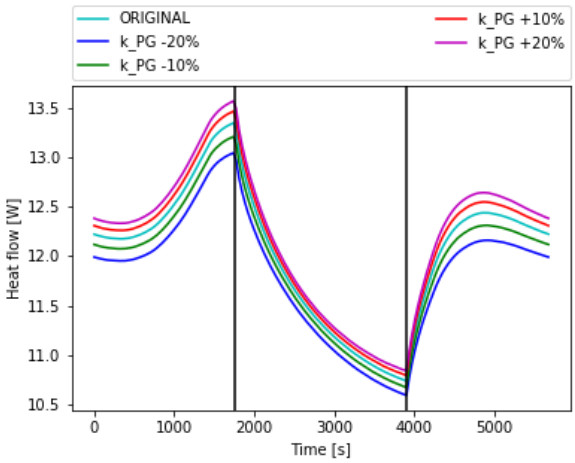

Figure 9.21: The heat flow progression over the course of the orbit for variations in the thermal conductivity of the PG sheets.

A change in the thermal conductivity of PG does not result in any significant change in temperature, Figure 9.20, or heat flow, Figure 9.21. So this is considered not to be a risk.

9.5.6. Boundary condition change: minimal operating power

Instead of having boundary conditions giving a high heat input, it is possible to set the heat input at a minimal level. This minimal level would simulate the thermal conditions when there are no instruments working and thus no heat generated for extended periods of time. This large radiator introduces a large heat loss, even during conditions when this is not desired. The CubeSat instruments and equipment have a lower limit for the temperature. This lower temperature limit must not be exceeded. Therefore, it is important to understand the mechanics and behaviour of the system during low power operations to take precautions to prevent exceeding the lower limits.

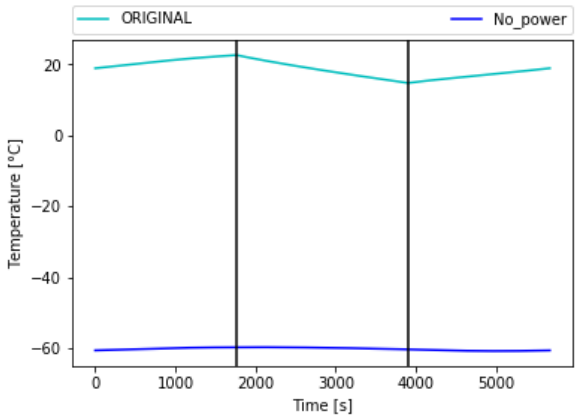

Figure 9.22: The temperature progression over the course of the orbit for no heat loads on the payloads and PCBs

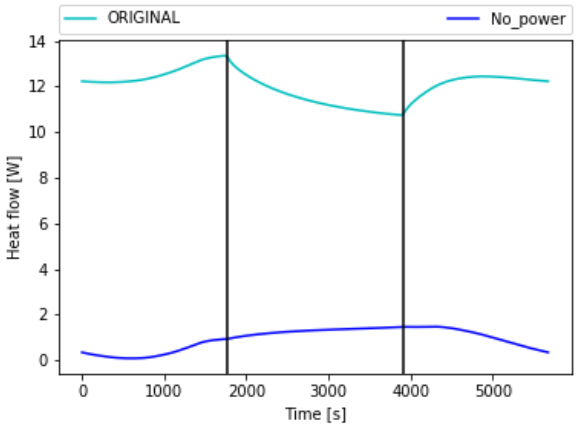

Figure 9.23: The heat flow progression over the course of the orbit for no heat loads on the payloads and PCBs

From Subsection 9.5.1 the temperature drops below 0°C when the boundary conditions of the payloads for the heat generated are halved with respect to the original. Some subsystems could have difficulties with such a low temperature already. In absence of any power source over the full orbit, the heat flow to the DRW is around zero, from Figure 9.23. It does not drop below zero. If it were that would mean that there is a net heat flow from the DRW to the payloads. Interestingly, the shape of the heat flow progression is quite similar to Figure 9.19 where the power load is held constant over the eclipse. This is actually the case here, though the power load is zero. This is probably caused by the

albedo and the absence of albedo during the eclipse as explained in Subsection 9.5.4.

9.6. Model influences

The model is an approximation of the reality. However, not everything is easy to parameterise, so errors can occur. In Section 9.5 it is explained how the parameters variate and how these parameters have a direct link to the performance of the DRW. This section describes the variations of the parameters that are used to describe the model, but has a lower apparent link to the performance of the DRW.

The assumed value for the conductivity of the payloads and stack of PCBs is challenged in Subsection 9.6.1. The assumed value for the thermal link between the payloads and the DRW is challenged in Subsection 9.6.2.

9.6.1. Variation of the thermal conductivity of various CubeSat elements

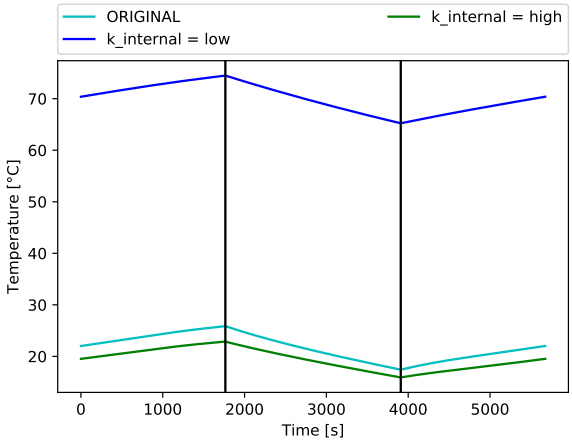

Figure 9.24: The temperature progression over the course of the orbit for low and high conductivity of the materials of the payloads and PCBs.

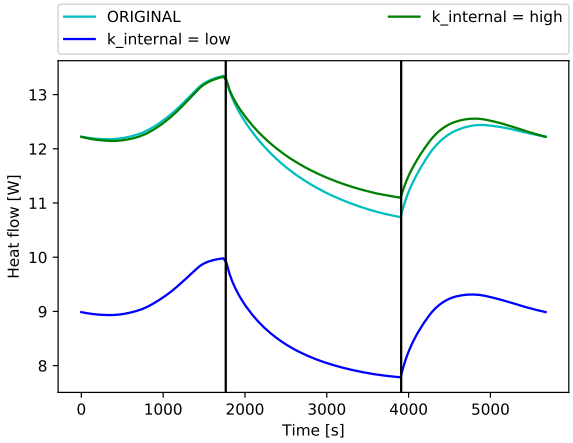

Figure 9.25: The heat flow progression over the course of the orbit for low and high conductivity of the materials of the payloads and PCBs.

The payloads and the PCBs have an internal conductivity to simulate the mass and volume of the materials, this is 5 W/mK. Reducing this by a factor of 100 to 0.05 W/mK, causes the temperatures on one side of the payloads to increase to over 70°C, see Figure 9.24, whereas the other side is around 2°C. Furthermore, the heat flow from the payloads to the DRW decreases significantly, as shown in Figure 9.25. This means that the heat flow through the walls of the CubeSat increases. The large temperature gradient is explained by how the geometry is modelled. It is modelled as a shell rectangle with edges of 10 by 10 cm and at a (virtual) thickness of 5 cm. The heat of the boundary condition is spread evenly on each side of the shell rectangle. A thermal link connects the top and bottom face of the shell rectangle.

On the other hand, increasing the thermal conductivity of the payloads and PCBs by a factor of 1000 lowers the temperature only slightly. The heat flow is slightly higher than the original model at the end of the eclipse.

For payloads with high conductivity, the assumption of 5 W/mK is true. However, for payloads with small conductivity, this does not hold true. Since this is payload and, therefore, CubeSat mission specific, must be analysed again for the specific mission.

9.6.2. Variation of the conductivity of the thermal link between the payloads and the DRW

The model assumes a high thermal conductivity of 100 W/K for the conductive link between the two payloads and the DRW. This internal conductive link can be a heat pipe or a thermal strap. The wide range of performances is not reflected in the model. Therefore, it is important to investigate the influence of a change in the thermal conductivity of the thermal link between the payloads and the DRW.

In the original model the conductivity of the thermal link between the payloads and the DRW is 100 W/K. Reducing it to 10 W/K does not show a significant change in the temperature and heat flow, as can be seen in Figure 9.26 and Figure 9.27 respectively. Even though, the legend of Figure 9.26 and Figure 9.27 refer to a heat pipe, it can be any thermal link. Decreasing the conductivity of the thermal link by a factor of 100 with respect to the original model increases the temperature by approximately 5°C. The heat flow as shown in Figure 9.27 is only decreased by around 8% but follows the same curve. Therefore, reducing the thermal conductivity of the thermal link by a factor of 100 does not give a significant decrease in performance. However, following from Figure 9.26 and Figure 9.27, decreasing the conductivity by a factor of 1000 from the original model, does create a much larger discrepancy. Therefore, as long as the conductivity is more than 1 W/K, the consequences on the performance are minimal. Further research on the performance of thermal links for CubeSat is needed to conform this.

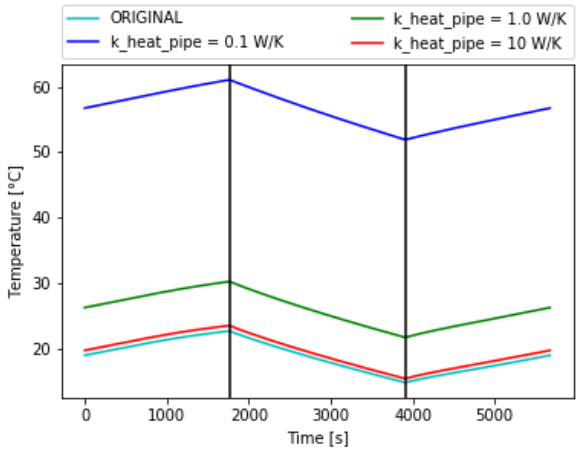

Figure 9.26: The temperature progression over the course of the orbit for decreasing conductivity of the thermal link between the payloads and the DRW.

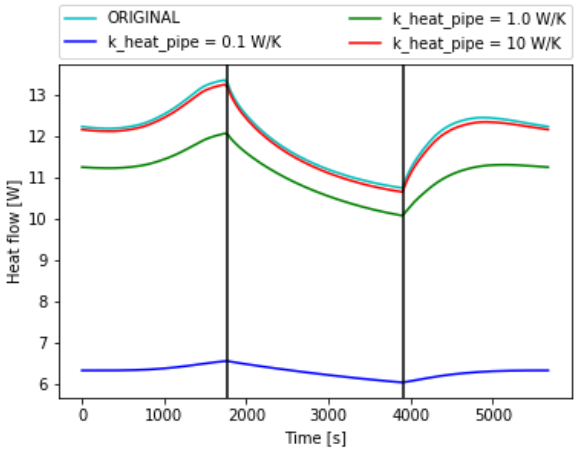

Figure 9.27: The heat flow progression over the course of the orbit for decreasing conductivity of the thermal link between the payloads and the DRW.

The results of the sensitivity analysis from Section 9.5 and the model influences of Section 9.6 are summarised in Table 9.9. This table shows the average temperatures and heat flows. In addition, the table shows to what significance these results differ from the original model.

Table 9.9: The results of the sensitivity analysis: average temperature of the payloads and average heat flow between the payloads and the DRW over the orbit.

Analysis	Significance with respect to the original model	Heat flow between the payloads and the DRW [W]			Temperature of the payloads [°C]		
		Average	Min	Max	Average	Min	Max
Original model		12.0	10.7	13.3	18.8	14.8	22.6
k_internal = low	High	8.9	7.8	10.0	70.0	65.3	74.4
k_internal = high	Small	12.2	11.1	13.3	19.4	15.9	22.8
Power_PLs * 0.50	High	7.2	6.8	7.8	-10.5	-12.6	-8.3
Power_PLs * 1.25	High	14.4	12.6	16.0	31.2	26.3	35.9
Power_PLs * 1.50	High	16.7	14.5	18.6	42.7	36.8	48.2
Power_PLs * 1.75	High	18.9	16.3	21.1	53.3	46.4	59.5
Power_PLs * 2.0	High	21.1	18.0	23.6	63.1	55.3	70.2
k_PG -20%	Small	11.8	10.6	13.0	20.5	16.5	24.4
k_PG -10%	Small	11.9	10.7	13.2	19.6	15.6	23.4
k_PG +10%	Small	12.1	10.8	13.5	18.1	14.2	22.0
k_PG +20%	Small	12.2	10.8	13.6	17.6	13.6	21.4
Full_power_eclipse	High	14.4	13.6	14.9	31.5	30.9	32.1
k_heat_pipe = 0.1 W/K	High	6.3	6.0	6.6	56.6	51.9	61.0
k_heat_pipe = 1.0 W/K	Medium	11.1	10.1	12.1	26.0	21.7	30.2
k_heat_pipe = 10 W/K	Small	11.9	10.6	13.2	19.5	15.4	23.5
No power	High	0.9	0.1	1.5	-60.3	-60.8	-59.8
Ω = 15°	Small	11.8	11.0	12.6	21.4	17.1	25.5
Ω = 30°	Medium	11.4	10.8	12.0	23.2	18.8	27.5
Ω = 45°	Medium	10.9	10.2	11.5	26.1	21.3	30.7
Ω = 60°	High	10.3	9.2	11.6	29.5	24.6	33.9
Ω = 75°	High	9.7	8.0	11.0	34.7	30.9	38.1
Ω = 90°	High	9.6	7.8	10.8	34.5	30.7	37.8
# of layers = 18	Small	12.2	10.5	13.7	17.5	13.7	21.1
# of layers = 26	Small	12.3	10.2	13.9	17.1	13.4	20.6
# of layers = 32	Small	12.3	10.0	14.0	17.0	13.3	20.4
# of layers = 36	Small	12.3	9.9	14.1	17.0	13.3	20.3

9.7. Summary

This chapter analysed the thermal performance of the DRW integrated in a dummy CubeSat model to answer the Main research question, *"What is the effect of an external radiator using HiPeR to the temperature progression of a CubeSat over the course of a polar orbit?"*. The design from Chapter 8 is translated into a numerical model in ESATAN-TMS-2019. The total internal heat generated is 20 W during day time and halved to 10 W during the eclipse. The CubeSat is in a polar orbit and Nadir pointing with the rotating solar arrays always perpendicular to the Sun. The thermal performance is analysed for two cases: with and without the DRW with the same boundary conditions. The results are presented in Figure 9.5. The temperature of the dummy payloads decreased from around 85°C to around 20°C for the model with the DRW. This decrease in temperature is significant and provides an answer for Main research question that the effect of adding an external radiator decreases the overall temperature progression by a constant 68°C of a CubeSat over the orbit.

To model the design, various assumptions on the model parameters were made. These model parameters are varied in order to analyse the influence on the thermal performance of the CubeSat system with DRW. The results from this sensitivity analysis are summarised in Table 9.9.

This detailed model is verified in Chapter 10 with a reduced numerical model using different thermal modelling software to prove that the detailed model is suitable for analysing the thermal performance of the DRW.

10

System model verification

In the previous chapter the performance of the DRW integrated in a satellite system was analysed with a numerical model. To verify this detailed and complex numerical model using ESATAN-TMS-2019, a reduced numerical model is developed for this thesis. The reduced model consists of a reduced number of nodes for simplification. Each node in the reduced model represents an element in the model from Chapter 9. The goal is to replicate the results found in Subsection 9.4.5 to prove that the detailed model is suitable for analysing the thermal performance of the DRW.

The first step of the verification is to identify all the nodes and the radiative and linear conductive links. This is covered in Section 10.1. Section 10.2 explains the second step for the verification. In the second step, the view factors are calculated for each of the radiative surfaces. These view factors are converted into Gebhart factor to take the reflections of the surfaces into account in Section 10.3. Then equations for each of the conductive nodes are set up. For this thesis, the resulting system of equations is not solved analytically, but numerically. Therefore, thermal modelling software is used. Since ESATAN-TMS-2019 is already used for the main model, this reduced model is solved with ThermXL. Finally, the results are presented in Section 10.4. This chapter is summarised in Section 10.5.

10.1. Nodes and thermal links

The first step is to define the nodes and the thermal links. The detailed numerical model consists of various geometries as explained in Table 9.1. Each geometry is represented by one node, except the DRW. The DRW is represented as one node for each part, since the temperature gradient is large over its surface and this geometry is the most important. Even though the solar arrays are on opposite sides of the CubeSat, they are combined in one node. From the main model it is clear that both sides have almost equal temperatures. In addition, the solar arrays mostly radiate to space and only a partially to the CubeSat body and DRW. The stack of PCBs modelled as one surface with one node for simplicity. The two payloads are modelled as two surface, like in the detailed model, but represented as one node each for the reduced model. The payloads are connected with a thermal link to the DRW. The nodal network with the conductive and radiative thermal links is presented in Figure 10.1.

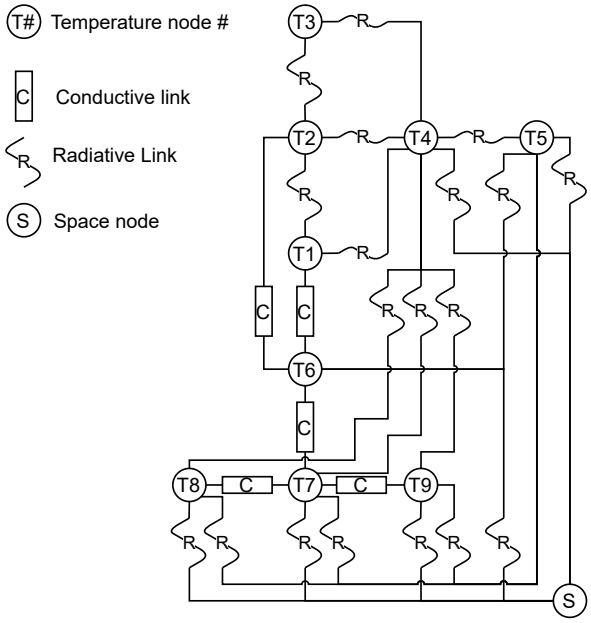

Figure 10.1: Nodal network of the reduced model. The heat source connections are not shown for clarity.

10.2. Calculating the view factors

The second step is calculating the view factors for the reduced numerical model. Normally view factors are calculated from surface to surface, however, each node has multiple surfaces. This can lead to seemingly incorrect view factor relations. This is factored in by keeping track of which side of the node the view factor is calculated to and from. ESATAN-TMS-2019 calculates these with a method called ray-tracing. This method is based on randomly firing rays and recording which of these hit the other surfaces. To calculate the view factors for the reduced model, mathematical relations are used from [11]. These mathematical relations are presented in Appendix B.

The model can be split into two cavities: the inside of the CubeSat body and the outside of the CubeSat body. There is no radiative link between the inside of the CubeSat and the surface of the CubeSat, there are only conductive links. This means that there is no radiative heat transfer from one to the other cavity. This is helpful because the two cavities can be analysed separately for the calculations of the view factors. The payloads and PCBs are all directly opposed rectangles. Using Equation B.1 the view factors for the payloads to each other and the PCB can be determined. The results are presented in Table 10.1. The view factors of the second cavity are calculated for the radiative thermal links from Figure 10.1.

Table 10.1: The view factors for the payloads, PCB and the inside of the CubeSat body.

Geometry name	Payload 1	Payload 2	PCB	CubeSat body
Payload 1	x	0.2		0.8
Payload 2	0.2	x	2.0	0.6
PCB		2.0	x	0.8
CubeSat body	0.8	0.6	0.8	x

10.3. Gebhart factors

These view factors are converted into Gebhart factor to take the reflections of the surfaces into account. Only a fraction of the energy that radiates on a surface is absorbed, the rest is transmitted or reflected. For opaque surfaces, no energy is transmitted, so most is reflected. This reflected energy can also bounce off to the other surfaces of the satellite, thus increasing the heat fluxes on these surfaces. This effect is especially large with surfaces with low emissivity. This reduced model takes this factor in account. This is included in the Gebhart factor and explained in further detail in Appendix B. The added reflections result in more radiative links. Due to the increase in radiative links for taking the Gebhart factors into account, only the Gebhart factors which are higher than 1% are used in the reduced model. Otherwise the reduced model becomes too complex and ignores the purpose of the reduced model.

10.4. Results for the verification model

For the reduced model it is not possible to solve it cyclically, solving it for the steady state is possible. Therefore, the steady state solution is found for the model described in Chapter 9. This is done for the point on the orbit where it crosses the equator on the sunlit side of Earth. The results for Figure 9.5 show that the steady state solution is not reached because the curve keeps changing. Therefore, it is expected that temperatures of the steady state solution for the full model is larger than from the results obtained in Chapter 9. The solution for the steady state for the model made in ESATAN-TMS-2019 is presented in Section 10.4.

From the view factors and Gebhart factors the heat load boundary conditions for the Sun radiation, Earth Albedo and Earth IR can be determined. These can be found in the centre part of Table 10.2 and are the boundary conditions for the reduced model. The two most right columns in Table 10.2 show the temperature results for the reduced model and the detailed model.

Table 10.3 is the summary of results of all heat flows into, inside and from the DRW for the detailed and the reduced models. This provides an insight into the differences between the models and to see if the detailed model is performing as expected. The blue cells represent the heat flow from the boundary conditions from the heat received the Albedo and Earth IR. The green cells represent the heat flows entering the elements. Orange cells represent the heat flows leaving the elements. The table is read with on the rows the parts of the DRW which receives or gives heat from or to the element on the column. As expected from the energy balance, the sum of the heat generated, entering and leaving an element is zero. This is shown in the last column. To present more insight in the differences, the percentage of the reduced model with respect to the detailed model is taken and presented in Table 10.4. The cells of the heat flows that show only a small difference are marked in green. A difference between 10% and 20% is marked in orange. Large differences are more than 20% and shown in red.

There are only a few small differences regarding the temperature in Table 10.2: the temperatures of the CubeSat body, the PCBs and the larger temperature gradient in the reduced model.

The temperature of the base part of the DRW is higher in the reduced model in comparison to the detailed model. The DRW is composed of multiple layers with on one side the heat applied from the interface. This results in a temperature gradient over the layers of the DRW. This temperature gradient is not represented in the results from Table 10.2 because the values presented are the averages of the whole part. This is especially apparent in the base part of the DRW. In the reduced model, all the layers are compressed into one node. The conductive heat flow is higher when the temperature gradient is high. In both models, the heat flow entering the base part from the interface is almost the same as shown in Table 10.3. The layers close to the interface in the detailed model, have high temperatures, thus in those layers the heat flow to the flap part is high. The layers further away from the interface have lower temperatures thus the heat flow to the flap part is lower. For the reduced model, the whole base part is represented as one node. To compensate for the high temperature in lower layers, the temperature of the base part node in the reduced model is higher than the average temperature of the detailed model.

The heat flows from Table 10.3 and Table 10.4 within the DRW are very similar to each other, except some boundary conditions and radiative links to the other CubeSat surfaces. The percentage difference of the heat flows between the detailed and reduced models are very high. But because the absolute values for the heat flows for the solar arrays and CubeSat body are small, the influence on the temperatures are small too.

Table 10.2: Overview of the boundary conditions for the reduced model with the temperature comparison between the detailed and reduced model. Space is a boundary condition with a constant temperature.

	Boundary conditions				Steady state temperature results	
Parts of the DRW	Sun radiation power [W]	Earth Albedo power [W]	Earth IR power [W]	Internal power [W]	Reduced model [°C]	Detailed model [°C]
Solar arrays	214.2	11.93	33.03		90.9	80.9
PCBs				10	80.7	47.5
CubeSat body	2.52	1.28	3.20		-7.2	1.20
Payload 1				10	32.9	37.0
Payload 2				10	32.9	37.0
Interface					32.7	35.3
DRW base		0.21	0.57		30.2	21.5
DRW flap		0.41	1.14		11.2	12.2
DRW left		0.41	1.14		4.9	8.4
DRW right		0.41	1.14		4.9	7.8
Space					-270.0	-270

Table 10.3: The differences in the heat flows into and from the parts of the DRW. Green is heat flow going into the element from other elements, blue is heat flow from boundary conditions and yellow is from heat flow leaving the element.

	DRW part	Interface	Base	Flap	Left	Right	Space	Solar arrays	CubeSat body	Net heat flow
Detailed model	Base	14.33	0.753	-12.04			-3.399	0.356		0.00
	Flap		12.04	1.25	-3.965	-4.029	-5.473	0.196	-0.017	0.00
	Left			3.965	1.332		-5.637	0.344	-0.005	0.00
	Right			4.029		1.319	-5.684	0.342	-0.007	0.00
Reduced model	Base	14.4	0.776	-11.53			-3.91	0.26		0.00
	Flap		11.53	1.552	-3.79	-3.79	-5.43	0.06	-0.13	0.00
	Left			3.79	1.552		-5.37	0.05	-0.02	0.00
	Right			3.79		1.552	-5.37	0.05	-0.02	0.00

Table 10.4: The percentage difference between the heat flows in the detailed and reduced model in Table 10.3. Green is a difference smaller than 10%, yellow between 10% and 20% and red is larger than 20%.

DRW part	Interface	Base	Flap	Left	Right	Space	Solar arrays	CubeSat body
Base	0%	3%	-4%			15%	-27%	
Flap		-4%	24%	-4%	-6%	-1%	-69%	665%
Left			-4%	17%		-5%	-85%	300%
Right			-6%		18%	-6%	-85%	186%

10.5. System verification summary

The temperatures and heat flows of the payloads and the DRW are very similar for the detailed and the reduced models. The higher temperature gradient in the reduced model is caused by the nodalisation of all the layers in only a few nodes. By verification of the detailed model by the reduced model, the detailed model proves suitable for analysing the thermal performance of the DRW.

This chapter verified the thermal performance of the DRW integrated in a CubeSat model by using a reduced model. A second method to verify the model presented in Chapter 9 is by testing using a prototype. This is performed in Chapter 7.

11

System model validation

This chapter will validate the numerical models from Chapter 5 and Chapter 9 with various methods. The most notable method to validate a numerical model is to build a prototype and test that in the same environment as the numerical model. However, due to external factors and influences, this was found not to be responsible and possible. Therefore, the following methods are used.

The numerical model is generated by and calculated with the thermal modelling tool ESATAN-TMS-2019. This tool is a black box for the user, and, therefore, does not allow for much validation. However, the results for the analyses generated with the tool in Subsection 9.4.3, Subsection 9.4.4 and the sensitivity analyses in Section 9.5 can be used for this validation process.

11.1. Requirement validation

This section takes the requirements defined in Section 2.2 and analyses its compliance. The requirement compliance matrix is presented in Table 11.1. For each requirement it is indicated whether the requirement is compliant and a value and reasoning is presented. Unfortunately, some requirements were not able to be tested due to unavailable test equipment. Other requirements are top-level requirements for the CubeSat system and independent from the DRW.

Table 11.1: Requirement compliance matrix.

Requirement	Compliant	Value and reasoning
DRW-Per1	Yes (Chapter 5)	Average of 12 W of heat dissipated from the payloads to space via the DRW.
DRW-Per2	Yes (Chapter 4)	Total radiating area is 0.04 m^2.
DRW-Per3	Yes (Chapter 4)	Bottom side.
DRW-Dpl1	Yes (Chapter 4)	By design and prototype the radiator is able to deploy using the tape spring hinges.
DRW-Per4	Yes (Chapter 7)	Prototype is 63 g.
DRW-Sto1	Yes on outside (Chapter 4)	Installed on the outside and folded over the outside, limits the used internal volume of the CubeSat to the interface and the thermal link.
DRW-Pod1	Yes	Thin laminate which is folded close to the outside walls. Does not overlap with the rails.
DRW-Pod1-Sto2	Yes	Thin laminate and see DRW-Pod1-Sto3.
DRW-Pod1-Sto3	Yes	The prototype of the DRW when folded around the dummy CubeSat, extents 5 mm of the bottom side and 3 mm of the sides.
DRW-Pod1-Sto4	Yes	The radiator is folded over the bottom of the CubeSat, while leaving the long edges for the rails free.
DRW-Dpl1-Sto5	Yes (Chapter 4)	The radiator has parts which are not adhered to allow for a small bending radius.
DRW-Dpl1-Dtc1	Depends	This depends on the HDRS.
DRW-Dpl1-Dtc2	Partial no (Chapter 4)	The tape spring hinge allows for passive deployment. However, an active HDRS may still be required to secure it during storage.
DRW-Dpl1-Ddc1	Yes	Installed at the opposite side of the deployable solar arrays, no shadow cast on the solar arrays.
DRW-Dpl1-Ddc2	Not tested	-
DRW-Dpl1-Ddc3	Not tested	-
DRW-CSc1	Yes	The base part of the DRW allows for a large and flexible location of the interface.
DRW-CSc2	CubeSat top-level requirement	-
DRW-CSc3	No (Subsection 9.5.6)	The temperature drops to -60°C when there is no internal power. To counter this something to disconnect the thermal link or heaters are required. However, typically survival heaters are required for CubeSats to prevent low temperatures [24].

11.2. Precision and repeatability

There are multiple steps taken to create and run the numerical model. Each of these must be repeatable for the whole to be repeatable. Steps that have random components can be irrepeatable. The creation of the model is repeatable since it is a set command lines that define all the geometries. For ESATAN-TMS-2019 there is one part that has a stochastic calculation step and another one that may cause the system to be irrepeatable.

The first step that is random, is the determination of the view factors with a Monte-Carlo ray tracing algorithm. A large enough number of rays are shot and traced from each of the surfaces of the geometry. The true view factors can calculated with mathematical relations as presented in Appendix B. This ray tracing will try to approximate these values with in a random manner. With infinite number of rays, these approximations are the same as the true values. With this finite amount of rays, there will be a deviation and, because the random behaviour, the deviation will be different each time.

The solution method is an iterative solver. With different initial conditions and different time steps, the final result may also be different. To test this, the model is run multiple times with the same and different initial conditions and different time steps.

The current time step is 0.1 second. When increasing to 1 second, the solver is unable to converge.

11.3. Curve fitting

ESATAN-TMS-2019 solves the system discretely with time steps of 0.1 seconds and all curves shows in this report have time steps of around 35 seconds with a period of 5674.5 seconds. It is possible that in between those time steps the curve is not smooth. However, this is not likely to happen. This is a system of interlinking conductive links with its constant boundary conditions. There are no sudden changes in either of these within the span of the time steps while their duration is shorter than the time step. Therefore, it is likely that the system does not behave in a non-smooth manner in between the time steps.

11.4. System survivability

The purpose of the radiator is to prevent overheating of the CubeSat. In some occasions the CubeSat can cool down too much. Low temperatures can damage the instruments and subsystems about satellites. The CubeSat could be cooled down too much, for example during times where some of the electronics are switch off or fall out of operation. A potential solution for this problem could be to temporarily disconnect the thermal link between the CubeSat instruments and the radiator. This reduces the heat flow from the CubeSat to the radiator to prevent heat loss.

Also, a CubeSat could be to cool down too much, because of the design of a radiator, instead a system with a too large radiator. Therefore, this has to be taken into account when designing the radiator for a CubeSat. From the sensitivity analysis in Subsection 9.5.6 the temperature will drop significant when there is no power for a longer duration.

12

Conclusion and recommendations

This final chapter concludes the findings made in this thesis report. The conclusions are detailed in Section 12.1. Recommendations for further research, analysis and testing are proposed in Section 12.2.

12.1. Conclusion

This section summarises the finding from this thesis report. First, the conclusions made during the design, analysing, prototyping and testing are presented in Subsection 12.1.1. Second, the research questions are answered in Subsection 12.1.2 using the DRW analysis results and the DRW integrated into a CubeSat system and the sensitivity analysis.

12.1.1. Conclusion design, analysis, prototyping and testing

The goal of this thesis was to provide a solution to the thermal problem of high-performing CubeSats. These CubeSat generate much heat due to a combination of increased power generation capabilities and miniaturisation. A deployable radiator is designed to solve this problem using HiPeR technology developed by Airbus Defence and Space Netherlands. This design is analysed, a prototype is produced and tested. The design is proposed after iteratively sizing the shape, dimensions, location of the interface and number of layers. The radiator allows for an efficient heat flow path between the payloads and space. This reduces the temperatures of the payloads. The design is a T-shaped laminate of 12 sheets of PG, and a top and bottom protective sheet of Kapton adhered with 3M966. This shape allows for easy folding over the outside of a CubeSat to minimise volume while being compliant with the P-POD requirements. Some parts of the PG sheets are not adhered, allowing for local bending with a small bending radius. A tape spring hinge provides support and the actuation for deployment.

This design is translated into a submodel. This is used for the sizing of the interface and dimension. The design is also analysed for the thermal performance of how much heat it is able to radiate. This is important because the DRW has to dissipate heat into space in order to be able to cool the CubeSat. The analysis shows that when 20 W is applied to the DRW, 20 W is radiated to space. The temperatures of the DRW are between -5°C (at the edges far from where the heat load is applied) and 45°C (near the location of where the heat load is applied). In conclusion, these temperatures and heat throughput are sufficient reason for further analysis to investigate how much the DRW is able to cool a CubeSat in orbit around Earth. For the verification by test, the submodel is adjusted to be representable for the test environment. The load cases for these analyses are detailed in Table 12.1.

A second case is proposed where the DRW is integrated into a CubeSat system to analyse the additional factors that influence the thermal performance. This case is a Nadir pointing CubeSat in a polar orbit at 500 km altitude. The load case, including boundary conditions, is detailed in Table 12.1. This analysis is performed for a CubeSat in a constant orbit around Earth using the thermal modelling software ESATAN-TMS-2019. From this analysis, around 40% of the 30 W heat produced inside the CubeSat is dissipated to space via the DRW. In conclusion, the DRW keeps payloads cool and ensures that the temperature of the payloads does not reach more than 23°C, a temperature at which a CubeSat is able to function properly.

Table 12.1: Overview of the load cases.

Case	Subcase	Chapter	Boundary condition location	Value	Eclipse
Submodel of DRW individually	Interface sizing	Section 5.3	Interface	30°C	n.a.
	Dimensions sizing	Section 5.3	Interface	30°C	n.a.
	DRW analysis	Section 5.4	Interface	20 W	n.a.
	Adapted for test	Chapter 7	Interface	5.1, 8.0 or 11.5 W	n.a.
System model with DRW integrated on a CubeSat	Nadir pointing CubeSat in polar orbit at 500 km altitude	Chapter 9	Payload 1	10 W	Halved
			Payload 2	10 W	Halved
			PCBs	10 W	Halved
			Outside surfaces	Sun	None
			Outside surfaces	Earth IR	Earth IR
			Outside surfaces	Albedo	None

To investigate whether the assumptions in the numerical model are correct, the sensitivity of the assumptions was analysed. This analysis has shown that changes in some variables have a considerable influence on the thermal performance of the DRW. The influence is measured using the temperatures of the payloads and the heat flow between the payloads and the DRW via a thermal link. Below are the assumptions that have a medium or high sensitivity on the performance as detailed in Table 9.9:

- Low thermal conductivity of the payloads and PCBs.
- Higher levels of generated power in the payloads.
- No reduction in the heat generated by the payloads and PCBs during an eclipse.
- Low thermal conductivity of the thermal link between the payloads and the DRW.
- A power case with no heat generated in the payloads and the PCBs.
- The angle of incidence of the Sun on the DRW.

Some assumptions are more influential than expected. Nevertheless, the assumptions had to be made to set up a workable numerical model and because of unknown CubeSat design. Assumptions that do not have a significant influence on the thermal performance of the DRW are a change in the number of layers of the PG sheets and the thermal conductivity of the PG sheets.

The verification of the numerical models was performed by testing a prototype in a vacuum oven instead of the desired vacuum chamber. The vacuum chamber was unavailable due to the COVID19 pandemic. The vacuum oven as an alternative test facility was not optimal. The air pressure of the vacuum oven is too high. The result is that the heat flow via radiation is not dominant over the heat conduction through the air. This does not simulate the space environment with dominating radiative heat flow sufficiently. Additionally, the adjusted submodel of the DRW was not accurate. The results of the verification by test are, therefore, inconclusive. However, the test did show that the achieved thermal conductivity of the PG sheets is the same as the theoretical value.

12.1.2. Answers research questions

Before answering the Main research question from Section 1.2: *"What is the effect of an external radiator using HiPeR to the temperature progression of a CubeSat over the course of a polar orbit?"*, the subquestions are answered first.

- RQ-1**:** What is the influence of different radiator shapes to the temperature gradient?

  Section 4.7 analyses the influence of the general shape for the radiator. Shapes with higher efficiency have temperatures closer to the boundary condition, and the temperature spread is uniform. It is found that for shapes with a larger surface area, the temperature gradient is smaller.

- RQ-2**:** How does the temperature gradient behave in the in-plane and out-of-plane directions of the surface of the radiator?

  When the boundary condition is applied in the centre of the radiator, the in-plane temperature gradient is smaller than when the boundary condition is applied to the edge of the radiator. This

is supported by the analysis from Section 4.7. The thermal analysis of the DRW in Section 5.4 shows that the temperature gradient is large in the in-plane direction and out-of-plane direction at the base part. The in-plane and out-of-plane temperature gradients reduce further away from the location of the boundary condition to almost zero near the edges of the side parts of the DRW.

- RQ-3**:** How does the temperature progression of the CubeSat behave over the course of a full orbit, with and without the radiator.

  This is answered in Section 9.4 with Figure 9.5. The temperature in sunlit conditions is increasing to its maximum until the CubeSat enters the eclipse phase. In the eclipse, the temperature drops to its minimum temperature. Over the orbit, it never reaches its steady-state temperature.

  The temperature trend for the CubeSat with and without the DRW is uniform. However, the difference is 68°C. Specifically, the CubeSat without DRW reaches a temperature that is 68°C higher than the CubeSat with the DRW. In conclusion, the DRW reduces the temperature of the CubeSat, over the entire orbit, so that the CubeSat does not overheat.

- RQ-4**:** What is the influence to the temperature progression of the CubeSat for different orbits?

  Over the course of the orbit of the Earth around the Sun, the orientation between the CubeSat and the Sun changes from the assumed position in the analysis. This is answered in the sensitivity analysis in Subsection 9.5.3. When the longitude of the ascending node changes to 45°, the temperature increases with around 7°C. When this angle increases to 90°C, the change increases to 15°C. At this point, the Sun is always perpendicular to the DRW. However, the solar arrays are parallel to the Sun's rays. Therefore, the CubeSat will probably rotate around its z-axis such that the solar arrays are perpendicular to the solar rays, thus, rotating the DRW out of the solar rays. Still, this increase in temperature is deemed significant.

- RQ-5**:** What is the influence of the thickness of the radiator to the temperature progression of the CubeSat?

  This is answered in the sensitivity analysis in Subsection 9.5.2 by varying the number of layers between 12 and 36 in steps of 6. The average heat flow to the DRW increased with up to 2%. The mass is increased by almost a factor of 3. Thus, it can be concluded that more than 12 layers does not increase the performance of the DRW significantly.

- Main research question**:** What is the effect of an external radiator using HiPeR to the temperature progression of a CubeSat over the course of a polar orbit?

  The effect of an external radiator to the temperature progression of a CubeSat over the course of a polar orbit is a reduction in the temperatures by a constant value. For a numerical model with 30 W heat load generated on the inside of a CubeSat, the radiator is able to dissipate 40% to space for a total of 12 W. The 30 W is distributed over two payloads and a stack of PCBs evenly. In the model, the payloads are directly connected to the DRW with a high conductive thermal link. The sensitivity analysis used for analysing the numerical models showed the limitations. In conclusion, the DRW is able to dissipate a significant amount of heat to space to prevent the CubeSat from overheating.

The DRW is able to radiate much heat to space. This ability to radiate heat efficiently allows for CubeSats to use more power, and thus heat generation, without the danger of overheating. This increase of tolerable heat generation allows more instruments on the CubeSat to operate simultaneously. Miniaturisation allows for smaller instruments, so more instruments are able to fit on the same CubeSat. The available heat generation and miniaturisation combined increases the economic and scientific value of CubeSat missions.

12.2. Recommendation

This thesis project designed, analysed the thermal performance, prototyped and tested a radiator to dissipate excessive heat for high-performance CubeSats. During this research, some elements came up, which require further research which could not be performed in this thesis project due to time and facility constraints. Recommendations are made for this further research in this section. The first points focus on the recommendations for the analysis and the second points focus on the prototype testing.

During the sensitivity analysis, it was found that the sensitivity of the conductivity of the thermal link between the DRW and the payloads is significant. Therefore, more research should be performed to investigate options for high thermal conductive means of transport between the payload and the DRW.

Additionally, more in-depth analysis of the influence of a changing orbit is required. Earth revolves around the Sun and thus changing the solar angle of incidence on the DRW and increasing the heat transfer.

This research assumed that the contact resistance between the PG or Kapton sheets and the adhesive are negligible. More research is needed on what these values are by testing.

A more optimal shape is a plus-shape. This has a larger surface area and thus larger heat radiation. For this thesis, this is not considered due to the fixed width of the PG sheets. PG sheets with a larger width would make plus-shaped radiators possible.

During the test, the influence of the air is significant. This caused the test to be not performed in an environment where heat flow via radiation is dominated as it is in orbit around Earth. The vacuum, where radiation is dominant, requires a vacuum chamber, and for this thesis project, this was not available. Therefore, it is recommended to test the prototype in a vacuum chamber in an environment where the heat flow via radiation is dominant.

To summarise the recommendations:

- Research the thermal resistance between the PG or Kapton sheets and the adhesive.
- Prototype the plus-shaped radiator with wider PG sheets if it exists.
- Test the prototype in a vacuum chamber where radiative heat transfer is dominant.
- Research potential thermal links for efficient heat transfer between the instruments of CubeSats and the radiator.
- Research the thermal performance of the DRW, integrated on a CubeSat, for multiple Earth revolutions taking changing orbits into account.

A

Test plan

This appendix consists of test plans for three tests. First, the test for the performance inside the vacuum chamber is described. Second, the vibration test is described and finally the test for the deployment is described. Not all tests were performed, but detailed here for completeness.

A.1. Test plan for Deployable Radiator Wing test for verifying the thermal performance

This test with a prototype of the DRW will verify the predictions of the thermal performance made by the mathematical model in Chapter 5 and Chapter 9.

A.1.1. Objective and assumptions

Ideally the test is performed in a vacuum chamber with a vacuum such as in space. This is because the heat flows from the DRW to the surroundings in space are dominated by radiation. Introducing air, introduces a second mode of transport, the heat flows via conduction. In a vacuum chamber radiation is dominant. However, a vacuum chamber was not available to test in. Instead, a vacuum oven is used. To compensate for the heat flow via conduction with the air, the numerical model is adjusted, see Section 5.6. The base part of the DRW is subjected to a heat flow by a heater element to simulate the heat from the payloads. This heat load is varied to investigate the performance for various power levels. The test is not able to simulate the conditions in space because the available test equipment does not allow for cooling and other heat sources to simulate the Sun, Albedo and Earth IR.

A.1.2. Test approach

The prototype of the DRW is as explained in Section 7.1. A schematic overview of the prototype is shown in Figure A.1. The prototype is placed on an elevated platform in the model of the vacuum chamber. The heater is connected to the power supply. The thermal couples are placed on the prototype with aluminium tape and then connected to the temperature measurement device. An overview of the locations of the thermocouples is shown in Table A.1. The temperature measurement device is connected to a computer to log all the temperatures. Then the power supply is set to a power level. The heater will heat the DRW to the equilibrium temperature. This could take a lot of time, therefore, it is assumed that the equilibrium temperature is reached when the temperature changes less than 0.05°C per minute. This process is repeated for a total of three heater power levels.

A.1.3. Success criteria

The test is a success when the radiator is able to dissipate 5 W with a maximum temperature of 50°C.

Table A.1: Locations of the thermocouples

Number	Part name	Position
0	Base	Top middle
1	Flap	Top middle
2	Left	Top middle
3	Right	Top middle
5	Vacuum oven	Ceiling
6	Vacuum oven	Free hanging
7	Vacuum oven	Floor
8	On heat cover plate	Bottom middle
9	Flap	Bottom middle
10	Left	Bottom middle
11	Right	Bottom middle

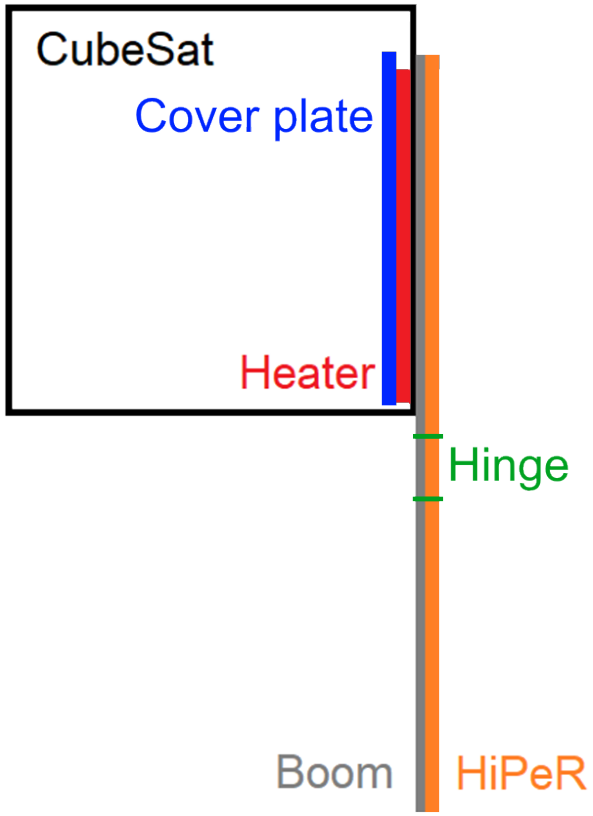

Figure A.1: Schematic overview of the prototype of the DRW including the aluminium dummy cube, heater and cover plate.

A.2. Test plan for vibration test

This test will investigate the reaction to vibrations.

A.2.1. Objective

The objective of the test is whether the system can survive the launch vibrations and to measure what the natural frequencies are.

A.2.2. Test approach

There are two kind of vibration test possible, the sinusoidal and the random vibration test. The sinusoidal test is a sweep of the frequencies between 5 and 140 Hz at 2 oct/min [13]. The acceleration experienced is shown in Table A.2 for the different frequencies. The random vibration test is performed for 2 minutes [13] with the data presented in Table A.3 which is visualised in Figure A.2. Each test must be performed on each of the three axes of the dummy CubeSat three times. The vibration table can only vibrate in 1 (or 2) directions. Therefore, for each of the vibration tests, three runs must be performed. Two runs are in the x-direction and y-direction of the CubeSat while mounted on the bottom side and one test is in the z-direction of the CubeSat while mounted on the open side. An additional sinusoidal test may be performed after the random vibration test to see if anything is damaged. The second sinusoidal test will be different from the first if there is any damage caused by the random vibration test. The natural frequency will change due to any damage.

The test is performed with the aluminium CubeSat dummy with the DRW on top. The DRW must be in stowed configuration. The heater, thermal strap and thermal wire cutter can be included, but are not necessary for the test.

The test stand used is the Vibration Exciter - Type 4809. This vibrator is able to deliver a g-force of 20 g to a mass of 170 g. This may not be enough. Lightweight vibration sensors are needed to get feedback from the vibrations of the model and the DRW.

A.2.3. Success criteria

It is expected to survive without any damage. Damages that are possible to occur are: delamination, tearing and plastic deformation. During the tests it is expected that the sides of the flap will vibrate because it does not have a high internal stiffness.

The measurements are collected by a camera or by looking at it. Also, the second sinusoidal vibration test could give insight into any damage when the natural frequency is different.

The test is successful when there is no visible deofrmation, visible tearing of the material, visible destruction of any of the parts and that the amplitude of the vibrating DRW laminate is too high. A high amplitude of the vibrating DRW laminate could cause damage to the DRW because it could be hitting the walls on the inside of the P-POD.

A.2.4. Test sequence

The test sequence is as follows:

1. Set-up test
2. Sinusoidal vibration test:
   (a) Mounting
   (b) x-direction
   (c) y-direction
   (d) Remount
   (e) z-direction

Table A.2: Sinusoidal vibration qualification test level [13].

Frequency [Hz]	Amplitude [g]
5-100	2.5
100-140	1.25

Table A.3: Random vibration qualification test level [13].

Frequency [Hz]	ASD level [g^2/Hz]
20	0.026
20-50	+6dB/oct
50-800	0.16
800-2000	-6dB/oct
2000	0.026
Overall	14.1 Grms

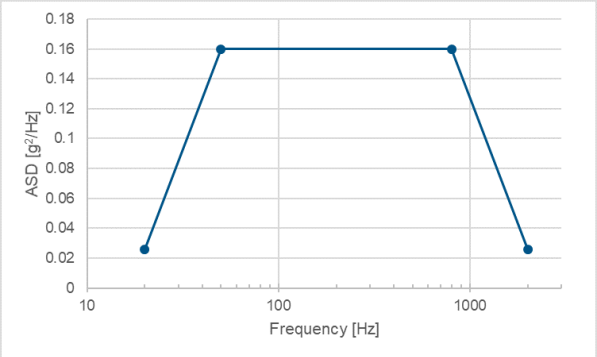

Figure A.2: Graphical representation of the ASD level for the random vibration

3. Random vibration test
   (a) Remount
   (b) x-direction
   (c) y-direction
   (d) Remount
   (e) z-direction
4. Repeat step 2 to check for damage
5. Clean-up

A.3. Test plan for deployment test

This test will investigate the behaviour of the deployment of the DRW.

A.3.1. Objective and assumptions

The objective is to see if the DRW deploys without damaging the structure and HiPeR laminate. Also the deployment may induce shocks and an increase in angular momentum. The first objective is to see whether the tape spring is able to deploy the DRW. The asymmetrical deployment will cause the CubeSat to spin. The second objective is to investigate the influence of this asymmetrical deployment. Additionally, the third objective is to investigate the intensity of the shock caused by the locking of the tape spring upon deployment. This locking is explained in more detail in Section 3.3.

A.3.2. Test approach

This test to check the first objective is a simple deployment test where the hold down wire is melted by a thermal wire cutter as part of the HDRS. This allows the DRW to unfold and deploy. This test involves the aluminium CubeSat dummy with the DRW on top. The DRW must be in stowed configuration, so it can be deployed during the test. The plastic wire must touch the thermal wire cutter. The heater and thermal strap can be included, but are not necessary for the test. Alternatively, instead of using a wire cutter and a HDRS, the DRW can also be folded around the aluminium dummy CubeSat and held down with a hand. This makes the process repeatable and simple.

The test sequence for objective 1 is as follows:

1. Set-up test
   (a) Camera
   (b) CubeSat with integrated HDRS and DRW
2. Connect hold-down wires to DRW and HDRS
3. Deploy
4. Remove leftover wires
5. Repeat from step 2 on-wards
6. Clean-up

The tests for objective two and three are more difficult. This requires a weighted CubeSat dummy with a representable mass moment of inertia and a balance table on which the whole system can rotate. These two objectives can be tested simultaneously. The system is attached to a rotating table with low friction to measure the induced rate of rotation onto the system. This test is not detailed further because it was not performed due to the COVID19 pandemic and the closing of the test facilities.

A.3.3. Success criteria

Not much can go wrong, just an inspection if any cracks form. The test is successful if there are no cracks after deploying it 10 times. One deployment test is performed successfully after the prototype is in a stored configuration of at least one week.

B

View factor equations

This appendix explains the equations used for calculating the view factors of various geometries.

The view factor between two opposing flat plates of equal size is governed by Equation B.1. Where X and Y are the fractions in Equation B.2 and Equation B.3, respectively [11]. The variables a, b and c are the width, length and the distance between the two plates as shown in Figure B.1.

$$F_{12} = \frac{2}{\pi XY}\left(\ln\left(\frac{(1+X^2)(1+Y^2)}{1+X^2+Y^2}\right)^{\frac{1}{2}} + X\sqrt{1+Y^2}\arctan\frac{X}{\sqrt{1+Y^2}} + Y\sqrt{1+X^2}\arctan\frac{Y}{\sqrt{1+X^2}} - X\arctan X - Y\arctan Y\right) \tag{B.1}$$

$$X = \frac{a}{c} \tag{B.2}$$

$$Y = \frac{b}{c} \tag{B.3}$$

The view factor between two rectangles with a common edge at $\Phi = 90°$ is governed by Equation B.4. Where N and L are the fractions in Equation B.5 and Equation B.6, respectively [11]. The variables a, b and c are the width of plate 2, width of plate 1 and the length of both plates, as shown in Figure B.2.

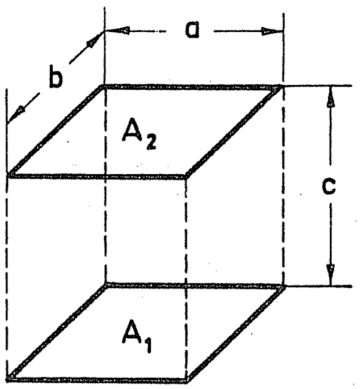

Figure B.1: Two parallel and directly opposed flat plates of same width and length [11].

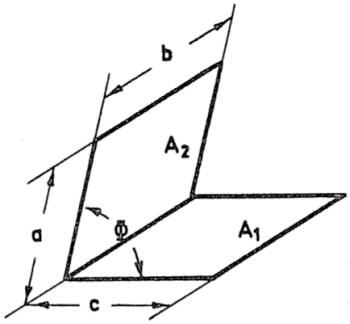

Figure B.2: Two rectangles with a common edge at 90°[11].

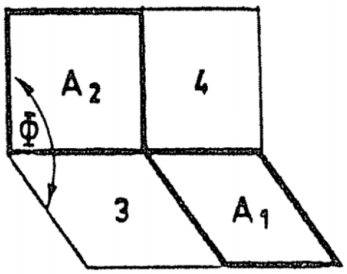

Figure B.3: Two plates crosswise with a common edge and included angle [11].

$$F_{12} = \frac{1}{\pi L}\left(L\arctan\left(\frac{1}{L}\right) + N\arctan\left(\frac{1}{N}\right) - \sqrt{N^2+L^2}\arctan\left(\frac{1}{\sqrt{N^2+L^2}}\right)\right.$$
$$\left. + \frac{1}{4}\ln\left(\left(\frac{(1+L^2)(1+N^2)}{1+N^2+L^2}\right)\left(\frac{L^2(1+N^2+L^2)}{(1+L^2)(N^2+L^2)}\right)^{L^2}\left(\frac{N^2(1+N^2+L^2)}{(1+N^2)(N^2+L^2)}\right)^{N^2}\right)\right) \tag{B.4}$$

$$N = \frac{a}{b} \tag{B.5}$$

$$L = \frac{c}{b} \tag{B.6}$$

The view factor for plates crosswise with a common edge and included angle is calculated by area fractions. To obtain the view factors required to solve this for $\Phi = 90°$, the view factors for each of the four areas needs to be calculated with Equation B.4 and substituted into Equation B.7 [11]. This is visualised in Figure B.3.

$$F_{12} = \frac{1}{2A_1}\left(A_{(1,3)}F_{(1,3)(2,4)} - A_1F_{14} - A_3F_{32}\right) \tag{B.7}$$

The view factor for two plates with different areas with a common edge and included angle is calculated with the area fraction Equation B.8. To obtain the view factors required to solve this for $\Phi = 90°$, the view factors for each of the six areas needs to be calculated with Equation B.4. This is visualised in Figure B.4.

$$F_{3(2,4,6)} = \frac{1}{2A_3}\left(A_{(1,3)}F_{(1,3)(2,4)} + A_{(3,5)}F_{(3,5)(4,6)} - A_1F_{12} - A_5F_{56}\right) \tag{B.8}$$

To account for the reflection of the surfaces onto all other surfaces, the Gebhart factor is used [12]. To calculate this, all view factors are corrected for the emissivity and the amount of radiation reflected to every other surface, see Equation B.9. All Gebhart factors originating from the same surface should add up to 1 from the principle of conservation of energy as similar to the view factors, see Equation B.10.

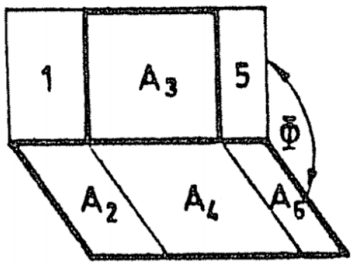

Figure B.4: Two plates with different areas with a common edge and included angle [11].

$$B_{ij} = F_{ij}\epsilon_j + \sum_{k=1}^{n}(1-\epsilon_k)F_{ik}B_{kj} \tag{B.9}$$

$$\sum_{j=1}^{n} B_{ij} = 1 \tag{B.10}$$

C

Model figures

This appendix provides the figures of the model in the ESATAN-TMS-2019 geometric user interface. The colours shown in the figures in this appendix correspond to the geometries in Table C.1.

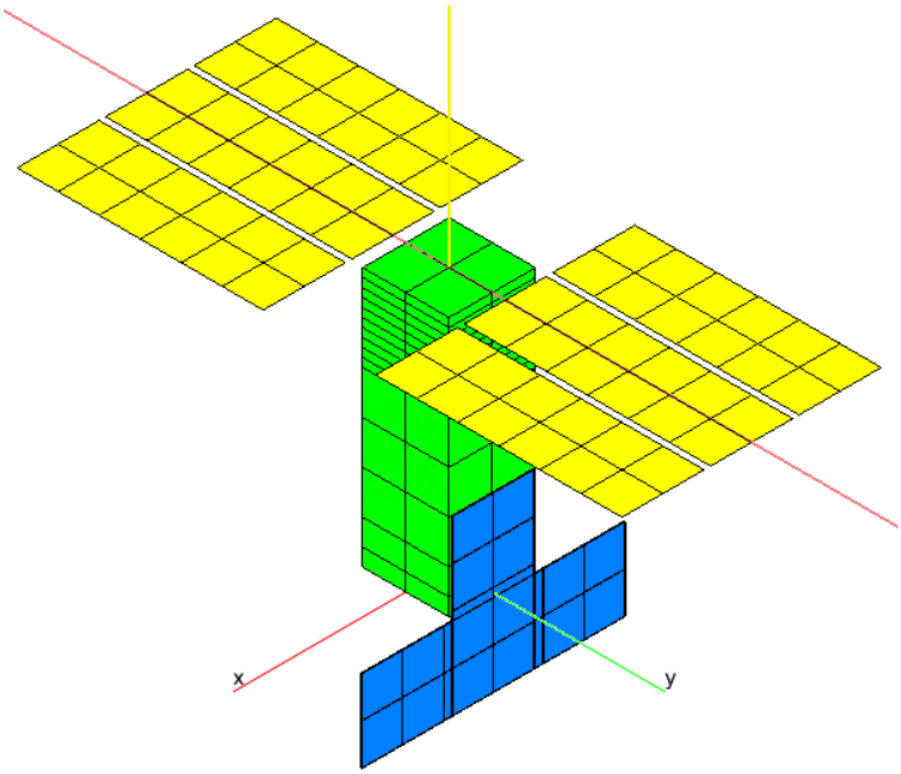

Figure C.1: Full model isometric view.

Table C.1: Colour coding

Colour	Geometry
Blue cyan	DRW
Blue	Payload 1 and 2
Green	CubeSat body
Purple	Stack of PCBs
Yellow	Solar arrays

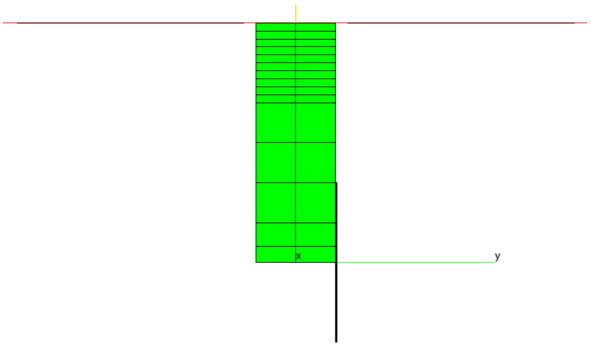

Figure C.2: Full model view form the $+x$-direction.

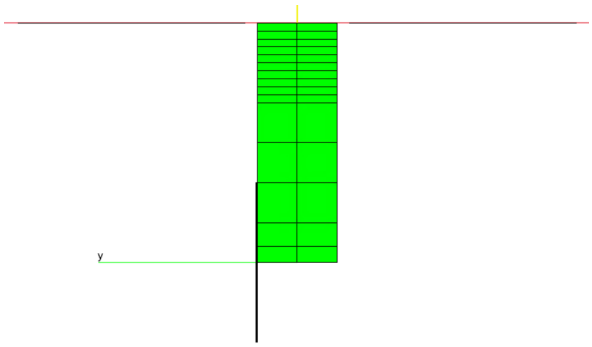

Figure C.3: Full model view form the $-x$-direction.

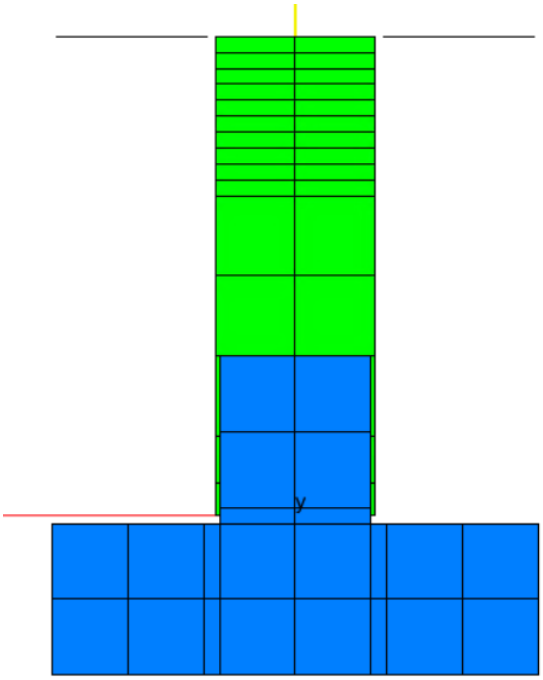

Figure C.4: Full model view form the $+y$-direction.

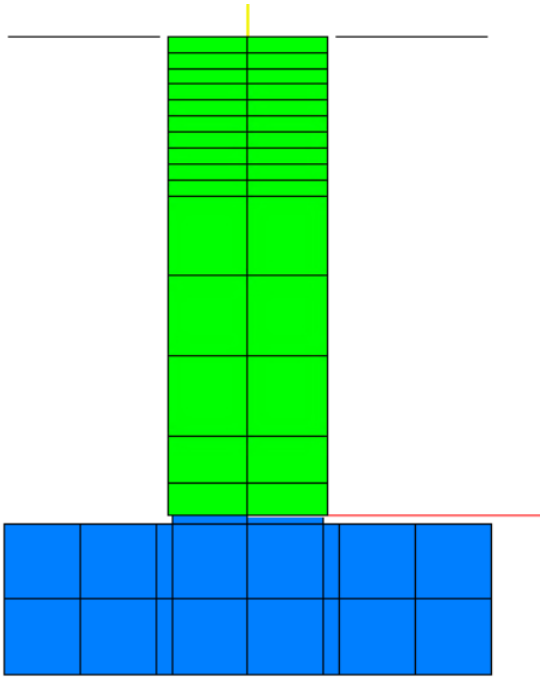

Figure C.5: Full model view form the $-y$-direction.

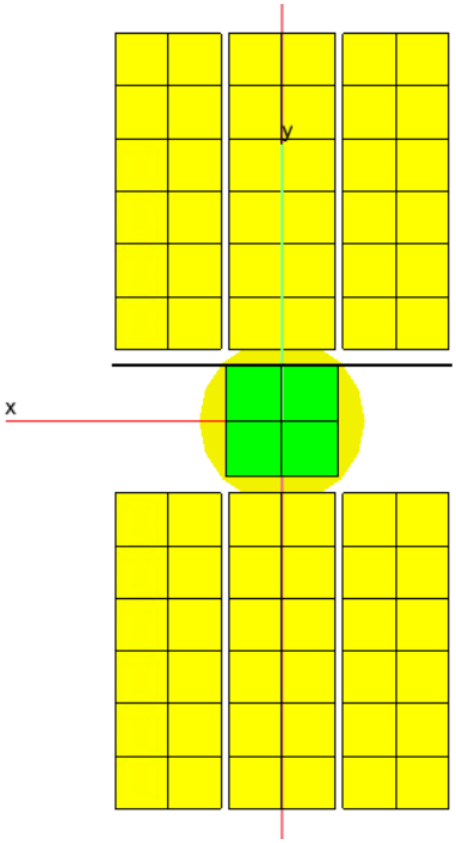

Figure C.6: Full model view form the $-z$-direction.

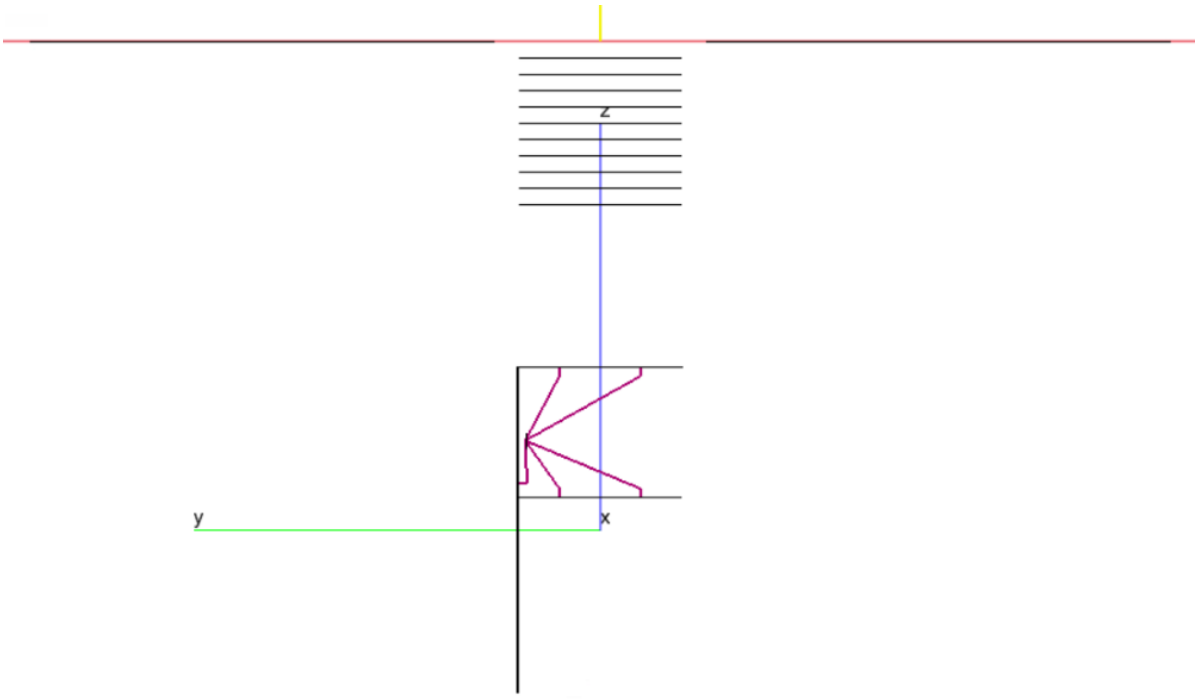

Figure C.7: Inside model view form the $-x$-direction (hidden CubeSat body geometry).

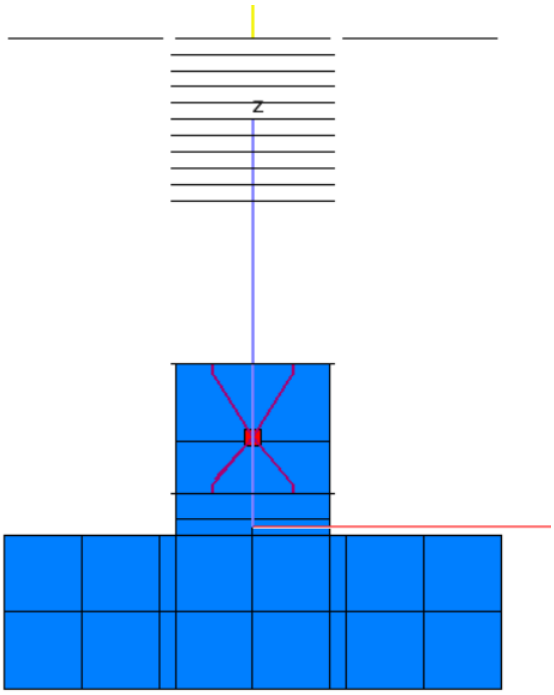

Figure C.8: Full model view form the $-y$-direction (hidden CubeSat body geometry).

D

Model explanation

This appendix will explain how the model is made in ESATAN-TMS-2019. It starts in Section D.1 with how the input files are made using python. Then, in Section D.2 how those files are interpreted inside the ESATAN-TMS-2019 application environment. And finally how ESATAN-TMS-2019 solves the model in Section D.3.

D.1. Construct input files

ESATAN-TMS-2019 requires three inputs to calculate the temperatures and heat flows. First, the geometry must be defined in the geometric file, then the environment and radiative case are defined in the radiative file. Finally, the definition of the analysis file is defined that combines the geometric and radiative files with the boundary conditions in the thermal file. This is performed using a python script. This subsection describes the process of creating the model. The actual parameters used, are described in Chapter 4 and Chapter 8.

The input files consists of many parameters and functions. A lot of the parameters and functions have standard templates where only a few options vary and are repetitive. This allows for the use of a program that generates these input files. In addition, it allows for changing the model parameters easily. To construct these input files the programming language Python is used. A main file is made where all functions are called into that to construct the input files. These functions use input data of the model parameters from a file with the model parameters stored in dictionaries.

In the geometric file, all data and parameters are stored that define the model geometrically and physically. This includes the defined geometries from Subsection 9.2.1, the thermo-optical and material properties, the definition of the Sun-pointing solar arrays, the conductive interfaces between adjacent geometries and the conductors between the payloads via the heat switch to the DRW.

The radiative file contains the information to run the radiative analysis. This includes the radiative case definition, the parameters used for ray-tracing, the orbit characteristics and the definition of the environment.

The thermal file contains the information to run the thermal analysis. This includes the analysis case definition. This file also defines and sets the boundary conditions. Furthermore, the commands are given on how to solve the analysis case and to solve the analysis case.

D.2. ESATAN-TMS-2019 environment

The Graphical User Interface (GUI) of the ESATAN-TMS-2019 environment lets the user interact with the model, define geometries, boundary conditions, conductors, conductive interfaces and parameters. However, instead of defining everything in the GUI this is defined in text by the input files described in Section D.1. These files still needs to be imported into the GUI and run with the GUI or run via the so-called shell script. After importing the three input files (geometric, radiative and thermal) into ESATAN-TMS-2019, the radiative case is run to determine the view factors over the orbit. This is explained in Subsection D.2.1. Then, the conductive links are calculated, see Subsection D.2.2, and written into the analysis file, see Subsection D.2.3. The process described above can be circumvented by running a shell script that does it automatically.

D.2.1. Calculate view factors

The view factors are calculated by ESATAN-TMS-2019 by ray-tracing. This means that for each surface node, called a face, a large amount of rays are fired. Each ray is fired from the middle of the node in a random direction facing away from the node. The path is analysed and which surface the ray is hit by, is stored. The result is a distribution of the faces that are hit. The view factors of each face to other faces can be derived from this distribution. For ESATAN-TMS-2019 the default number of rays are 10,000. This will be used in the system analysis, for the DRW stand-alone analysis, a lower number could be used when using a lot of nodes because there is no complex geometry around it.

D.2.2. Calculate conductive links

There are multiple kinds of conductive links, but this model uses only the linear and radiative conductive links. The linear conductive links follow the conductive heat transfer model from Equation 4.2. These links are calculated for the nodes within one geometric shape and between geometric shapes when a conductive interface is defined. The radiative conductive links follow the radiative heat transfer model from Equation 4.1. The view factors are used for the radiative conductive links.

D.2.3. Construct analysis file

The analysis file is a system of equations which is solved by ESATAN-TMS-2019. How it is solved, is explained in Section D.3. This file combines information of the definitions of all nodes with its properties, the conductive links between the nodes, the boundary conditions, time and temperature dependent variables and the solving method.

D.3. Solve for the steady-state solution

The parameters solving the analysis file are defined in the thermal file, see Section D.1. Instead of importing all input files into the GUI and running the solver from the GUI of ESATAN-TMS-2019, the solver can also be run from the terminal. This will speed up the process and no information is lost. These shell files calls functions that import and run the files into ESATAN-TMS-2019 directly. Finally, the results are exported and can be graphed and analysed.

E

Prototype and testing

This appendix shows more pictures of the prototype and the test.

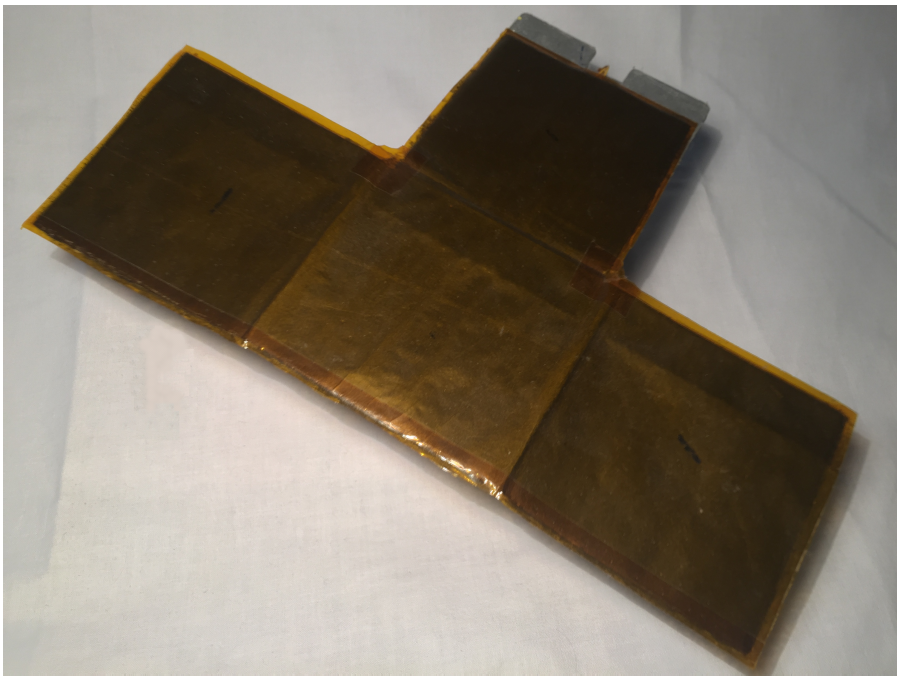

Figure E.1: Top view of the DRW prototype.

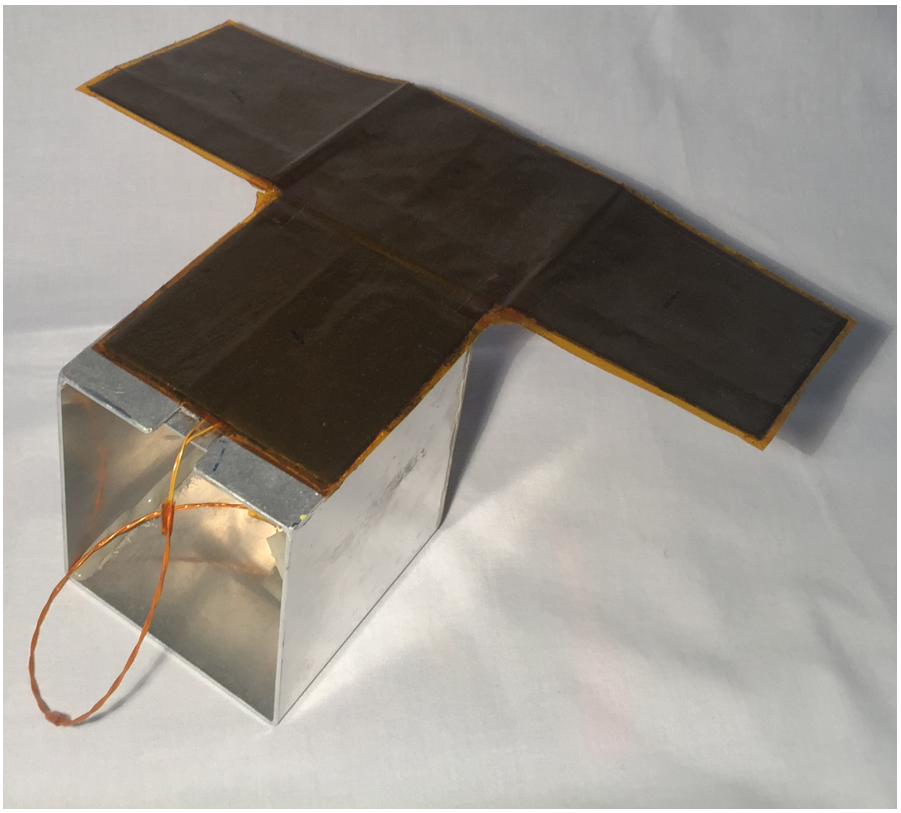

Figure E.2: Top view of the DRW prototype with view on the aluminium dummy. The wires of heater element are visible.

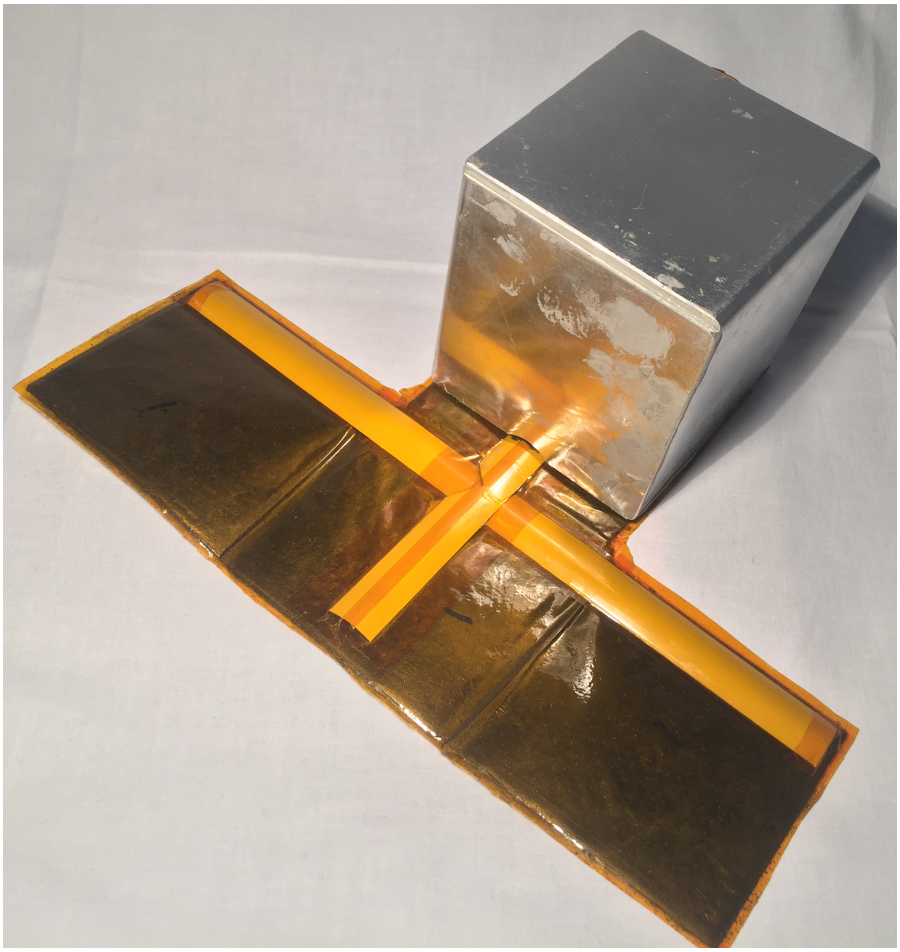

Figure E.3: Bottom view of the DRW prototype with the tape spring visible.

Figure E.4: The DRW prototype in the test set-up inside the vacuum oven. The green white wires are the thermocouples.

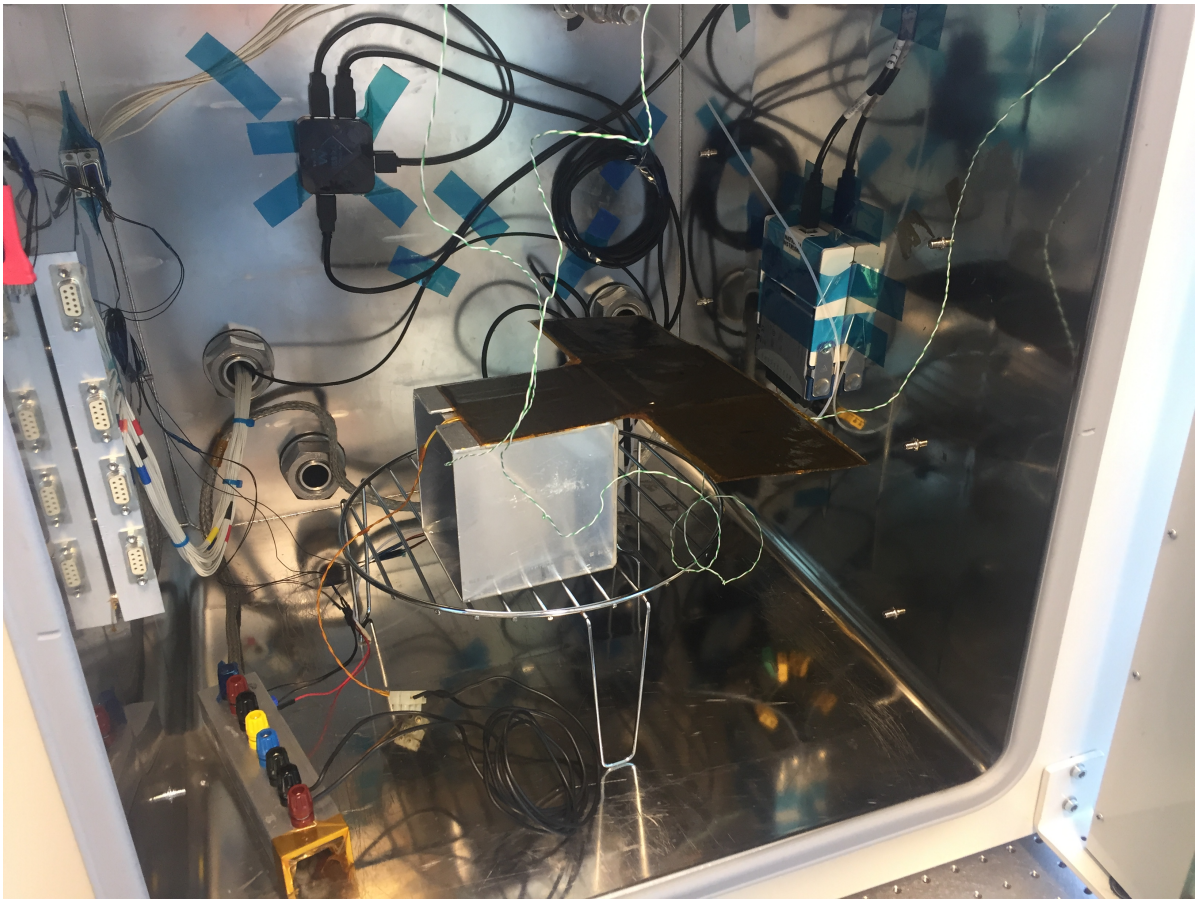

Figure E.5: The DRW prototype in the test set-up inside the vacuum oven. The prototype sits on top of a platform such that the prototype is situated in the middle of the vacuum oven. The green white wires are the thermocouples.

Bibliography

[1] Kevin R. Anderson, Matthew Devost, Watit Pakdee, and Niveditha Krishnamoorthy. Star ccm+ cfd simulations of enhanced heat transfer in high-power density electronics using forced air heat exchanger and pumped fluid loop cold plate fabricated from high thermal conductivity materials. *Journal of Electronics Cooling and Thermal Control*, 3(04):144, 2013.

[2] Scott Sterling Arnold, Ryan Nuzzaci, and Ann Gordon-Ross. Energy budgeting for cubesats with an integrated fpga. In *2012 IEEE Aerospace Conference*, pages 1–14. IEEE, 2012.

[3] PW Atkins. Thermodynamic principles. *AccessScience@ McGraw-Hill, http://www. accessscience. com, DOI*, 10:1097–8542, 2002.

[4] W. J. Blackwell, S. Braun, B. Zavodsky, C. Velden, T. Greenwald, D. Herndon, R. Bennartz, M. DeMaria, G. Chirokova, R. Atlas, J. Dunion, F. Marks, R. Rogers, H. Christophersen, and B. Annane. Overview of the NASA TROPICS CubeSat constellation mission. In Thomas S. Pagano and Charles D. Norton, editors, *CubeSats and NanoSats for Remote Sensing II*, volume 10769, pages 64 – 73. International Society for Optics and Photonics, SPIE, 2018. doi: 10.1117/12.2320333. URL https://doi.org/10.1117/12.2320333.

[5] H.S.B. Brouwer. Performance characterization of water heat pipes and their application in cubesats. Master's thesis, Delft University of Technology, 2016.

[6] Hugo Brouwer, Zeger de Groot, Jian Guo, and Henk Jan van Gerner. Solving the thermal challenge in power-dense cubesats with water heat pipes. In *in 31st Annual AIAAUSU Conference on Small Satellites*, 2017.

[7] Elizabeth Buchen. Spaceworks' 2014 nano/microsatellite market assessment. 2014.

[8] Craig Clark. Huge power demand... itsy-bitsy satellite: Solving the cubesat power paradox. In *in 24th Annual AIAAUSU Conference on Small Satellites*, 2010.

[9] MAP Space Coatings. Thermal conductivity. https://www.map-coatings.com/en/boutique/configuration-selector/p/1.php. [Online; accessed 20-01-2021].

[10] Florence Dewalque, Pierre Rochus, and Olivier Brüls. Importance of structural damping in the dynamic analysis of compliant deployable structures. *Acta Astronautica*, 111:323–333, 2015.

[11] *Spacecraft Thermal Control Design Data Handbook, Volume 1*. ESA PSS-03-108, Issue 1, Noordwijk, the Netherlands, November 1989.

[12] B. Gebhart. *Heat Transfer*. McGraw-Hill, 1961. URL https://books.google.nl/books?id=Zv5QAAAAMAAJ.

[13] NASA GSFC. General environmental verification standard (gevs). Technical report, GSFC-STD-7000A, 2013.

[14] ISISpace. Cubesat solar panels. https://www.isispace.nl/product/isis-cubesat-solar-panels/. [Online; accessed 14-09-2020].

[15] ISISpace. Cubesat deployers. https://www.isispace.nl/wp-content/uploads/2016/02/CubeSat-deployers-Brochure-web-compressed.pdf, 2016. [Online; accessed 23-08-2020].

[16] Herbert J. Kramer. UKube-1 (United Kingdom Universal Bus Experiment 1). https://earth.esa.int/web/eoportal/satellite-missions/u/ukube-1, 2012. [Online; accessed 01-11-2020].

[17] Herbert J. Kramer. Cubesat concept and the provision of deployer services. https://directory.eoportal.org/web/eoportal/satellite-missions/c-missions/cubesat-concept, 2014. [Online; accessed 10-10-2020].

[18] Wiley J Larson and James R Wertz. Space mission analysis and design. *Space*, 5(14):110, 1999.

[19] Wilfried Ley, Klaus Wittmann, and Willi Hallmann. *Handbook of space technology*, volume 22. John Wiley & Sons, 2009.

[20] John Lohan, Pekka Tiilikka, Peter Rodgers, C Fager, and Jukka Rantala. Effect of pcb thermal conductivity on the operating temperature of an so- 8 package in a natural convection environment: Experimental measurement versus numerical prediction. In *International Workshop on Thermal Investigations of ICs and Microstructures (THERMINIC)*. Citeseer, 1999.

[21] Alexander Maas. Development of pyrolytic graphite applications in spacecraft thermal control systems-Airbus DS NL HiPeR product suite development status. In *47th International Conference on Environmental Systems*, 2017.

[22] Arash Mehrparvar, D Pignatelli, J Carnahan, R Munakat, W Lan, A Toorian, A Hutputanasin, and S Lee. Cubesat design specification rev. 13. *The CubeSat Program, Cal Poly San Luis Obispo, US*, 1(2), 2014.

[23] NASA. ALBus hopes to increase power availability for cubesats. https://www.nasa.gov/feature/albus-hopes-to-increase-power-availability-for-cubesats, 2018. [Online; accessed 03-10-2019].

[24] Oleg Nizhnik. Cubesat amateur laser communicator with earth to moon orbit data link capability. 12 2014.

[25] Parasonic. Thermal management solutions. https://industrial.panasonic.com/cdbs/www-data/pdf/AYA0000/AYA0000COL24.pdf, 2019. [Online; accessed 03-10-2019].

[26] Elia Picault, Stephane Bourgeois, Bruno Cochelin, and Francois Guinot. On the folding and deployment of tape springs: A large displacements and large rotations rod model with highly flexible thin-walled cross-sections. In *53rd AIAA/ASME/ASCE/AHS/ASC Structures, Structural Dynamics and Materials Conference 20th AIAA/ASME/AHS Adaptive Structures Conference 14th AIAA*, page 1956, 2012.

[27] John R Samson. Implementation of a dependable multiprocessor cubesat. In *2011 Aerospace Conference*, pages 1–10. IEEE, 2011.

[28] John R Samson Jr and FL Clearwater. Dependable multiprocessor (dm) implementation for nanosatellite and cubesat applications. In *2010 Summer CubeSat Workshop Small Satellite Conference*. Citeseer, 09 2010.

[29] Fabio Santoni, Fabrizio Piergentili, Serena Donati, Massimo Perelli, Andrea Negri, and Michele Marino. An innovative deployable solar panel system for cubesats. *Acta Astronautica*, 95:210–217, 2014.

[30] Klaus Schilling. Perspectives for miniaturized, distributed, networked cooperating systems for space exploration. *Robotics and Autonomous Systems*, 90:118–124, 2017.

[31] K.A. Seffen and S. Pellegrino. Deployment dynamics of tape springs. *Proceedings of the Royal Society of London. Series A: Mathematical, Physical and Engineering Sciences*, 455(1983):1003–1048, 1999.

[32] Daniel Selva and David Krejci. A survey and assessment of the capabilities of cubesats for earth observation. *Acta Astronautica*, 74:50–68, 2012.

[33] Omer Soykasap, Sergio Pellegrino, Phil Howard, and Mike Notter. Tape spring large deployable antenna. In *47th AIAA/ASME/ASCE/AHS/ASC Structures, Structural Dynamics, and Materials Conference 14th AIAA/ASME/AHS Adaptive Structures Conference 7th*, page 1601, 2006.

[34] S Tieszen, A Ooi, P Durbin, and M Behnia. Modeling of natural convection heat transfer. In *Proceedings of the Summer Program*, pages 287–302, 1998.

[35] Harald van Weeren, H J. M. ter Brake, Gerrit Holl, Rob J. Hamann, and Steve Price. Thermal aspects of satellite downscaling. *Journal of Thermophysics and Heat Transfer - J THERMOPHYS HEAT TRANSFER*, 23:592–600, 07 2009. doi: 10.2514/1.41857.

[36] Thyrso Villela, Cesar A. Costa, Alessandra M. Brandão, Fernando T. Bueno, and Rodrigo Leonardi. Towards the thousandth cubesat: A statistical overview. *International Journal of Aerospace Engineering*, 2019, 2019.

[37] Mark Wellons. The stefan-boltzmann law. *Physics Department, The College of Wooster, Wooster, Ohio*, 44691, 2007.